Doctoral Dissertations   Graduate School

12-2020

Investigating transmembrane-lipid interactions of EphA2 and pH responsive peptides

Katherine M. Stefanski
University of Tennessee, Knoxville, kstefans@utk.edu

To the Graduate Council:

I am submitting herewith a dissertation written by Katherine M. Stefanski entitled "Investigating transmembrane-lipid interactions of EphA2 and pH responsive peptides." I have examined the final electronic copy of this dissertation for form and content and recommend that it be accepted in partial fulfillment of the requirements for the degree of Doctor of Philosophy, with a major in Life Sciences.

Francisco N. Barrera, Major Professor

We have read this dissertation and recommend its acceptance:

Dan Roberts, Jennifer Morrell-Falvey, Rachel McCord, Bruce McKee

Accepted for the Council:

Dixie L. Thompson

Vice Provost and Dean of the Graduate School

(Original signatures are on file with official student records.)

Characterizing transmembrane-lipid interactions of EphA2 and pH responsive peptides

A Dissertation Presented for the
Doctor of Philosophy
Degree
The University of Tennessee, Knoxville

Katherine Mackenzie Stefanski
December 2020

DEDICATION

For Dr. Elizabeth Howell and the nearly 10 million lives lost globally to cancer each year.

ACKNOWLEDGEMENTS

ABSTRACT

Single-pass membrane receptor signaling plays vital roles in human development and maintaining homeostasis. These membrane receptors can also have causative functions in several diseases including cancer. Much is known about the structure and signaling outcomes of these receptors but the mechanistic details of how they pass an extracellular signal across the membrane and into cytoplasm via the transmembrane (TM) domain is unclear. It is further unknown how or if interactions with membrane lipids facilitate and/or regulate these events. Here we use the TYPE7 peptide to target the TM region of a receptor tyrosine kinase, EphA2. EphA2 engages in both tumorigenic (ligand-independent) and anti-tumorigenic (ligand-dependent) signaling making it an attractive drug target. From TYPE7 we learned that the activity of EphA2 could be modulated by interactions with a TM peptide. Findings from TYPE7 (Chapter II), lead to hypotheses about the signaling states of EphA2 and interactions with anionic lipids. We next demonstrated (Chapter III) that there is a TM conformation-specific coupling of juxtamembrane residues of EphA2 with PIP_2 [phosphatidylinositol 4,5-bisphosphate]. Our data suggests that PIP_2 promotes dimerization of EphA2 in the ligand-independent state, potentially regulating tumorigenic signaling. These findings add to the knowledge of the molecular events of EphA2 signal transduction which is vital to designing effective therapeutics. Finally, we investigated the effects that TM peptides can have on their lipid environments. We developed (Chapter IV) a fluorescence recovery after photobleaching (FRAP) protocol and an automated data analysis pipeline using programs written in Python and Mathematica languages for the determination of lipid diffusion coefficients. We used the pH responsive peptide (pHLIP) as a model TM domain and FRAP in supported lipid bilayers to investigate the effect of pHLIP on the rate of lipid diffusion.

TABLE OF CONTENTS

LIST OF FIGURES

Chapter I. Introduction

1.1 Membrane Proteins

Eukaryotic cells have lipid membranes to encapsulate their contents from the extracellular environment and to generate intracellular organelles. Membranes establish necessary boundaries so that the chemical processes that support life can occur. While the encapsulation established by membranes is crucial, the flow of information and certain molecules across this membrane is just as crucial. To accomplish this, a host of membrane protein families have evolved. Peripheral membrane proteins associate with one leaflet of the bilayer while integral membrane proteins span both leaflets of the bilayer. Integral membrane proteins account for roughly one third of the human proteome and can be categorized by both structure and function (1). Membrane proteins can be grouped into several broad, functional categories including transport proteins, enzymes, cell adhesion proteins, and signaling receptors.

These proteins have different characteristics based on which membrane they are localized to. While 22% of all human proteins exist at the cell surface they represent 60% of all drug targets (2). Cell membrane receptors convey signals from the outside of a cell to the inside of a cell. Structurally, they are comprised of extracellular, transmembrane, and intracellular regions. The extracellular domain(s) bind to a signaling molecule(s) (ligand) then confer that signal across the membrane through the transmembrane region(s) to the intracellular domain(s) resulting in downstream changes in intracellular signaling. Signaling

molecules include hormones, neurotransmitters, growth factors, cytokines, nutrients, and cell adhesion molecules (3).

The most abundant membrane receptors are G-protein coupled receptors (GPCRs) (4) and single pass membrane receptors including the highly studied receptor tyrosine kinases (RTKs) (the second largest family of membrane receptors) (5). GPCRs have seven transmembrane domains (TMDs) and when bound by an extracellular ligand pass the signal to a peripheral G-protein on the membrane inner leaflet (6). The G-protein then affects downstream signaling changes. A similar effect is achieved by RTKs which have a single TMD. Unlike GPCRs, binding of an extracellular ligand results in the signal being transduced to an intracellular kinase domain instead of a G-protein (7). Despite their structural differences, both GPCRs and RTKs rely on their TMDs to confer messages from outside of the cell to the inside of the cell.

1.2 Importance of transmembrane domains in signaling

Membrane spanning proteins can have α-helical or beta sheet secondary structures. Due to their similar evolutionary origins to prokaryotes, beta barrel proteins in eukaryotes are found almost exclusively in the mitochondria and chloroplasts. Almost all plasma membrane proteins contain α-helical TMDs. In order to confer information from the extracellular side of the membrane to the intracellular side of the membrane TMDs must conduct some kind of dynamic movement. Multi-pass receptors, like GPCRs, can undergo very large rearrangements of subunits to achieve signal transductions. Single-pass

receptors on the other hand are limited to a handful of motions of their single TMD while avoiding the high energetic cost of hydrophobic mismatch between their non-polar amino acid side chains and the aqueous environment outside of the bilayer. As described by Matthews *et al.* in their 2006 review, TMDs participate in four motions: translation (lateral movements within the plane of the bilayer), piston (vertical movements within the plane of the bilayer), pivot (spinning around the peptide backbone axis) , and rotation (tilting within the plane of the bilayer) (Figure 1) (8). Combining certain individual movements, TMDs can engage in dynamic lateral interactions by forming dimers and higher order oligomers. These interactions are medicated by very specific dimerization interfaces (9, 10).

Two common TMD dimerization interface motifs are GAS$_{right}$ (glycine, serine, alanine, right-handed) and left-handed dimers (11, 12). One of the first dimerization sequences to be described is the glycine zipper (GXXXG) which is an example of a GAS$_{right.}$ Glycine zippers are common and highly over represented in RTK TMD sequences (13). Glycine zipper mediated dimers are stabilized by van der Waals forces and non-canonical Cα-H hydrogen bonding. They also exhibit relatively large interhelical crossing angles of around 40° (14–16).

Left-handed dimers on the other hand exhibit smaller crossing angles of 15-20° (11). These dimers are mediated by heptad repeat motifs which are repeating units of seven amino acids in which the sequence contains the

4
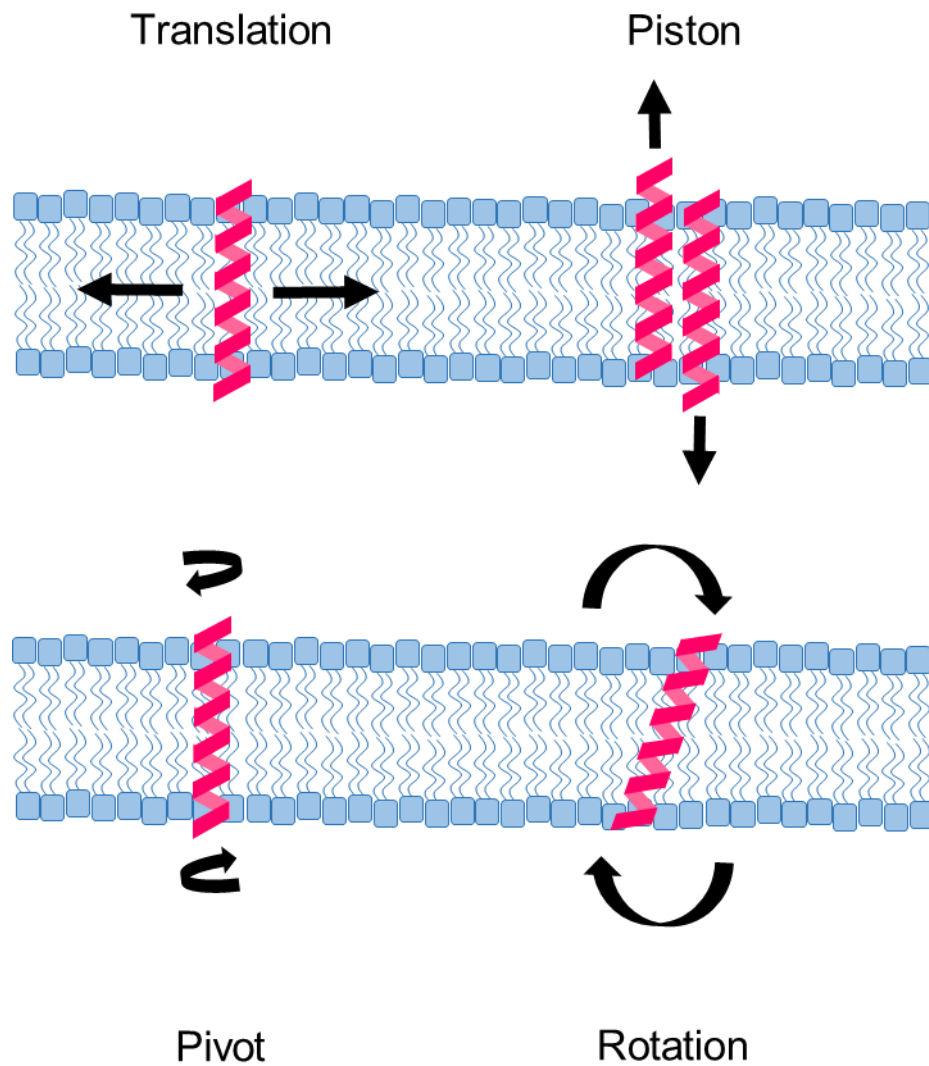
Figure 1. Four principle TMD motions.

TMDs can move via translation (laterally in the plane of the bilayer, piston (vertically), pivot (rotation around the peptide backbone) and/or rotation (tilting) motions due to hydrophobic constraints.

following pattern: H-P-P-H-C-P-C. Where, typically, H is a hydrophobic residue, P is a polar residue and C is a charged residue (17). The interface tends to be mediated by interactions between hydrophobic or charged residues (18).

The classic model of RTK activation involves a monomeric receptor undergoing dimerization in a ligand dependent manner (19). However, in recent years this model has been determined to be overly simplistic as it has been found that many RTKs form unliganded dimers (20). Several studies have suggested that receptors transition from one dimerization motif to another in a manner that involves changes via pivoting and rotational movements of two TMDs relative to each other. It has been proposed that this kind of change occurs in fibroblast growth factor receptor (FGFR), Eph receptors, ErbB2/HER2, and epidermal growth factor receptor (EGFR) (21–24). This can involve switching from one right-handed interface to another in a different position on the helix as seen in ErbB which switches from a C-terminal GXXXG motif to an N-terminal GXXXG motif (24). Or, as is proposed, for EphA2 a switch from a right-handed dimer to a left-handed dimer can occur (22). It has been shown that these signaling related changes in dimerization also cause changes in localization at the plasma membrane.

As will be discussed in detail below (section 1.6), the lipid environment in which a TMD resides can have important functional consequences. Cell membranes are organized laterally into distinct domains including lipid rafts. Recent studies have shown that recruitment of membrane proteins into lipid rafts

6

is dependent on TMD structure and composition. It has been found that TMD length, surface area and palmitoylation are strong predictors of raft affinity with longer, palmitoylated TMDs with smaller surface areas preferring the raft environment (25). This can have functionally important consequences for signaling. For example, the urokinase-type plasminogen activator receptor (uPAR/CD87) dimerizes and preferentially partitions with lipid rafts and this partitioning accelerates downstream signaling outcomes (26).

1.3 pH Responsive Transmembrane Peptides

Due to their membrane-spanning ability and importance in conferring signals, transmembrane domains have been highly studied for their potential as therapeutic agents and targets. There exists a large group of membrane active peptides which includes anti-microbial peptides, cell-penetrating peptides, and pH responsive peptides. Perhaps the best known and well-characterized of this last group is the pH low insertion peptide (pHLIP). The sequence of pHLIP is from the C-helix of the bacteriorhodopsin protein from *Halobacterium halobium* (27, 28). The unique sequence characteristics of pHLIP allow it to be soluble in solution at neutral pH (state I), bind with lipids in solution at neutral pH (state II) and form a transmembrane α-helix at acidic pH (state III) (Figure 2) (27, 28). This behavior is due to the seven acidic amino acids in the sequence of pHLIP (Table 1). In their unprotonated state at neutral pH the peptide remains soluble and unfolded. The peptide remains unstructured when it associates with lipid membranes in

Table 1. Transmembrane peptides studied for their interactions with membranes

Name	Sequence	Molecular Weight (Daltons)
pHLIP	G G E Q N P I Y W A R Y A D W L F T T P L L L L D L A L L V D A D E G T	4079.62
EphA2 TMJM	G S G N L A V I G G V A V G V V L L L V L A G V G F F I H R R R K C W N	3749.53
TYPE7	E F Q T L S P E G S G N L A V I G G V A V G V V L E L V L A G V E F F I E E E E E	4277.79

State I
Neutral pH

State II
Neutral pH
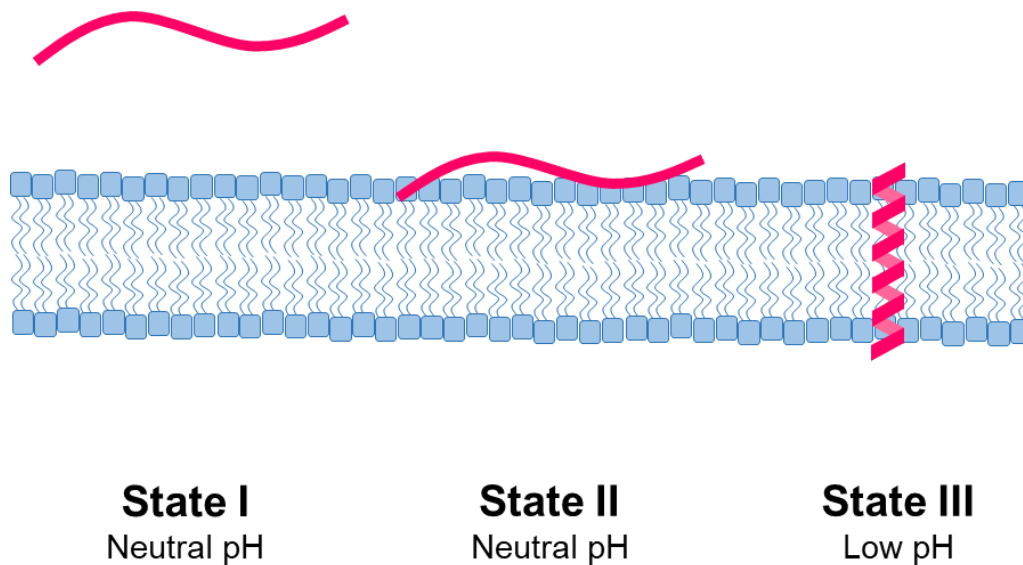
State III
Low pH

Figure 2. Three states of a pH responsive peptide.

pH responsive peptides are disordered and soluble in solution (State I) and will bind with membranes (State II) at neutral pH. In a low pH environment, pH responsive peptides form transmembrane α-helices (State III).

state II. Upon a decrease in pH the acidic amino acids become protonated driving α-helical formation and increased hydrophobicity resulting in state III (29, 30).

The characteristics of pHLIP are particularly appealing as an agent to target solid tumors in cancer (31). The pH of the tumor environment in cancer is lower than the rest of the body due to the Warburg effect (a shift toward anaerobic glycolysis), which causes lactic acidosis, and poor blood perfusion in solid tumors (32). The logic behind using pHLIP as a therapeutic agent is that it will bypass cells at a healthy pH and selectively insert into only those in an acidic environment. Studies have shown that pHLIP is, in fact, not toxic to healthy tissues while inserting into cells at low pH (33). When injected into mouse cancer models, pHLIP successfully accumulates in tumors regardless of tumor size (31). The potential applications for pHLIP are numerous and are continually being explored.

Early studies demonstrated that pHLIP could carry cytotoxic agents or other membrane impermeable drugs across the plasma membrane and into cells (34–36). pHLIP has also been used to deliver gold nanoparticles to tumors in mouse models (37). More recently, pHLIP has been used to deliver gene silencing siRNA into cancer cells and antisense RNAs which inhibit long non-coding RNAs sensitizing tumors to other treatments (38, 39).

In addition to direct therapeutic applications, pHLIP has also been employed for targeted imaging of tumors (40). When conjugated to a radionuclide, pHLIP

has been used in positron emission tomography (PET) and single-photon emission computed tomography (SPECT) to produce high contrast diagnostic images (41–43). Fluorescently labeled pHLIP has been used to effectively target and label several different types and sizes of tumors and malignant lesions (44–46). These fluorescently labeled versions of pHLIP may be useful for precisely labeling tumor margins enabling complete surgical excision.

Unsurprisingly, the advances made with pHLIP have spawned new pH-responsive peptides bearing high to low sequence similarity to pHLIP as researchers seek to fine-tune the application of these peptides. Several pHLIP variants have been generated by changing the one or both of the titratable aspartic acids from the WT sequence resulting in variants with altered pK_a values (47). By contrast, our lab developed the acidity-triggered rational membrane (ATRAM) peptide which has less than 25% sequence identity to pHLIP but engages in the same three-state insertion process as pHLIP. ATRAM however, inserts into cells at a higher pH than pHLIP (6.5 vs. 5) which targets the mildly acidic environment of cancer cells more efficiently (48).

Taking the departure from pHLIP even further, our lab has been testing the ability to design pH-responsive peptides based on transmembrane domains of a variety of membrane proteins. Current projects include peptides which target T-cell receptor (TCR) and neurotrophic tyrosine kinase, receptor-related 1 (ROR1). We recently published the TYPE7 peptide which binds to the receptor tyrosine

10

kinase EphA2 in cancer cells and modulates its signaling (49). Studies involving TYPE7 are discussed in detail in Chapter 2.

1.4 Receptor Tyrosine Kinases

The largest family of enzyme-linked cell surface receptors are the receptor tyrosine kinases (RTKs). RTKs are single-pass membrane proteins whose activation by binding to an extracellular ligand induces phosphorylation events by an intracellular kinase domain. Humans express 58 known RTKs which fall into 20 families. They are key regulators critical processes such as cell cycle, metabolism, proliferation, differentiation, and migration (50, 51). All RTKs have the same basic domain architecture: an extracellular, N-terminal ligand binding domain, a single pass TMD, an intracellular juxtamembrane regulatory region, a protein kinase domain, and a C-terminal regulatory region (7). RTKs engage in lateral interactions in cell membranes forming dimers or larger order oligomers. Dimerization or oligomerization may or may not precede binding of an extracellular ligand. Nevertheless, ligand binding is believed to drive changes in oligomerization via the extracellular domains which is conferred to the intracellular domains to activate kinase activity resulting in cross-phosphorylation of the RTKs. The phosphorylated protein then becomes a scaffold for assembly and activation of downstream signaling effectors (50).

Ligands induce dimerization of the extracellular domains frequently in the form of a divalent ligand that binds to two ligand binding domains of an RTK forming a heterotetramer. This kind of organization has been identified in crystal

structures of several RTKs including vascular endothelial growth factor (VEGF) receptor, Eph receptors, the nerve grown factor TrkA, and Tie2 (52–57). This kind of complex can involve only receptor-ligand interactions, as in TrkA, or it can involve dimerization interfaces between other regions of the extracellular domains, as in KIT, FGRF and Eph receptors (56, 58–60).

Upon activation by ligand binding, crystal structures of the kinase domains of all RTKs adopt a similar form (7). RTK kinase domains have an N-lobe and C-lobe. The activation loop and the αC helix in the kinase N-lobe adopt a specific configuration in all activated RTK kinase domains which is required for phosphorylation to occur (61). On the other hand, structures of inactive kinase domains vary, indicating diverse mechanisms of regulation (7).

Kinase domains can be autoinhibited by the activation loop, juxtamembrane (JM) region, or C-terminal regions. Activation loops can inhibit kinase domains in different ways. For example, in the insulin receptor there is a tyrosine residue in the activation loop that projects into the active site thereby occluding the active site. This configuration is stable and blocks access to ATP and protein substrates (62). Upon ligand activation, a different tyrosine residue becomes trans-phosphorylated causing the activation loop to become "active" and released from the autoinhibited state (61). Juxtamembrane autoinhibition involves the unstructured JM making extensive stable contacts with the kinase domain including the activation loop. These contacts involve tyrosine residues of the JM which upon ligand stimulation, become phosphorylated releasing the

autoinhibited state (62). While the exact details of these interactions vary, this kind of autoinhibition has been observed in KIT, Flt3, and Eph receptors (63–65). Finally, an interesting mechanism of C-terminal mediated autoinhibition of the kinase domain is exhibited by Tie2. A region in the C-terminal tail containing phophorylatable tyrosines contacts the kinase domain and blocks substrate access to the active site (66). These methods of self-regulation are believed to prevent premature activation of the RTKs.

Upon ligand activation, RTKs undergo a series of trans and autophosphorylation events. The result is the formation of downstream signaling complexes. The first result is the recruitment of proteins containing SH2 or PTB domains that bind to phosphotyrosines in the RTK (67, 68). These proteins become phosphorylated and recruit other proteins to the RTK which become phosphorylated as well. Some interact directly with the phosphotyrosines of the RTK or indirectly through other docking proteins (69). With multiple phosphotyrosines on each receptor and docking partners, RTKs are primed to influence a wide variety of signaling pathways.

These signaling pathways were once thought to be linear but have since been revealed to be branching, interconnected networks. The result is complex and dynamic signaling with RTKs acting as nodes in the networks. Positive and negative feedback loops are integrated across multiple members of a network to effect different cellular outcomes. These networks are vast and complex. For example, the signaling network of EGFR contains 211 reactions with 322

components (70). Also, simply knowing the components involved does not allow for predicting cellular outcomes.

Recently, Zinkle and Mohammadi proposed a threshold model for RTK signaling and cellular response (71). They suggest that quantitative differences in the strength/longevity of ligand-activated dimers results in quantitative and qualitative difference in activation loop tyrosine phosphorylation (how many vs. the pattern of residues which get phosphorylated). The quantitative differences, they claim, lead to differences in duration of signaling while the qualitative differences lead to recruitment of distinct substrates and therefore activation of distinct pathways. For example, studies with FGFR have revealed that some phosphorylation sites are sensitive to dimer stability meaning that some sites require different degrees of dimer stability in order to become phosphorylated (72, 73). It has also been shown that specific adaptor proteins only bind to and become activated by specific phosphorylated tyrosines in FRGR activation loop (72). In this way FGFR can affect different cell outcomes (like cell migration vs cell proliferation) which result from binding of different ligands which promote dimers that have different stabilities. Data like this exists for many other receptors supporting the threshold model for RTK pathway activation (71).

RTK signaling is typically downregulated by endocytosis and degradation of the receptor. When internalized, RTKs continue to promote signaling until the receptor is dephosphorylated, ubiquitylated, and finally the ligand is removed in the acidic environment of the lysosome (7, 74, 75). The step of endocytosis at

14

which each of these occur depends in the RTK and ligand pair. Some RTKs are degraded while some are recycled back to the cell surface. Ubiquitylation of RTKs has been shown to be important in designating receptor fate. Several studies show that mono-ubiquitylation directs RTKs to clathrin coated pits for endocytosis and degradation (76). On the other hand, studies with EGFR have shown that ubiquitylation is not necessary for endocytosis but only for degradation (77, 78). The exact roles of mono- and polyubiquitylation in RTKs is an ongoing area of research.

Beyond their signaling functions in healthy tissues, RTKs are of immense interest due to their dysregulation and deregulation resulting in human diseases, particularly cancers. RTKs promote cancer through 4 key mechanisms: autocrine activation, chromosomal translocations, overexpression, and/or gain-of-function mutations. The EGFR family of receptors is known to be overexpressed, often due to gene duplication, in several cancers (79). The KIT family of RTKs demonstrate activating gain-of-function mutation in gastrointestinal stromal tumors, acute myeloid leukemia, mast cell leukemia, and melanoma (80–83). Chromosomal translocations are responsible for expression of FGFR dimeric fusion proteins which are constitutively active in several cancers (84).

1.5 Introduction to Eph receptors and EphA2

Of the RTKs, the largest family are the Eph receptors with 14 genes in the human genome. Eph receptors are of interest as models for RTK structure and function, their unique signaling modalities, and their roles in human diseases.

Eph receptors pair with ephrin ligands and are classified as EphA or EphB based on the structure of their ephrin ligand. Type A ephrins are bound to the cell membrane via a glycosylphosphatidylinositol (GPI) linkage while type B ephrins are single-pass membrane proteins. In addition to the forward signaling induced by kinase activation on the Eph receptor bearing cell, ligand binding results in reverse signaling on the ephrin bearing cell. Type-A ephrins which lack intracellular domains rely on co-receptors while type-B ephrins have SRC homology 2 and PDZ binding motifs to interact with downstream signaling components. In either case, ephrin reverse signaling affects cell retraction, migration, adhesion, and proliferation. Ephrin reverse signaling has not been as thoroughly studied as Eph forward signaling. Typically, Eph signaling performs roles in tissue patterning during embryonic environment, wound healing, and synaptic plasticity.

During embryogenesis, Eph receptors contribute to the formation of tissues by regulating cell sorting. For example, Eph receptors help establish hindbrain segmental patterning by preventing intermixing of cells from adjacent segments (85, 86). Several Eph receptors play roles during angiogenesis. For example, EphB4 is expressed in venous endothelial cells while ephrinB2, its ligand, is expressed in arterial endothelial cells. Their interactions are believed to define boundaries between endothelial venous and arterial cells (87, 88).

Typically, in healthy adult tissues, Eph expression becomes limited with some exceptions. In the brain, EphA4 participates in synaptic plasticity. Among other

effects, EphA4 signaling in neurons leads to phosphorylation of the non-receptor tyrosine kinase c-Abl1(89, 90). c-Abl is responsible for cytoskeletal remodeling via actin depolymerization which causes growth cone collapse and the retraction of dendritic spines known as dendrite pruning(91). Further, EphA4 activation results in the removal of the synaptic glutamate AMPA receptor (AMPAR), decreasing synaptic strength (92, 93). Removal of AMPAR and dendrite pruning are part of healthy neuroplasticity and work to maintain appropriate excitatory signaling strength.

Several Eph receptors and ephrins are involved in inflammation and wound healing. For example, after lung injury is induced, EphA2 and ephrinA1 are both upregulated (94, 95). It is believed that in the vascular endothelium EphA1/ephrinA1 regulates secretion of pro-inflammatory signals such as monocyte chemoattractant protein and C-X-C motif chemokine ligand 1. As mentioned above, EphB4/ephrinB2 are important for angiogenesis during embryonic development. EphrinB2 expression is also induced during hypoxia, driving angiogenesis through induction of vascular endothelial growth factor signaling (96, 97).

Beyond these roles in healthy tissues, Eph receptors are involved in many human diseases. As mentioned above EphA4 signaling regulates synaptic homeostasis. However, in the context of Alzheimer's disease (AD), EphA4 is bound by amyloid β and aberrantly activates signaling leading to loss of dendritic spines and synaptic signaling and also phosphorylation of the non-receptor

tyrosine kinase c-Abl1(7, 8, 16). In fact, blocking EphA4 signaling in tissue culture and in AD mouse models has been shown to ameliorate synaptic defects (90, 98). Interestingly, phosphorylation of c-Abl has also been linked to phosphorylation of Cdk5 which in turn phosphorylates tau contributing to neurofibrillary tangles, a hallmark of AD (99, 100). EphA4 is also overexpressed in amyotrophic lateral sclerosis (ALS) where it causes motor neuron degeneration(101, 102). Eph receptors have also been implicated in skeletal malformations. For example, loss of EphB2/B3 signaling is implicated in craniofacial bone malformations that cause cleft palate (103).

Additionally, a large body of research exists establishing that many Eph receptors are overexpressed in a variety of cancer types. Specifically, EphA2 overexpression at both the mRNA and protein level is found in breast, ovarian, prostate, and pancreatic cancers (104–107). Furthermore, EphA2 overexpression is correlated with cancer severity. For example, one study of esophageal cancers found that 50% of patient tumors had EphA2 overexpression that correlated with rates of lymph node metastasis and low rates of survival (108). EphA2 overexpression has also been linked to poor survival rates in glioblastoma, cervical, ovarian, and renal cancers (109–112).

Aside from overexpression causing disease, EphA2 is also a known receptor for several viruses. EphA2 is a crucial receptor for Kaposi's sarcoma-associated herpesvirus (KSVH). KSHV is the cause of Kaposi's sarcoma and at least two B cell malignancies (113). In several cell lines, expression levels of

EphA2 correlates with increased viral entry and deletion of the gene in mice abolishes infection (114). Similarly, EphA2 is also an epithelial receptor for Epstein-Barr virus (EBV) (115, 116). EBV causes gastric carcinomas and B cell lymphomas (117). It was found that EBV binds to the ligand binding and fibronectin type III repeat domains of EphA2 and RNA knockdown of EphA2 in cells prevents EBV infection (115). Binding of EBV may be highly specific to EphA2 as it was found that EBV does not bind to the closely related EphA4 (116). EphA2, together with EGFR, has also been identified as a host cofactor for Hepatitis C viral entry (118).

To better understand its role is disease, we must examine the function of EphA2. EphA2 signaling pathways control cell proliferation, migration, and cell retraction (119). It has been demonstrated in several studies that overexpression of EphA2 in cancers is accompanied by a loss of ephrin ligand (120, 121). It is believed that this imbalance of EphA2 overexpression and loss of ligand-dependent signaling causes tumor formation.

Eph2 and all Eph receptors share the same common RTK domain architecture (Fig. 1) with a ligand binding domain (LBD), cysteine rich domain (CRD), two fibronectin-like repeats (FN), a transmembrane domain (TMD), a disordered juxtamembrane (JM) region, kinase domain (KD), sterile α motif domain (SAM) and a PDZ-binding motif.

Ephrin binding induces formation of heterotetramers via ephrin-LBD and LBD-LBD interactions. Eph-Eph dimerization is also facilitated by CRD-CRD

interactions (56). This results in the formation of large, micron sized, signaling clusters at the plasma membrane (122, 123).

EphA2 is has two modes of signaling: ligand-independent and ligand-dependent. Ligand-independent (Figure 3, left) is responsible for tumorigenic phenotypes via phosphorylation of S897 by AKT, RSK, and PKA (124–127). EphA2 phospho-S897 is known to localize to the leading edges of migratory cells where it is believed to promote assembly of the actin cytoskeleton in lamellipodia extensions (124, 126). EphA2 phospho-S897 promotes RhoG/Rac activation which promotes cell motility. EphA2 induced RhoG activation was also found to inhibit apoptosis through PI3K interactions (128), and EphA2 serine phosphorylation was found to prevent cell retraction (127).

Conversely, ligand-dependent signaling requires activation of EphA2 by its ligand ephrinA1 (Figure 3, right). Ligand binding causes changes in dimerization and the formation of large oligomers. The kinase domain is then activated resulting in the phosphorylation of Y588, Y594 and Y772. Ligand-dependent signaling has been shown to inhibit metastatic phenotypes by causing decreases in proliferation, migration, and cell retraction/rounding (124, 129, 130). For example, tyrosine phosphorylation inhibits mitogen-activated protein (MAP) kinase phosphorylation which reduces cell proliferation(131, 132). Ephrin induced phosphorylation recruits SHP-2 which dephosphorylates focal adhesion kinase (FAK) which disrupts integrin function and results in decreased cell adhesion (129). FAK is also believed to be responsible for the cytoskeletal rearrangements

20
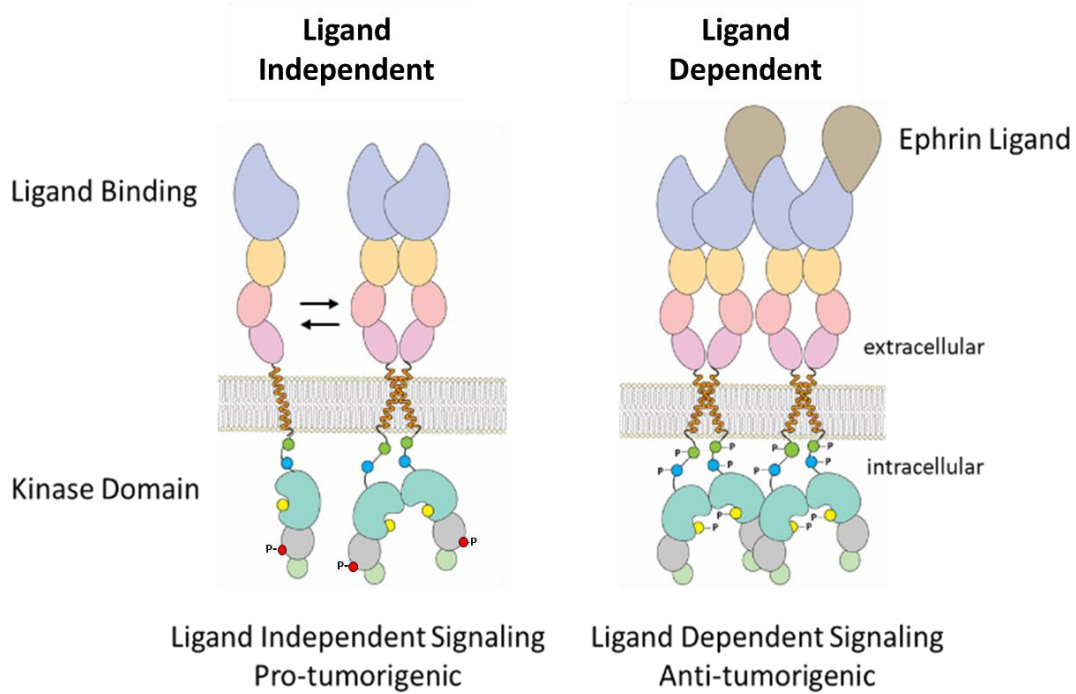
Figure 3. Architecture and oligomerization of EphA2 in two signaling states.

(Left) In the ligand-independent state EphA2 exists in a monomer-dimer equilibrium. Pro-tumorigenic signaling is promoted via phosphorylation of S897. **(Right)** Upon binding of ephrinA1 on an adjacent cell, EphA2 forms large signaling clusters and the kinase domain is activated resulting in trans-autophosphorylation of three tyrosine residues resulting in downstream anti-tumorigenic signaling.

that cause ephrinA1-induced cell rounding/contraction (133). Finally, ligand-dependent signaling results in endocytosis of Eph signaling clusters. From the endosome, the receptors are either degraded or recycled back to the plasma membrane (134–136).

While many aspects of Eph receptor signaling have been worked out, the exact molecular details of how the receptor passes an extracelular signal across the plasma membrane are unknown. As a membrane spanning receptor, the transmembrane domain (TMD), must play a role in conferring signals.

To investigate interactions between TMDs of EphA2, an NMR structure of the TMD dimer was solved (137). To the authors' surprise, it was found that this dimer interface is mediated by a heptad repeat motif even though the EphA2 TMD sequence contains a glycine zipper (GXXXG) dimerization motif which is generally overrepresented in RTK TMD dimer interfaces (13). In the same 2010 study, Bocharov *et al.* also conducted molecular dynamics (MD) on the NMR structure and found upon relaxation that the EphA2 TMD dimer rotated to the glycine zipper interface. It was then hypothesized that the receptor can switch between these two dimerization interfaces.

In a follow-up study it was reported that mutations in the heptad repeat decreased ligand independent signaling while mutations in the glycine zipper decreased ligand-dependent signaling (22). These findings combined with the structural data gave rise to the following model (Figure 4): In the ligand-
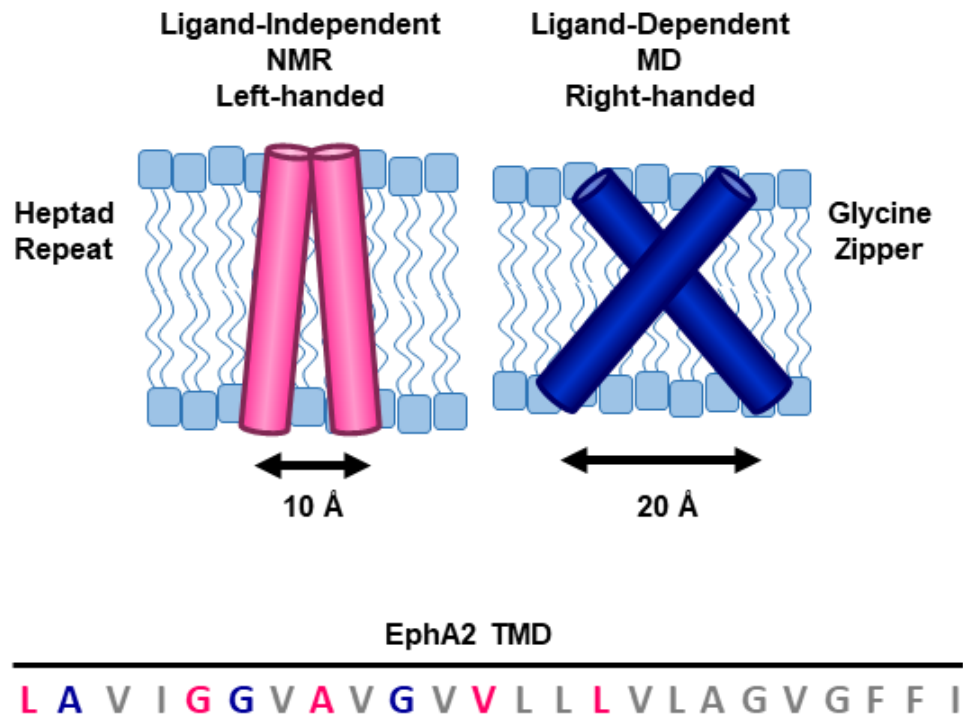
Figure 4. Structures of EphA2 TMD dimers in two signaling states.

(Left) In the ligand-independent state the EphA2 TMD dimerizes via a heptad repeat motif with a small interhelical crossing angle. **(Right)** Upon binding of ephrinA1 the EphA2 TMD dimer rotates to a glycine zipper motif resulting in a larger interhelical crossing angle. (Bottom) Sequence of EphA2 TMD highlighting HR residues (fuchsia) and GZ residues (navy) as identified by Bocharov *et al*., 2009.

independent signaling state the EphA2 TMD dimerizes via the heptad repeat

(Fig. 2, left) with a helical crossing angle of 15° while in the ligand-dependent

(Fig. 2, right) signaling state EphA2 dimerizes via the glycine zipper with a helical

crossing angle of 45° (22, 137). It is unknown how the switch in dimerization

interface and opening of the interhelical crossing angle participates in conferring

the extracellular signal from the outside of the cell to the inside. It is also

unknown if the JM region responds to these changes in TMD orientation. It is

also unknown if or how the lipid environment interacts the TMD and JM of

EphA2. We investigate this in Chapter 3.

1.6 Phospholipids and functional roles in signaling

Plasma membranes of cells are composed of lipids, proteins, and

carbohydrates (138). Of these components, the lipids are grouped into three

major classes: phospholipids, cholesterol, and glycolipids (139). Phospholipids

make up the majority of the plasma membrane lipids. Phospholipid molecules are

composed each of a polar head group with two hydrophobic hydrocarbon tails of

varying degrees of saturation and length (139) and, in aqueous environments,

will spontaneously form bilayers by orienting their headgroups towards the

solvent and their acyl chains toward each other.

Phospholipids fall into two groups: glycerophospholipids (containing a

glycerol and phosphate headgroup) and phosphosphingolipids (containing a

sphingosine backbone and phosphocholine). Common examples of

glycerophospholipids found in membranes include phosphatidylcholine (PC),

24

phosphatidylserine (PS), and phosphatidylethanolamine (PE) while sphingomyelin (SM) is a common a phosphosphingolipid. Together these lipids comprise most of the structure of the cell membrane. The plasma membrane has a unique asymmetry with the outer leaflet being primarily PC and SM while the inner leaflet being primarily PE, PS and phosphatidylinositol.

Of the phospholipids, phosphoinositides represent a small fraction of lipids in the plasma membrane (140). Despite their low abundance they play vital roles in crucial cellular processes. Phosphatidylinositol(4,5)-bisphosphate (PIP_2) and phosphatidylinositol (3,4,5)-trisphosphate (PIP_3) make up less than 1% of membrane phospholipids but regulate important signaling pathways (140, 141). As such, the relative levels of phosphoinositides are under careful regulatory control. PIP_2 is synthesized in two steps. First, phosphatidylinositol is converted to Phosphatidylinositide(4)-phosphate (PI(4)P) by phosphatidylinositol 4-kinase and then PI(4)P is converted to PIP_2 by PI(4)P kinase 5α (142). PIP_2 can then be phosphorylated to generate PIP_3 by phosphatidylinositol 3-kinase or dephosphorylated by phospholipase C (PLC) to inositol triphosphate (IP3) and diacylglycerol (DAG). IP3, DAG, and PIP_3 are all important secondary messengers.

When cleaved by PLC from PIP_2, IP3 is released as a soluble molecule which is then free to diffuse through the cell to the endoplasmic reticulum where it binds to a ligand-gated calcium channel causing the release of intracellular Ca^{2+} stores (143, 144). Meanwhile, DAG remains at the membrane where it

binds to and activates protein kinase C (PKC) (144). PKC phosphorylates

proteins in a wide variety of signal transduction cascades depending on the

specific cell type (145, 146).

Phosphoinositides are bound by proteins containing pleckstrin homology

(PH), ezrin/radixin/moesin family (FERM), and epsin N-terminal homology

(ENTH) domains (147–149). Proteins with ENTH domains (epsin and CALM) are

believed to bind to PIP_2 and regulate the assembly of clathrin coats at sites of

endocytosis (148, 150). Dephosphorylation of PIP_2 by synaptojanin to PI(4)P

induces the disassembly of the clathrin lattice (151). ERM family proteins have

an N-terminal FERM domain that binds to the C-terminus of the protein. Upon

FERM binding to PIP_2 the C-terminus is released, and the protein is able to

interact with other proteins involved in linking actin to the plasma membrane

(152). PH domains have been identified in over 100 proteins which play roles in

reorganization of the actin cytoskeleton. Most PH domains will bind any

phosphoinositide with high affinity and low selectivity (153). There are a handful

of exceptions to this observation which bind selectively to PIP_2 or PIP_3

exclusively underscoring the importance of these lipids.

In addition to these structured domains, there are several examples of

proteins with unstructured regions which bind to PIPs. A common feature to

these proteins is regions containing clusters of basic residues. For example,

MARCKS (Myristoylated Alanine-Rich C-Kinase Substrate) is an unstructured

protein with a myristate membrane anchor. The myristate alone however is not

sufficient for tethering the protein to the membrane. MARCKS contains a region of 13 basic residues which bind electrostatically to the negatively charged PIP_2 headgroup with high affinity helping to attach MARCKS to the membrane (154). Binding of this region by Ca^{2+}/calmodulin results in the release MARCKS from the membrane into the cytosol (155). This mode of electrostatic binding to PIP_2 has been demonstrated for other proteins/domains.

It has been proposed that electrostatic interactions with PIP_2 of the JM and kinase domains of EGFR are responsible for autoinhibition of the receptor (156, 157). It has been shown that the JM and kinase domains, which have positively charged residues interact with PIP_2 containing membranes. During ligand-induced activation of EGFR the receptor undergoes TMD dimer rearrangements and trans-autophosphorylation occurs via the kinase domains. These phosphorylation events result in the activation of downstream signaling cascades. It is believed that electrostatic interactions with PIP_2 of the JM and kinase domains prior to ligand binding prevent inappropriate signaling events. The transition of the JM and kinase domains from the membrane bound to unbound state is facilitated by binding of Ca^{2+}/calmodulin to basic JM residues (156, 158). This binding is believed to outcompete the PIP_2 interactions and release both the JM and kinase domains thereby facilitating signaling (156, 157). A key aspect of this model is the coupling between changes in TMD dimerization and changes in JM-PIP_2 interactions.

A similar mechanism has been proposed for FGFR. In one study it was observed that FGFR TMD tilt angle is coupled to JM-PIP_2 interactions (21). The authors proposed that the FGFR unliganded dimer exhibits more tilted TMDs and that in this state the JM is tethered to the membrane via PIP_2 interactions while the liganded dimer exhibits less tilted TMDs and in this state the JM is released from the membrane (21). The importance of these electrostatic interactions between juxtamembrane domains and PIP_2 are currently being explored for other receptors. For example, molecular dynamics simulations have been used to predict strong interactions of PIP_2 with all 58 RTKs and tropomyosin receptor kinase A (TrkA) (159, 160). Specifically, strong interactions with the JM and kinase domains of EphA2 have been predicted but have not been demonstrated experimentally. The functional implications of these interactions have also not been established. EphA2 JM-PIP_2 interactions are explored in detail Chapter III.

Chapter II.
Interactions between TYPE7 and EphA2 in cells and effects on cell morphology

A portion of this chapter (Figure 5) was published by Daiane S. Alves, Justin M. Westerfield, Xiaojun Shi, Vanessa P. Nguyen, Katherine M. Stefanski, Kristen R. Booth, Soyeon Kim, Jennifer Morrell-Falvey, Bing-Cheng Wang, Steven M. Abel, Adam W. Smith, and Francisco N Barrera:

Alves, D. S., Westerfield, J. M., Shi, X., Nguyen, V. P., Stefanski, K. M., Booth, K. R., Kim, S., Morrell-Falvey, J., Wang, B. C., Abel, S. M., Smith, A. W., and Barrera, F. N. (2018) A novel pH-dependent membrane peptide that binds to EphA2 and inhibits cell migration. *Elife.* **7**, 1–22

Daiane S. Alves conceptualized the project, collected and analyzed data, wrote and edited the manuscript. Justin M. Westerfield collected and analyzed data, wrote and edited the manuscript. Xiaojun Shi, Vanessa P. Nguyen, Soyeon Kim, Bing-Cheng Wang, and Katherine M. Stefanski collected and analyzed data and edited the manuscript. Kristen R. Booth collected and analyzed data. Jennifer Morrell-Falvey collected and analyzed data and provided resources. Steven M. Abel helped conceptualize the project and assisted with software, analysis, investigation and methods. Adam W. Smith supervised investigators. Francisco N. Barrera conceptualized the project, acquired funding, analyzed data, supervised investigators and wrote and edited the manuscript.

2.1 Abstract

EphA2 is capable of pro-tumorigenic and anti-tumorigenic signaling based on its activation state. When bound by its ephrin ligand the anti-tumorigenic signaling is activated while in its unbound form, it promotes tumorigenic signaling. In the context of cancer, overexpression of the receptor and cleavage of the extracellular domain promote the ligand-independent signaling. We recently developed the pH responsive TYPE7 transmembrane peptide which targets the TM domain of EphA2. TYPE7 causes phosphorylation of a single tyrosine residue and decreased migration of cancer cells, partially mimicking ligand activation. Here we show that TYPE7 associates with endogenous EphA2 in cancer cells at the plasma membrane. We further explore cell contraction, another outcome of ligand-dependent signaling, with TYPE7 and the natural EphA2 ligand, ephrinA1 using both fixed and live cells.

2.2 Introduction

Eph receptors are receptor tyrosine kinases (RTKs) that comprise the largest family of RTKs. Together with their ephrin ligands at cell-cell contacts, Eph receptors are involved in tissue patterning during embryonic development, neuronal plasticity, and wound healing (130). EphA2 signaling plays a role in pathways which control cell proliferation, migration, and cell retraction (119). It is also found to be over expressed in many cancers (130). Specifically, EphA2 overexpression is found among many others, in breast, ovarian, prostate, and pancreatic cancers and is correlated with relatively aggressive tumors and poor

31

patient prognosis (104–107). It is believed that EphA2 is involved in two methods of signaling: ligand dependent and ligand independent. Ligand-independent signaling is responsible for metastatic phenotypes via phosphorylation of S897 by AKT, RSK or PKA (125). Conversely, activation of EphA2 via its ligand ephrinA1 and phosphorylation of tyrosine residues has been shown to inhibit metastatic phenotypes (124). Specifically, EphA2 activation leads to decreases in proliferation, migration, and cell retraction/rounding (130). For these reasons, finding novel methods to activate EphA2 has become an attractive avenue of investigation.

One logical means of promoting the anti-tumorigenic signaling would be to treat tumors with EphA2 agonists. Efforts toward this have been made in the form of antibodies and peptide drugs. As of August 2020, there are twelve antibody drugs which target EphA2 in various stages of development (161). One promising candidate is the mouse EA5 monoclonal antibody which binds to the LBD of EphA2 and mimics the binding of an ephrin ligand. EA5 has been shown to decrease tumor size and cell proliferation (162). Ephrin mimetic peptides like the YSA peptide have also shown promise in targeting and activating ligand-dependent signaling of EphA2 (163).

However, in the tumor environment, the extracellular portion of EphA2 can be cleaved by membrane type I-matrix metalloproteinase (MT1-MMP) thus rendering the receptor blind to activation via the LBD (164, 165). The cleaved receptor has been shown to promote tumorigenic signaling (165). It is therefore

imperative to find a means to target and modulate EphA2 activity in a way that does not depend on the ligand binding domain.

We have recently developed TYPE7 (transmembrane tyrosine kinase peptide for Eph) to promote EphA2 activation by targeting the transmembrane domain (49). TYPE7 was designed to block the transmembrane dimerization interface that is involved in ligand-independent signaling. The occlusion of this interface is believed to promote dimerization at the available ligand-dependent interface. TYPE7 was also designed to be a soluble disordered coil at neutral pH and from a transmembrane alpha helix at acidic pH. Lower than physiological pH (6.5-6.9 vs. 7.2-7.4) is a hallmark of the tumor environment. By being responsive to acidity, TYPE7 can, in theory, bypass healthy tissues and insert into the membranes of cancer cells.

Biophysical experiments show that TYPE7 does form a transmembrane alpha helix in the presence of liposomes at acidic pH. It was found that, in cancer cells, TYPE7 inhibited cell migration as effectively as ephrinA1. Phosphorylation studies demonstrated that this change in behavior was due to phosphorylation of Y772 induced by TYPE7. With this data, we wondered if TYPE7 directly interacts with EphA2 in cancer cells and if TYPE7 could affect other aspects of cancer cell morphology and behavior. We further hypothesized that TYPE7 would have the same effects on tyrosine phosphorylation and cell migration by interactions with EphA2 lacking the extracellular domain.

2.3 Methods

Cell Culture

      PC-3 cells (ATCC, CRL-1435) in F-12K media (Gibco), A375 cells (ATCC, CRL-1619), and Hek293 (ATCC, CRL-1573) were cultured in EMEM or DMEM (Gibco) media. Media was enriched with 10% fetal bovine serum (Gibco), 5% penicillin streptomycin (Gibco). Cells were cultured in a humidified incubator with 5% CO_2.

Co-localization Analysis

      A375 cells were plated at a seeding density of 1 x 10^4 cells per well in a glass-bottom 8-well slide (Ibidi, Munich Germany) coated with 50 μg/mL rat tail collagen I (Gibco, Waltham MA). 24 hours later cells were serum starved. 12 hours later the cells were pre-treated with DMEM containing 2 μM unlabeled TYPE7 for 1 hour at 37° C to prevent high background seen in samples that were not pre-treated. Samples were then treated +/- 0.5 μg/mL EphrinA1-Fc (R&D Systems, Minneapolis MN) and +/- 0.2 μM of TYPE7-Alexa568 in PBS++ for 5 minutes at room temperature followed by a 2 minute wash with PBS++ then immediately fixed in 4% PFA. Samples were then blocked for I hour at room temperature in PBS with 5% goat serum (Gibco). Samples were then incubated with 1:100 rabbit anti-human EphA2 mAb (Cell Signaling, Danvers MA) primary antibody in PBS with 1% BSA (Fisher Scientific, Pittsburgh PA) for 1 hour at room temperature. Samples were rinsed 3 time with PBS++ then incubated with 1:200 goat anti rabbit IgG Alexa488 antibody (Invitrogen) in PBS with 1%BSA in

the dark at room temperature for 45 min. Samples were then rinsed 3 times with PBS++, stained with DAPI and covered with VectaShield mounting medium for fluorescence (Vector Laboratories, Burlingame CA).

Cells were imaged on a confocal laser scanning microscope (Zeiss LSM 710) with 63x and 100x objectives and images were captured using Zen2 blue edition software with excitation wavelengths of 504 nm, 488 nm, and 561 nm and emission were collected at 410-481 nm, 496-584 nm, and 604-733 nm for Dapi, Alexa488, and Alexa568 respectively. Co-localization were subsequently quantified, and Pearson's Correlation Coefficients were generated using the ImageJ Co-localization Threshold plugin. Statistical analyses were performed in IBM SPSS Statistics Software (version 24).

Cell Contraction in Fixed Cells

A375 or PC-3 cells were plated in 5 well of a 24-well plate on glass coverslips at a seeding density of $1x10^5$ cells per well. Cells were grown for 24 hours then, 2 wells were treated with 2 μM TYPE7 in serum free media. All other wells were treated with serum free media. The next morning, cells were treated with 0.5 µg/mL of Fc or EphrinA1-Fc and fresh 2 μM TYPE7 for 10 minutes at 37 °C. The treatments were combined to make the following groups: Control (untreated), Fc only, Type7 only, ephrinA1-Fc only, and Type7 + ephrinA1-Fc. After the 10-minute treatment, cells were rinsed with PBS++ and fixed with 4% paraformaldehyde for 30 minutes at room temperature. Cells were then washed 3 times with PBS++ for 5 minutes each. Cells were then permeabilized with

permeabilization buffer (0.3% Triton X-100, 0.1% bovine serum albumin (BSA) in PBS) at room temperature for 15 minutes. Cells were then blocked in blocking buffer (33% goat serum, 40 mM sodium phosphate, pH 7.4, 450 mM NaCl, 0.6% Triton X-100) for 30 minutes at room temperature. Cells were then incubated with 1:100 rabbit anti-human EphA2 mAb primary antibody in blocking buffer for 1 hour at room temperature. Cells were then washed 3 times with permeabilization buffer. Cells were then incubated with 1:200 goat anti rabbit IgG Alexa488 antibody and phalloidin CF594 (Biotium, Fremont, CA) in blocking buffer for 45 minutes at room temperature. Cells were then rinsed once with PBS++ and the nuclei were stained for 3 min with Dapi. Coverslips were then rinsed with PBS++ then ddH$_2$O and transferred to slides and mounted with VectaShield mounting solution. Cells were imaged on a confocal laser scanning microscope (Zeiss LSM 710) with 40x, 63x and 100x objectives and images were captured using Zen2 blue edition software.

EphA2 immunostaining was used as a visual control to check that in cells not treated with ephrinA1-Fc EphA2 is primarily localized to the plasma membrane, Cells treated with ephrinA1-Fc were checked for EphA2 puncta and endocytosis. Phalloidin staining of actin and Dapi stained nuclei were imaged for measuring cytoplasmic area. To measure this, CellProfiler software (Broad Institute) was employed (166). The "Human Cell" pipeline available online was used for cell measurements. In this pipeline "primary objects" were set to nuclei and identified in the blue channel while "secondary objects" were set to

cytoplasm and identified in the red channel. For each, the global thresholding strategy and Otsu thresholding method were selected for two-class thresholding. To identify the cytoplasm, in "IdentifyTertiaryObjects" the larger identified object was set to "Cells" and the smaller identified object was set to "Nuclei". In "MeasureObjectSizeShape", "Cells", "Cytoplasm", and "Nuclei" were selected". From this pipeline several parameters are measured and exported including area, eccentricity, form factor, maximum and mean radius. Due to large day to day variability in cell areas, data were normalized to control (0% contraction) and ephrinA1-Fc (100% contraction) treatments.

Live Cell Contraction

PC-3 cells were plated at a seeding density of 5000 cells per well and grown for 24 hours. Cells were then serum starved overnight. The next day, cells were placed in L-15 media for imaging. Cells were treated with 0.5 µg/mL ephrinA1-Fc and were imaged via phase contrast every minute for 30 minutes. Cell areas were measured by hand in ImageJ.

Truncated EphA2 Cloning

A pCMV6-AC-GFP EphA2 mammalian expression vector was purchased (Origene, Cat. # RG205725). EphA2NT1296+AsiSIForward primer (TATATAGCGATCGCATGAGCATCAACCAG) was designed to amplify from the 5' end the EphA2 gene after nucleotide 1296 (S432), create point mutation V433M, and add a AsiSI restriction sequence upstream on start codon. EphA2+MluIReverse primer (TATACGCGTGATGGGGATCCC) was designed to

amplify the 3' end of EphA2 with a downstream MluI restriction sequence. The

primers were used to PCR amplify truncated EphA2 using the pCMV6EphA2-

GFP vector. The new PCR amplified gene insert and the template pCMV6-GFP

were restriction digested with AsiSI and MluI-HF and run on an agarose gel. The

resulting bands cut out and purified with gel clean-up kit. The digested insert and

vector were ligated with T4 DNA ligase using a 1:3 vector to insert ratio. The

sequence of the insert in the ligated vector was confirmed via Sanger

sequencing. The resulting vector was named EphA2ΔN-GFP.

Transfection and Western Blot Analysis

Hek293 cells were transfected with 1.5μg of DNA each of EphA2-GFP or

EphA2ΔN-GFP vectors using lipofectamine (Thermofisher, Waltham MA) in a 6-

well plate. 48 hours later, cells were imaged via fluorescence and brightfield

microscopy to check from GFP expression. For Western Blot, cells were lysed

with 50 mM Tris HCl pH 7.5, 100 mM NaCl, 1 mM EDTA, 1% Triton X-100, and

protease inhibitors for 30 minutes on ice. The insoluble fraction was separated

via centrifugation at 10,000 x g for 30 minutes at 4°C. Lysate proteins were then

separated by SDS-PAGE on an 8% polyacrylamide gel and transferred to a 0.45

μm nitrocellulose membrane. Membranes were incubated with 1:1000 anti-

EphA2 rabbit primary antibodies or 1:10000 anti-β-actin mouse primary

antibodies. Membranes were subsequently incubated with 1:5000 anti-mouse

and anti-rabbit IR-dye conjugated secondary antibodies. Secondary antibodies

were detected on an Odyssey Infrared Scanner (Li-Cor Biosciences, Lincoln, NE).

2.4 Results

TYPE7 co-localizes with EphA2 in cells

To determine if TYPE7 co-localizes with EphA2 in cancer cells in culture, we performed experiments by incubating Alexa568 labeled TYPE7 with A375 melanoma cells, fixing the cells, and performing immunohistochemistry to label endogenous EphA2 with an Alexa488 antibody. By imaging with a scanning laser confocal co-localization between TYPE7 and EphA2 could be visualized (Figure 5A). To quantify co-localization, the overlap in signals of Alexa568 and Alexa488 were determined in ImageJ and expressed as a Pearson's correlation coefficient (r) (Figure 5B). A positive correlation between exists between EphA2 and TYPE7 (r = 0.26, n =14) which increased significantly upon receptor activation with ephrinA1-Fc (r = 0.38, n = 17) (p < 0.05). We calculated r for whole images to reduce biases associated to selecting ROIs. We expect that correlation values would be higher for just the plasma membranes of individual cells since a large portion of EphA2 is internalized, whereas TYPE7 is not. These data were validated by experiments showing that TYPE7 co-precipitates with EphA2 and that the amount of TYPE7 co-precipitating with EphA2 increases significantly with the addition of ephrinA1-Fc (49).
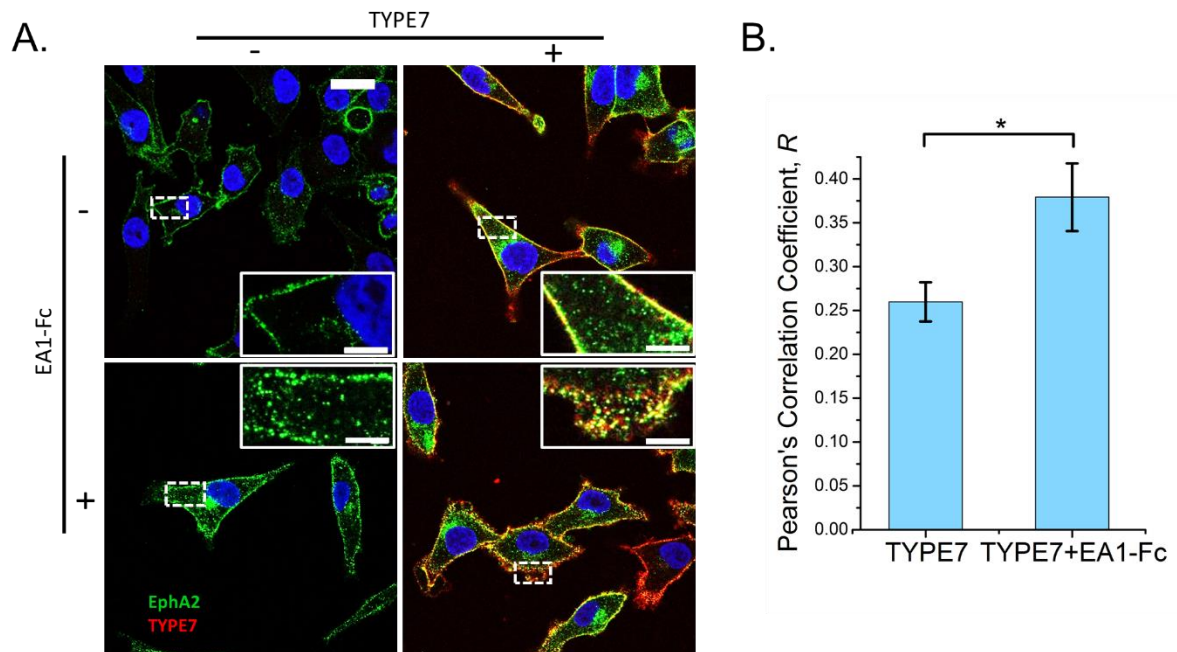
Figure 5. TYPE 7 co-localizes with EphA2 in cancer cells.

A. Representative confocal images of A375 cancer cells treated ± TYPE7-Alexa568 (red) and ± EphrinA1-Fc (EA1-Fc). Cells were fixed and immunostained for EphA2 (green). **B.** Quantification of co-localization of red and green dyes as seen in A via Pearson's Correlation Coefficients. Bars are means ± S.D., n = 3. *p < 0.05, from student's t-test.

Cell contraction studies in fixed cells

Since TYPE7 significantly reduced cell migration (49) we reasoned that other EphA2 signaling-dependent changes in cell behavior and morphology may be induced by TYPE7. Ligand-dependent activation of EphA2 results in dramatic cell rounding and reduction of two-dimensional cell area. We sought to test if TYPE7 also has a similar effect in cancer cells. To do this, we employed cell contraction studies as described by Barquilla *et al.* (167). We initially conducted these experiments in A375 melanoma cells to be consistent with the cell line used in the cell migration assays. Cells were treated with TYPE7 and ephrinA1-Fc, stained and imaged (Figure 6A). For these initial experiments, cells were measured by hand in ImageJ (Figure 6B and C). These experiments and results yielded significant differences between control and TYPE7 treated cell. However, there were concerns about the relatively small number of cells measured and bias introduced due to manual measurements. It was decided that a more high-throughput and unbiased method of measuring cell area would provide more valid data.

We then implemented the open source software, CellProfiler, to measure cell contraction in A375 cells. We also investigated another measure of cell morphology, eccentricity, which is another output of the CellProfiler pipeline we used. Eccentricity if a measure of how circular an object is. An eccentricity value of 0 is a perfect circle where an eccentricity value of 1 is a parabola. We found
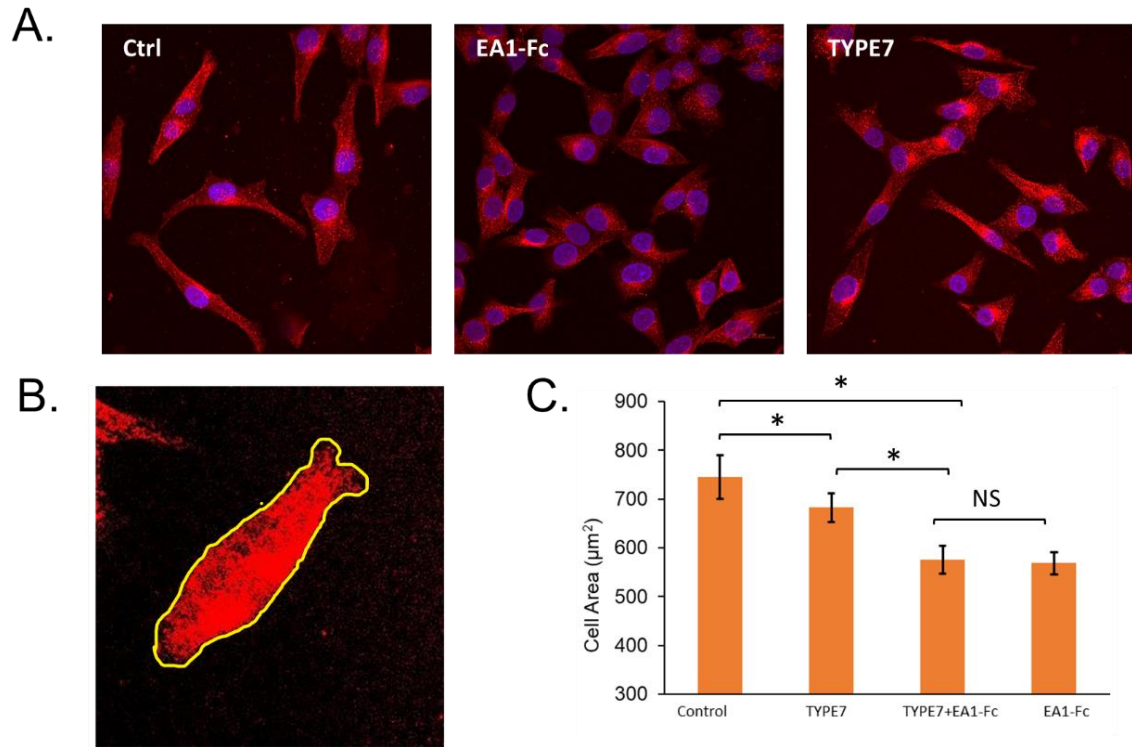
Figure 6. Initial cell area measurements in A375 cells.

A. Representative confocal images of control, 0.5 µg/mL ephrinA1-Fc, and 2 µM TYPE7 treated A375 cells. Actin is label by phalloidin (red) and nuclei are stained with Dapi (blue). **B.** Representative image showing manual measurement of cell area as conducted in ImageJ. **C.** Average cell areas for treated cells as measured manually in ImageJ. Bars are means ± S.D. * $p < 0.05$, as determined by ANOVA and Tukey post-hoc test, $n = 3$.
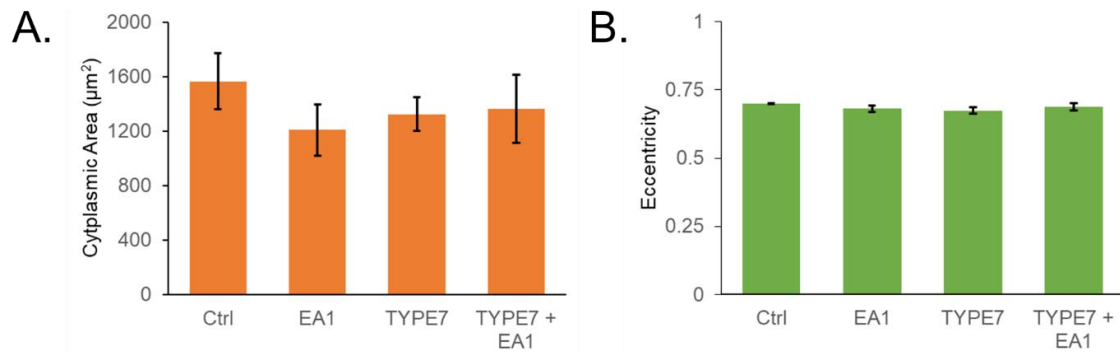
Figure 7. Automated cell area and eccentricity of A375 cells.

A. Cytoplasmic area of treated A375 cells measure from confocal images using CellProfiler. Bars are means ± S.D. **B**. Eccentricity of treated A375 cells as measured in CellProfiler. Bars are means ± S.D.

that there were no significant changes in cytoplasmic area (Figure 7A) or eccentricity (Figure 7B) in A375 cells treated with ephrinA1 or TYPE7. We also noticed that the relative change is area of A375 between control and ephrinA1-Fc treatment was not as large as in published images of contracted PC-3 cells (167).

Thus, we moved forward with conducting experiments in PC-3 cells (Figure 8A) and measuring using the automated cell measuring software, CellProfiler. With this new method, we found that ephrinA1-Fc did significantly increase cell contraction (Figure 8B) in agreement with previously published data (167). While it consistently appeared that TYPE7 induced cell contraction, the change was never significant when compared to the Fc control. We believed this was due to the high level of heterogeneity in cell sizes across the population.

Cell contraction studies in live cells

Studies in fixed cells gave results which had too high of a degree of variability to determine any statistical significance. We also did not know if maximal cell contraction was reached for most cells during the 10-minute treatment prior to fixation. We reasoned that measuring cell contraction of individual live cells might yield more reproducible results. Thus, we designed an experimental set-up in which a small number of cells would be imaged (Figure 9A) before and during treatment so their size could be tracked over time. What we found was that not all cells reached maximal contraction at the same time post-treatment (Figure 9C). On a given day, cells might reach their maximal
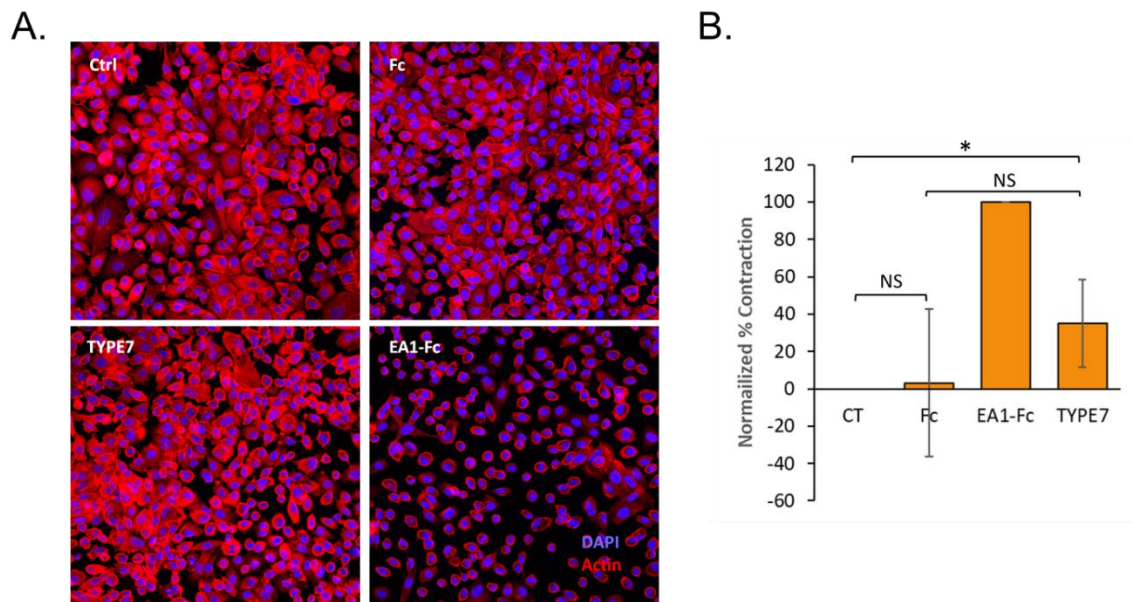
Figure 8. Cell contraction observed in PC3 cells.

A. Representative confocal images of PC-3 cells treated ± 0.5 µg/mL ephrinA1-Fc (EA1-Fc) and ± 2 µM TYPE7. Actin is labeled with phalloidin (red) and nuclei are stained with Dapi (blue). **B.** Normalized cell contraction quantified using cytoplasmic areas from CellProfiler from confocal images. Bars are means ± S.D. * $p < 0.05$, from ANOVA and Tukey post-hoc tests, $n = 3$.

contracted size after 10 minutes (Figure 9C, orange line) of ephrinA1-Fc or 20 minutes (Figure 9C, blue line) of ephrinA1-Fc. The relative percentage of total area that cells contracted was also highly variable. On some days, cells contracted around 10% to 60% (Figure 9C). On other days, the cells showed very little to no contraction when treated with ephrinA1-Fc. At this point, we chose to stop pursuing this line of investigation.

Cloning of truncated EphA2

To test our hypothesis that TYPE7 could activate MMP cleaved EphA2 we sought to generate stable cell lines expressing both full-length (as a control) and N-terminal truncated EphA2. MT1-MMP is known to cleave EphA2 at 4 sites (165). For our N-terminal truncation, we chose to recapitulate the S-^{423}V cleavage site. An EphA2-GFP expression vector was modified by site-directed-mutagenesis to produce EphA2ΔN. Cell lines in which the WT EphA2-GFP and the EphA2ΔN-GFP are stably expressed in HEK293 cells were produced. HEK293 cells were chosen for their negligible endogenous EphA2 expression (168). Imaging of GFP fluorescence in cells confirmed expression and localization of both constructs (Figure 10A) while Western Blot analysis confirmed the length of EphA2 produced by both cell lines (Figure 10B). However, it appears that EphA2ΔN-GFP did not primarily get trafficked to the plasma membrane. We saw significant cytoplasmic and ER levels of GFP. Total EphA2 levels for both constructs show differences as can be seen in Figure 10B with the WT construct having a larger band than the ΔN construct.
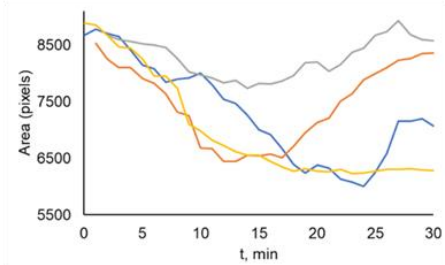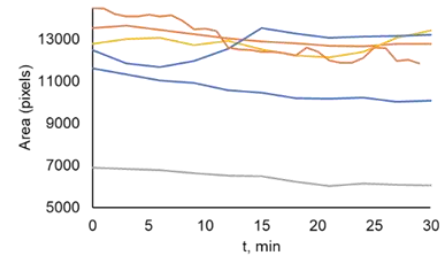
Figure 9. Live cell contraction measurements.
A. Representative live PC-3 cells at low confluency imaged by phase contrast.
B. and **C.** Cell areas measured over time from live-cell videos taken after stimulation with 0.5 μg/mL ephrinA1-Fc for 30 minutes on two different days.
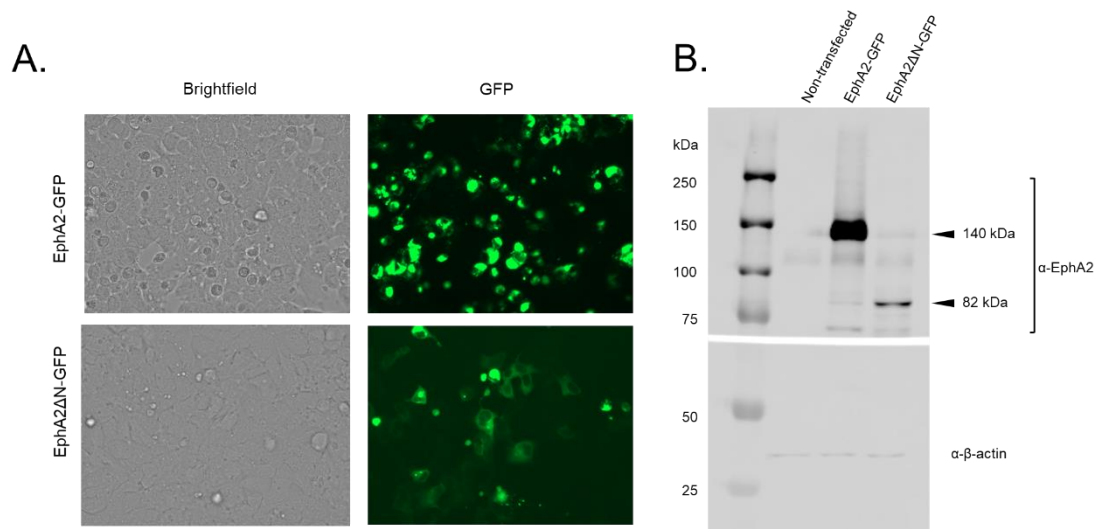
Figure 10. Expression of truncated and WT EphA2-GFP vectors.

A. Brightfield and epifluorescence images of Hek293 cells transfected with EphA2-GFP and EphA2ΔN-GFP 48 hours after transfection. **B.** Western blot of transfected Hek293 cells showing no expression of EphA2 in untransfected cells (first lane), full-length EphA2-GFP (second lane), and the smaller truncated EphA2ΔN-GFP (third lane). Expected molecular weights are indicated at arrows. β-actin was blotted for as a loading control.

2.5 Discussion

Here we investigated how TYPE7 interacts with EphA2 in cancer cells. We showed via fluorescence microscopy and co-localization analysis that TYPE7 associates with EphA2 in cancer cells. Further, this association was increased upon addition of ephrinA1. These results were supported by co-immunoprecipitation experiments which confirmed a direct interaction between EphA2 and TYPE7. It was also seen in these experiments that ephrinA1 increased the amount of TYPE7 that co-precipitated with EphA2 (49). We propose that the increase in co-localization relates to the formation of large EphA2 signaling clusters which occurs upon stimulation with ephrinA1 (123, 169). If TYPE7 binds to one interface of the EphA2 TMD it is possible that as another interface forms dimers that the peptide gets pulled into the signaling clusters. Sequestration of the peptide in receptor clusters would disrupt any equilibrium dissociation that would occur outside of clusters. This could explain why less TYPE7 is co-localized with EphA2 under basal conditions.

We next sought to determine if TYPE7 could induce cell rounding and contraction similar to ephrinA1. Although initial experiments with a small number of cells indicated that TYPE7 promoted an intermediate level of contraction in A375 cells, further high-throughput analysis in A375 and PC-3 demonstrated that TYPE7 had no significant effect on cell contraction. We observed a large heterogeneity in cell sizes which may have been due to differences in cell cycle and the kinetics of individual cell responses to treatment. Conducting

experiments in live-cell experiments were further complicated by experimental artifacts. No robust effect on cell contraction was observed even though TYPE7 was shown to have a very robust effect on cell migration which are both expected outcomes of EphA2 tyrosine phosphorylation (130). This may be due to the fact that TYPE7 promotes the phosphorylation of only Y772.

As has been shown for FGFR, specific adaptor proteins bind to specific phosphorylated residues or patterns of phosphorylated residues in ligand-activated RTKs (72, 73). It may be that phosphorylation of Y772 is sufficient to recruit the adaptor proteins and down-stream signaling activators which are responsible for reducing cell migration. This would mean that in order to promote cell contraction to the same degree as ephrinA1, a different tyrosine or combination of tyrosines must be phosphorylated.

We had hoped to further characterize the ability of TYPE7 to inhibit cell migration by demonstrating that it could modulate the activity EphA2 cleaved by MT1-MMP. Toward this goal, I successfully cloned and expressed an N-terminal truncated EphA2-GFP construct. The site of truncation was chosen to mimic one of the known MT1-MMP cleavage sites. However, imaging indicated issues with trafficking of the truncated protein. It may be that the levels of expression for this construct are too high for the protein to be correctly folded resulting in the altered trafficking and degradation.

Alternatively, it is possible that removal of the predicted signal peptide (residues 1-23) at the N-terminus of EphA2 greatly reduces the ability of the

protein to be targeted to the plasma membrane. Although not every membrane

protein has a signal peptide, they are known to partition into lipid bilayers and

greatly enhance the efficiency of membrane insertion in addition to ensuring

correct membrane topology (170). It is possible through modifications to the

vector (to modulate expression levels) and EphA2 sequence (addition of the

signal peptide) we could render a construct which gets efficiently trafficked to the

plasma membrane.

Chapter III.
PIP$_2$ promotes conformation-specific dimerization of the EphA2 membrane region

3.1 Abstract

The EphA2 receptor exhibits two activation states: anti-tumorigenic ligand-dependent activation, and pro-tumorigenic ligand-independent activation. Evidence suggests that in these two states the transmembrane domain (TMD) dimerizes via two distinct helical interfaces: the ligand-independent dimer mediated by a heptad repeat motif and the ligand-dependent dimer mediated by a glycine zipper. It has also been proposed that positively charged residues on the intracellular juxtamembrane (JM) segment interact with negatively charged phosphatidylinositol 4,5-bisphosphate (PIP_2) lipids on the inner leaflet of the plasma membrane. Here we investigate the coupling of the TMD and JM in different lipid environments. We devised a method enabling us to study the two putative signaling conformations of a peptide comprised of TMD and JM residues of EphA2 by varying membrane thickness using 14:1 PC and 22:1 PC. We found that bilayer thickness alters the environment of the JM residues but not distance from the bilayer surface. In thick bilayers addition of PIP_2 results in changes to JM environment and headgroup distance which appears to be driven by PIP_2 clustering around the basic JM residues. No effect of PIP_2 on the JM was observed in thin bilayers. Using a novel single-molecule TIRF technique we observed that in thick bilayers PIP_2 promotes TMD dimerization. This effect on self-assembly was not observed in thin bilayers or in thick bilayers containing another negatively charged lipid, phosphatidylserine. These data suggest that

PIP$_2$ exerts a specific regulatory effect on EphA2 through interactions with the JM in the ligand-independent state.

3.2 Introduction

The Eph receptor tyrosine kinases (RTKs) are the largest family of RTKs in humans. Eph receptors are involved in tissue patterning during embryonic development, neuronal plasticity, and wound healing (130, 171). Beyond their normal physiological functions, Eph receptors can contribute to human diseases. For example, elevated EphA4 signaling results in neuronal damage in Alzheimer's disease and amyotrophic lateral sclerosis (ALS) (90, 98, 101, 102), and loss of EphB2/B3 signaling is implicated in skeletal malformations that cause cleft palate (172). Moreover, a large body of research exists establishing that Eph receptors are overexpressed in a variety of cancer types. Specifically, EphA2 overexpression is found in breast, ovarian, prostate, and pancreatic cancers and is correlated with aggressive tumors, high rates of tumor recurrence, and poor patient prognosis (104–108, 110, 173). Additionally, Eph receptors have been found to be cellular receptors for viruses that cause cancer. For example, EphA2 is a receptor for Kaposi's sarcoma-associated herpes virus and Epstein-Barr virus (114, 174).

EphA2 signaling pathways control cell proliferation, migration, and cell retraction (119). EphA2 engages in two modes of signaling: ligand-dependent and ligand-independent (i.e. non-canonical). Ligand-dependent signaling requires activation of EphA2 by binding of its ligand, ephrinA1, resulting in the

phosphorylation of residues Y588, Y594 and Y772. This results in signaling that inhibits metastatic phenotypes by causing cell retraction/rounding and decreasing cell proliferation and migration (124, 129, 130). Conversely, ligand-independent signaling is responsible for tumorigenic phenotypes and occurs via phosphorylation of S897 by the kinases AKT, RSK, or PKA (124–127). Overexpression of EphA2 in cancers is often accompanied by a loss of ephrin ligand (120, 121). It is believed that this imbalance of EphA2 and ephrin results in both increased ligand-independent signaling and a decrease in ligand-dependent signaling, promoting tumor growth and malignancy (175).

Due to its prominent role in tumorigenesis, EphA2 has become an attractive drug target and, as such, an active area of research. The structure of EphA2 includes an extracellular ligand binding domain, a single pass transmembrane domain (TMD), and an intracellular kinase domain connected to the TMD by a disordered juxtamembrane (JM) segment. In the ligand-independent state, EphA2 exists in a monomer-dimer equilibrium (176). Upon binding of ephrinA1, dimerization via the ligand-binding domains is promoted and leads to the formation of signaling clusters (56). While many aspects of Eph receptor signaling have been elucidated, the exact molecular details of how the receptor transmits an extracellular signal across the plasma membrane remain unknown. As a membrane spanning receptor, the TMD must play a role in conferring signals across the plasma membrane.

An NMR structure of the EphA2 TMD dimer was solved by Bocharov *et al.* (137). It was found that this dimer had a small interhelical crossing angle (15°) and the interface was mediated by a heptad repeat (HR) motif. The same study conducted molecular dynamics (MD) simulations on the NMR structure and found that the EphA2 TMD dimer could rotate to a glycine zipper (GZ) interface with a larger interhelical crossing angle (45°). It was then hypothesized that the receptor switches between these two conformations with different dimerization interfaces. In a follow-up study, it was reported that mutations in the HR motif decreased ligand-independent signaling while mutations in the glycine zipper decreased ligand-dependent signaling (22). These findings combined with the structural data gave rise to the following model: In the ligand-independent signaling state the EphA2 TMD dimerizes via the HR motif with nearly parallel TMDs, while in the ligand-dependent signaling state, EphA2 dimerizes via the GZ with tilted helices (22, 137). It is unknown how the switch in dimerization interface and opening of the interhelical crossing angle participate in conferring the extracellular signal from the outside of the cell to the cytoplasm. It is further unknown how the JM responds to changes in the TMD.

JM-lipid interactions play a role during the activation of several receptors. These interactions are believed to be mediated by positively charged JM residues interacting with negatively charged lipid head groups. For EphA2, associations between basic JM residues and phosphatidylinositol 4,5-bisphosphate (PIP_2) have been computationally predicted (159). Notably, the first

five positively charged residues (HRRRK) of the EphA2 JM are predicted to have strong interactions with the negatively charged PIP_2. However, this association has not been examined experimentally. The interaction of the JM with PIP_2 might regulate the activity of EphA2, since the two signaling modalities of EphA2 alter PIP_2 levels. Ligand-dependent signaling activates PI3K which phosphorylates PIP_2 to generate PIP_3. While ligand-independent signaling recruits SHIP2 which converts PIP_3 to PIP_2 and can be triggered by AKT upon PI3K activation (119). However, it is unknown if these local changes in PIP_2 directly alter EphA2 signaling.

In the present study, we investigate how the TMD and JM regions of EphA2 are affected by signaling-related changes in TMD orientation and lipid environment. We use hydrophobic matching to stabilize the two signaling modalities of the EphA2 TMD region. We also examine how bilayer composition affects the environment and position of JM residues. Our findings show that bilayer thickness drives differences in the environment of the JM, while addition of PIP_2 alters the distance of the JM to the bilayer. We also examine how bilayer composition affects self-assembly of the TMD of EphA2 using a novel single molecule approach with styrene maleic acid lipid particles (SMALPs). Our results indicate that PIP_2 promotes dimerization only in thick bilayers via interactions with the JM. Implications for the role of lipids in the two signaling states of EphA2 are discussed.

3.3 Methods

Liposome Preparation

Lipids were purchased from Avanti Polar Lipids, Alabaster, AL. 14:1 PC (1,2-dimyristoleoyl-*sn*-glycero-3-phosphocholine), 22:1-PC (1,2-dierucoyl-*sn*-glycero-3-phosphocholine), PIP_2 (L-α-phosphatidylinositol-4,5-bisphosphate (Brain, Porcine)), 18:1 dansyl-PE (1,2-dioleoyl-*sn*-glycero-3-phosphoethanolamine-*N*-(5-dimethylamino-1-naphthalenesulfonyl), POPC (1-palmitoyl-2-oleoyl-glycero-3-phosphocholine), biotin-PE (1-oleoyl-2-(12-biotinyl(aminododecanoyl))-*sn*-glycero-3-phosphoethanolamine), PIP_2 Bodipy FL (Echelon Biosciences, Salt Lake City, UT) stocks were prepared in chloroform. Aliquots of lipids were dried under argon gas and then placed in a vacuum overnight. Unless otherwise noted lipid films were resuspended with Buffer A: 19.3 mM HEPES (4-(2-hydroxyethyl)-1-piperazineethanesulfonic acid) buffer (pH 7.5), 1 mM EGTA (ethylene glycol-bis(β-aminoethyl ether)-*N,N,N′,N′*-tetraacetic acid), and 5 mM DTT (dithiothreitol) . Large unilamellar vesicles (LUVs) were formed by extrusion with a Mini-Extruder (Avanti Polar Lipids, Alabaster, AL) through a 100 nm pore size membrane (Whatman, United Kingdom).

Peptide Conjugation

The TMJM peptide was synthesized by F-moc chemistry by ThermoFisher (Waltham, MA), and purity (>95%) was assessed by MALDI-TOF and HPLC. The cysteine of TMJM was conjugated to Alexa Fluor 488 or Cyanine5, using a C_5 maleimide moiety (Molecular Probes, Eugene OR). The reaction was carried out

by adding a molar excess (peptide:dye of 1:1.1 moles) of dye dissolved in 100 mM sodium phosphate pH 7.6 to a peptide stock in 2,2,2-trifluoroethanol (TFE). Unreacted dye was removed by HPLC by injecting the TFE mixture onto a semi-preparative Agilent Zorbax 300 SB-C18 column on an Agilent 1200 HPLC system (Santa Clara, CA). The gradient of water + 0.05% trifluoroacetic acid (TFA) to acetonitrile + 0.05% TFA was 30 min from 0% - 100% acetonitrile. The conjugated peptide eluted around 95% acetonitrile. The collected fractions from HPLC were frozen and lyophilized. The dry conjugated peptide was resuspended in hexafluoroisopropanol (HFIP).

Oriented Circular Dichroism

A stock of TMJM was prepared in TFE. Aliquots of 2.23×10^{-7} moles of 14:1 PC or 22:1 PC were dried under argon then vacuum desiccated for at least 2 hours. The appropriate amount peptide stock (for a 50:1 or 300:1 lipid to peptide molar ratio) was added, dried with argon then dried under vacuum at least 2 hours. The lipid-peptide film was resuspended with 400 µl TFE and 150 µl spread on each of two circular quartz slides (Hellma Analytics, Germany). To allow for even solvent evaporation, the slides were placed in a fume hood overnight and further dried under vacuum for at least 6 hours to ensure complete evaporation of the TFE. The samples were hydrated under argon with 150 µl per slide of Buffer A overnight in 96% relative humidity, to obtain supported bilayers. Excess buffer was removed, and the hydrated slides were assembled in an OCD cell, with an inner cavity filled with saturated K_2SO_4 to keep the bilayers humidified. The OCD

spectra were recorded on a Jasco J-815 spectropolarimeter at room temperature. For each sample eight 45° rotations of the cell were averaged. Appropriate lipid backgrounds were subtracted in all cases.

Tryptophan Fluorescence

13 mm glass culture tubes (Fisher Scientific) were cleaned with piranha (75% H_2SO_4, 25% H_2O_2) solution for 3 minutes creating a hydrophilic surface to promote efficient removal of peptide. Appropriate amounts of 100% 22:1 PC/14:1 PC or 3 mol% PIP_2 and 97 mol% 22:1 PC/14:1 PC stocks were added to the cleaned tubes and dried under argon. Next, the lipids were dried under vacuum for at least 2 hours before the appropriate amount of peptide stock was added to achieve a lipid to peptide molar ratio of 300:1 and subsequently dried under vacuum overnight. Films were resuspended in Buffer A for an initial peptide concentration of 4 µM and extruded. To maximize peptide recovery, resuspension was conducted in three stages. First, 50% of the buffer volume was added to the tube then vortexed for 45 sec. This buffer was removed then the procedure was repeated twice with 25% of the final buffer volume. Equivalent lipid blanks were also prepared. To ensure that amounts of lipids between blanks and proteoliposomes were equal, ammonium molybdate phosphate assays were performed to quantify lipids (177). If necessary, lipid blank concentrations were appropriately adjusted. LUVs were then diluted to 300 µM lipid and 1 µM peptide and 5 mM $CaCl_2$ (where indicated). Samples were incubated for a minimum of 1 hour at room temperature to allow calcium levels to equilibrate across the bilayer.

Tryptophan fluorescence spectra were then collected on a Cary Eclipse

Fluorescence Spectrophotometer (Agilent Scientific, Santa Clara, CA) using an

excitation wavelength of 290 nm. Lipid blanks were subtracted in all cases.

Trp-DNS FRET

Lipids and peptide were dried in piranha-cleaned glass tubes as described

above. Films were resuspended as described above in Buffer A for an initial

peptide concentration of 4 µM. Equivalent lipid blanks were also prepared.

Liposomes and proteoliposomes containing 0% and 10% dansyl-PE were mixed

in appropriate ratios and subjected to seven rounds of freeze thaw to achieve

0%, 0.25%, 0.5%, 1%, 2%, 3%, and 5% dansyl-PE, +/- 1 µM peptide, and +/- 5

mM $CaCl_2$ final concentrations where indicated. Samples were incubated at room

temperature for a minimum of 1 hour to allow calcium levels to equilibrate. FRET

experiments were conducted on a Cary Eclipse Fluorescence Spectrophotometer

(Agilent Scientific, Santa Clara, CA) using an excitation wavelength of 290 nm.

Calcium Influx Assay

 POPC vesicles were prepared by resuspending dried POPC with Buffer A, and

0.1 mM Indo-1 (1H-Indole-6-carboxylic acid, 2-[4-[bis-(carboxymethyl)amino]-3-

[2-[2-(bis-carboxymethyl)amino-5-methylphenoxy]ethoxy]phenyl]-,

pentapotassium salt). LUVs were formed via extrusion as described above. To

separate encapsulated Indo-1 and free Indo-1, LUVs were subjected to size

exclusion chromatography on a sephadex G25 PD-10 column (GE Life Sciences,

Chicago, Il). The concentration of the encapsulated Indo-1 was estimated using

fluorescence and known amounts of free Indo-1. Indo-1 containing LUVs were diluted to a final Indo-1 concentration of 0.05 µM in Buffer A and 5 mM $CaCl_2$ was added. Calcium influx was observed in a Cytation5 plate reader (BioTek, Winooski, VT) as a shift in fluorescence maximum from 485 nm to 405 nm. Calcium influx saturated after 5 minutes. Free dye with 5 mM $CaCl_2$ and encapsulated dye with 0.1% Triton X-100 were used as controls.

SMALP preparation

For photobleaching experiments, peptide and lipid films were prepared by drying down 22:1 PC or 14:1 PC + 3% biotin-PE ± 3% PIP_2 or 10% POPS from chloroform stocks. To this TMJM conjugated with Alexa 488 in HFIP was added. For co-localization experiments, lipids and peptides were prepared the same way as in photobleaching experiments with PIP_2 Bodipy FL and TMJM conjugated to Cy5. The amount of lipid was kept constant while the amount of peptide was adjusted for the specified lipid to peptide ratio (300:1, 100:1 or 50:1). The films were dried under argon gas, then vacuum-desiccated for at least two hours. MLVs were then formed by resuspending in SMALP buffer (19.3 mM HEPES, 150 mM NaCl, 1 mM EGTA). MLVs were subjected to three rounds of freeze-thaw at -80 °C and 42 °C to ensure even mixing of the lipid components. A stock solution of 1-9 mg/mL of SMA 2000H (Polyscope, Geleen, The Netherlands) was diluted to 0.3 mg/mL and added to MLVs for a SMA final concentration of 0.075 mg/mL and lipid concentration of 100 µM. The MLV/SMA solution was then incubated overnight with shaking to allow SMALP formation.

Single molecule TIRF

Quartz microscope slides (G. Finkenbeiner Inc., Waltham MA) and coverslips were cleaned following the protocol of Chandradoss *et al.* 2014 (178). Clean slides and coverslips underwent animosalinization and pegylation following a procedure previously described (179). In short, slides were incubated with a solution of 93% methanol, 4.5% acetic acid and 2.5% 3-(triethoxysilyl)-propylamine (EMD Millipore Corp., Billerica, MA), rinsed with methanol and water and finally dried under a stream of nitrogen (179). A solution of m-PEG-SVA and biotin-PEG-SVA (Laysan Bio Inc., Arab, AL) was made by dissolving 20% w/v m-PEG and 1.25% biotin-PEG in filtered 100 mM $NaHCO_3$ overnight. To assemble a flow chamber, slides were pre-drilled with holes and fitted with a coverslip using double sided tape and sealed with vacuum grease. Pegylated slides were incubated for 10 min with 0.2 mg/mL streptavidin, and then washed with SMALP buffer. SMALPs, containing a peptide concentration of 20-30 nM, were immobilized on the slides for 10 min and then rinsed to remove any nonspecific interactions. The rinse buffer was replaced with an oxygen scavenging system; 2.5 mM PCA and 250 nM rPCO (recombinant Protocatechuate 3,4-Dioxygenase; Oriental Yeast Co., Tokyo Japan) in SMALP buffer with 2 mM Trolox (180). Slides were imaged under a custom-based TIRF microscope and the emission intensities were collected on CCD camera (Andor Technology) with 100 ms integration time. A custom written software package (downloaded from https://physics.illinois.edu/cplc/software) was used to record movies and extract

single-molecule traces using scripts written in IDL (Harris Geospatial Solutions, Inc) software (181). Single-molecule traces were assessed and analyzed using custom software written in Python and analyzed to determine the number of photobleaching steps. To prevent potential bias, the experimenter was blinded during analysis with a custom data-shuffling Python script.

SDS-PAGE

Lipid-peptide films were prepared for SDS PAGE as described above with unlabeled TMJM peptide at a lipid to peptide ratio of 300:1. Dried lipid-peptide films were resuspended in 19.3 mM HEPES, 1 mM EGTA and shaken at room temperature for 3 hours to allow disulfide bond formation. To the MLVs, SDS buffer was added for a final SDS concentration of 150 mM. To this, sample buffer +/- DTT was added. Samples were then boiled for 5-10 minutes to ensure complete disruption of liposomes. To ensure the stock of peptide did not contain disulfide-mediated dimers, a sample of the TMJM stock was also prepared without lipid. This sample was resuspended in buffer containing 150 mM SDS and loaded with sample buffer without DTT. Samples were run on a 16% tricine gel and stained using a Peirce Silver Stain Kit (Thermo Scientific, Waltham MA). Bands were quantified in ImageJ using the Band Peak Quantification plugin.

Transmission Electron Microscopy

SMALPs were prepared as described above to a final lipid concentration of 1 mM. 3% w/w SMA was used added to both lipids before overnight equilibration. SMALPs of 14:1 PC were equilibrated with shaking at room temperature

overnight while 22:1 PC SMALPs were incubated at 60 °C for the same duration. SMALPS were imaged with negative staining TEM. Small aliquots of SMALPs were adsorbed on to glow discharged carbon-coated copper EM grids (Electron Microscopy Sciences, Hatfield, PA) for 120 s. Grids were washed twice with ddH$_2$O for 15 s before negative staining with UranyLess (Electron Microscopy Sciences, Hatfield, PA) for 45 s. Excess liquid was removed from the grid with filter paper between steps. Grids were air-dried prior to examination on a JEOL JEM 1400-Flash TEM (JEOL USA, Peabody, MA) operating at 80 kV. SMALPs were measured in ImageJ.

Statistical Analysis

All statistical comparisons were made in IBM SPSS v25 software (Armonk, New York USA). Where only two means were compared, student's t-tests were used. Where more than two means were compared one-way analysis of variance (ANOVA) were conducted followed by post-hoc comparisons, with Tukey HSD tests where data were homoscedastic, and Dunnett's t-test where data were heteroscedastic. All *p*-values reflect an α = 0.05. Where no *p*-values are shown the difference is not significant.

3.4 Results

Bilayer thickness drives changes in TM orientation

We sought to generate an *in vitro* model of the ligand-independent and ligand-dependent signaling states of the membrane region of the EphA2 (Figure 11A). To this end, we used the TMJM peptide, which comprises a short stretch of

66

A.

B.
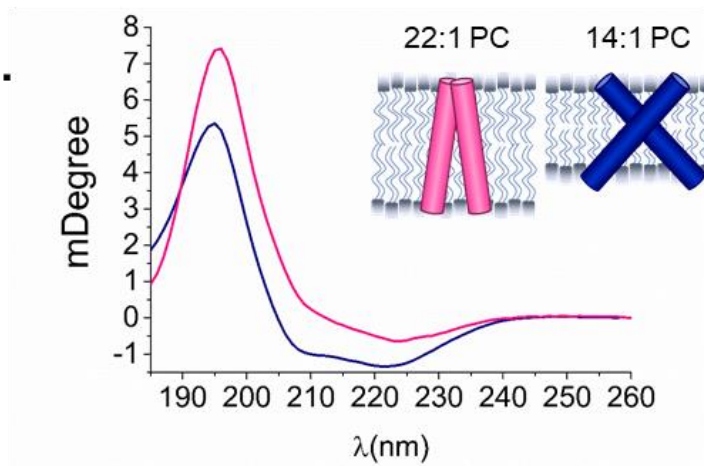
Figure 11. Bilayer thickness drives differences in TMJM helical tilt.

A. Sequence of the TMJM peptide comprised of EphA2 residues 531-563 with added CWN residues at the C-terminus. **B.** OCD spectra of TMJM in 22:1 PC (fuchsia) and 14:1 PC (navy). Inset: model of the conformations of TMJM in 14:1 PC and 22:1 based on OCD data.

extracellular residues, the TMD and first 5 JM residues of EphA2. At the C-terminus we added a cysteine to enable dye conjugation, and a tryptophan as a fluorescent reporter of the JM segment. As noted above, the two EphA2 signaling configurations have different inter-helical crossing angles. To promote the different configurations, we used model membranes composed of 14:1 PC or 22:1 PC, which only differ in the length of their acyl chains. Since 22:1 PC contains 8 more tail carbons than 14:1 PC, it forms thicker bilayers (45.5 Å vs. 29.6Å) (182). Our hypothesis was that we could use hydrophobic matching to stabilize the TMD of EphA2 in the two different conformations (183). Specifically, TMJM would orient closer to the bilayer normal in a thick bilayer (22:1 PC), while it would tilt further away from the bilayer normal in a thin (14:1 PC) bilayer. Thus, we sought to use bilayer composition to tune helical tilt and recapitulate the ligand-independent and ligand-dependent signaling configurations.

We used oriented circular dichroism (OCD) to test the effects of bilayer thickness on the helical tilt of TMJM which had been reconstituted in supported lipid bilayers composed of 14:1 PC or 22:1 PC. Fig. 1B shows that the obtained OCD spectra had two α-helical minima indicating a transmembrane orientation. To assess the helical tilt, we can examine the OCD spectra at the 208 nm minimum. A more positive value indicates a less tilted helix, as seen in 22:1 PC, while a lower value indicates a more tilted helix, as seen in 14:1 PC (Figure 11B) (184–186). These data indicate that, on average, the TMDs are more vertical in

thicker bilayers, like the ligand-independent signaling configuration. In contrast, the TMDs are more tilted in thinner bilayers, which might correspond to the ligand-dependent signaling state. The observed changes in tilt were independent of lipid to peptide ratio and were also observed at lower peptide concentrations (Figure 12B). Standard circular dichroism was performed on TMJM in 14:1 PC and 22:1 PC vesicles to ensure that the secondary structure of the peptide was the same in both lipids (Figure 12A). The OCD results suggest that the peptide responds to being placed in bilayers of different thickness by adjusting the interhelical crossing angle, providing a means to further study the two observed conformations.

TMJM can form dimers in thin and thick bilayers

We wanted to investigate if TMJM self-assembled into biologically relevant dimers. To this end we developed a single-molecule photobleaching method using SMALPs. TMJM labeled with the fluorescent dye Alexa Fluor 488 was reconstituted in multilamellar vesicles (MLVs) composed of either 14:1 PC or 22:1 PC containing traces of biotinylated phosphatidylethanolamine (biotin-PE). The MLVs were then incubated with styrene maleic acid (SMA). SMA forms a polymer belt around units of lipid bilayer and proteins (Figure 13A) (187, 188). Transmission electron microscopy confirmed that lipid composition did not alter SMALP size and co-localization experiments confirmed SMALP composition (Figure 14 and Figure 15D-E). SMALPs were immobilized on a microscope slide
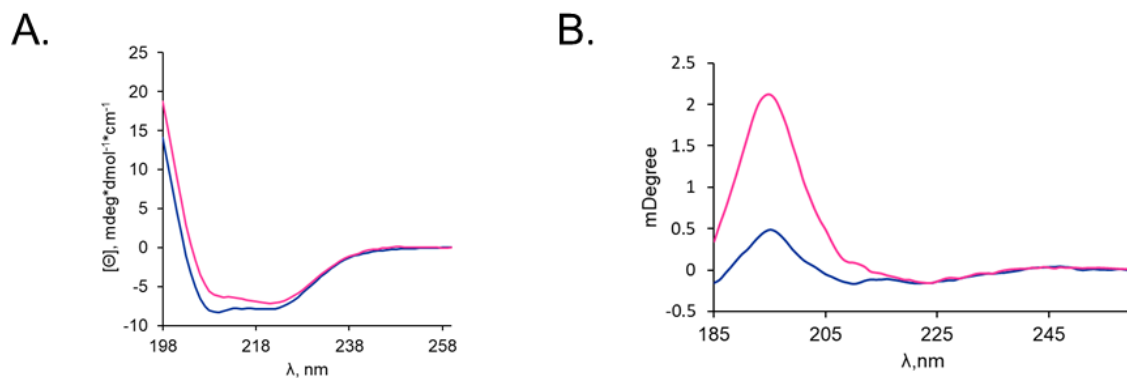
Figure 12. CD and OCD TMJM controls.

A. CD of TMJM in 22:1 PC (fuchsia) and 14:1 PC (navy) liposomes at a lipid to peptide ratio of 50:1 showing secondary structure in both lipids is α-helical. **B.** OCD of TMJM in 14:1 PC (navy) and 22:1 PC (fuchsia) at a lipid to peptide ratio of 300:1.
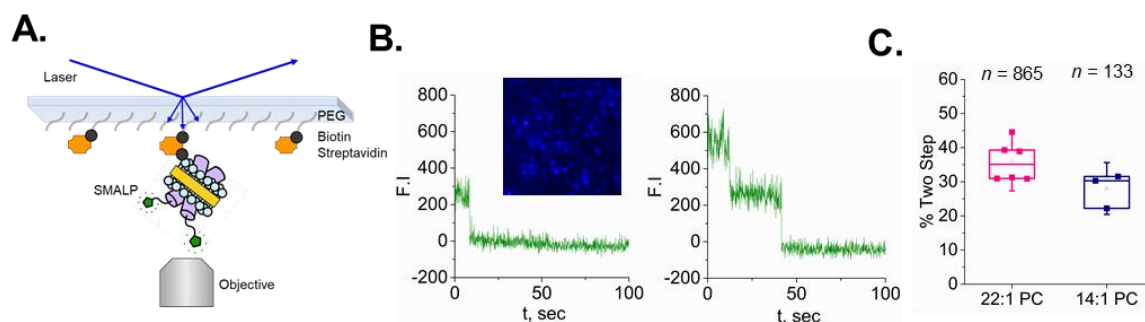
Figure 13. TMJM dimerization observed by single-molecule TIRF of SMALPS.

A. Schematic of TIRF experimental setup. SMALP showing SMA polymer (yellow) encircling lipids (blue) containing TMJM peptides (purple) labeled with Alexa488 (green), immobilized on a PEGylated slide via a biotin (black) and streptavidin (orange) linkage. **B.** Representative fluorescence traces showing one (left) and two (right) photobleaching steps. Representative TIRF image of SMALPs (inset). **C.** Box and whiskers plot showing percentages of peptide counted in traces with two photobleaching steps in 22:1 PC and 14:1 PC at a lipid to peptide ratio of 300:1. Data are from 3-6 independent experiments ± S.D, *n* is total number of traces counted with two photobleaching steps.
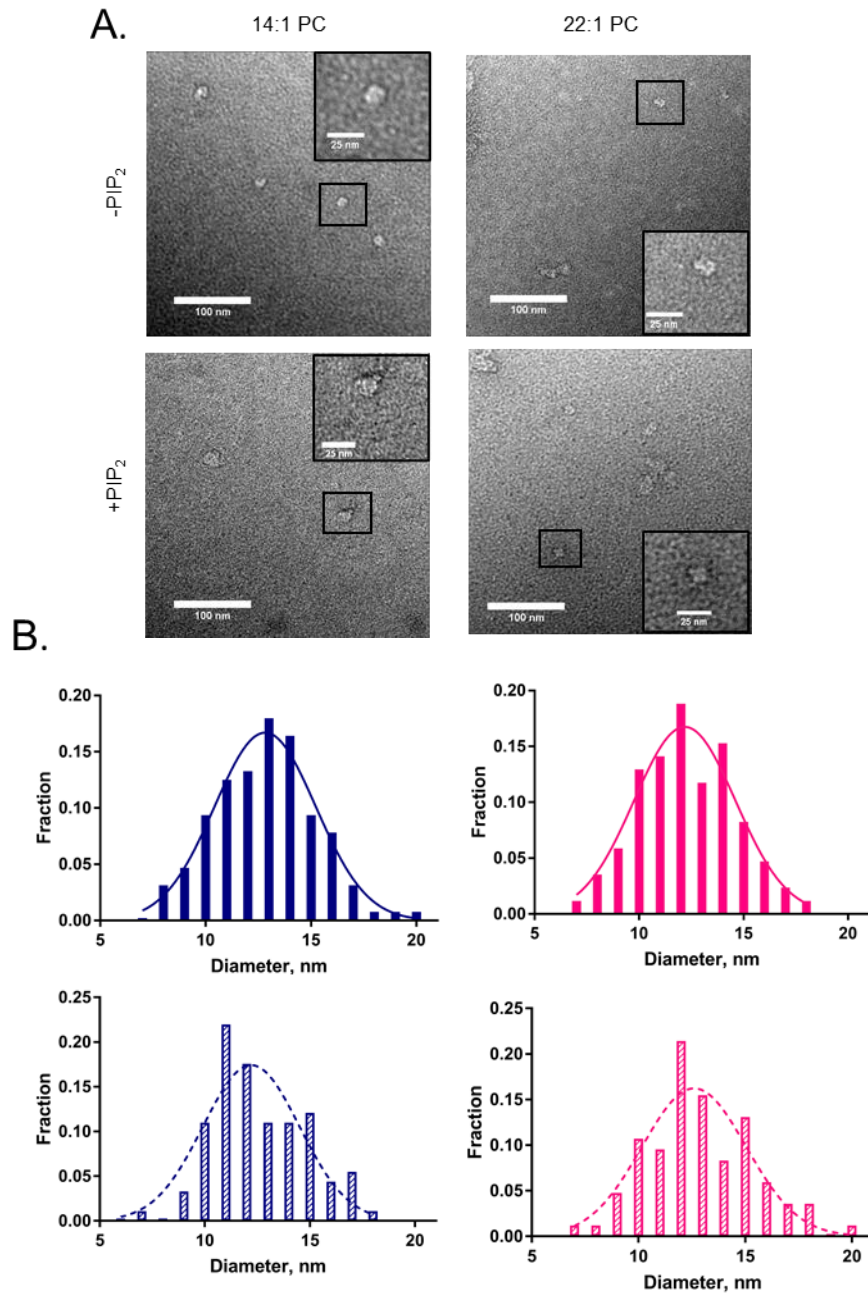
Figure 14. TEM of 14:1 PC and 22:1 PC SMALPS.

A. Representative TEM images of SMALPs comprised of 22:1 and 14:1 PC ± PIP_2. Scale bars in large images are 100 nm. Scale bars in insets are 25 nm. **B.** Histograms of SMALP diameters. Top: 22:1 PC (solid bars) and 22:1 PC + PIP_2 (cross hatch). Bottom: 14:1 PC (solid bars) and 14:1 PC + PIP_2 (cross hatch). Data are from 3-4 independent SMALP preparations for each lipid composition. 80-100+ SMALPs were measured for each lipid composition.
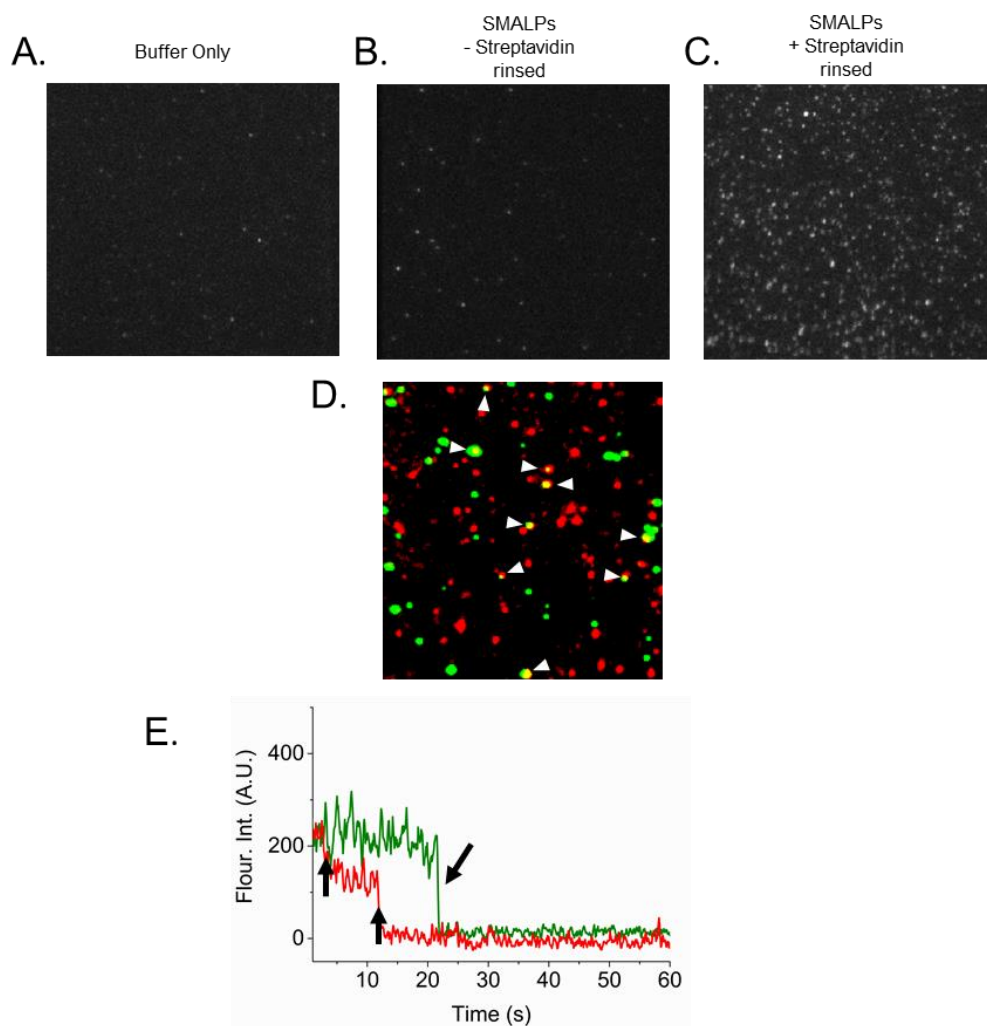
Figure 15. Controls for SMALP immobilization and composition.

A. Biotinylated slide with buffer only. **B.** A biotinylated slide without streptavidin was incubated for 10 min. with SMALPs containing 3% biotin-PE and TMJM Alexa488 and rinsed. Images show no immobilized SMALPs. **C.** A biotinylated slide was incubated with 0.2 mg/mL streptavidin for 10 min followed by incubation with SMALPs containing biotin-PE and TMJM Alexa488 then rinsed. Image shows immobilized SMALPs. **D.** Co-localization of SMALPs with PIP_2 Bodipy FL (left) and TMJM Cy5 (right) simultaneously excited. White arrows highlight SMALPs containing both PIP_2 and TMJM. **E.** Representative fluorescent trace from co-localization shown in D showing TMJM Cy5 (red) with two photobleaching steps and simultaneous fluorescence from PIP_2 Bodipy FL (green).

via a biotin-streptavidin linkage (Figure 13A, Figure 15A-C). Imaging was conducted using total internal reflection fluorescence (TIRF) microscopy. By analyzing the fluorescence of individual SMALPs over time, we can count individual fluorophore photobleaching events (Figure 13B) to determine the number of labeled TMJM peptides contained in a single SMALP. At a lipid to peptide ratio of 300:1 we found a substantial fraction of the peptide in SMALPs yielding two photobleaching steps Figure 13C). The majority of SMALPs contained one or two labeled TMJM peptides. Only a small fraction of SMALPs had 3 or more photobleaching steps (Figure 16). These results were robust as similar values were found for 2 bleaching steps in 22:1 PC and 14:1 PC (Figure 13C). Similar percentages of SMALPs containing one and two peptides were also observed at different lipid to peptide ratios (Figure 16). The single molecule results suggest that TMJM is in a similar monomer-dimer equilibrium in 14:1 PC and 22:1 PC.

Helical tilt alters environment of JM residues but not distance from the bilayer surface

We next investigated if JM-lipid interactions are different in the two conformations adopted by TMJM. We sought to understand if the change in helical tilt observed for TMJM in thin and thick bilayers altered the position of the JM residues. We used the tryptophan placed after the JM residues as a reporter (Figure 11A) and fluorescence experiments were performed in 14:1 PC and 22:1 PC 100 nm vesicles. We observed that the fluorescence intensity of the

74
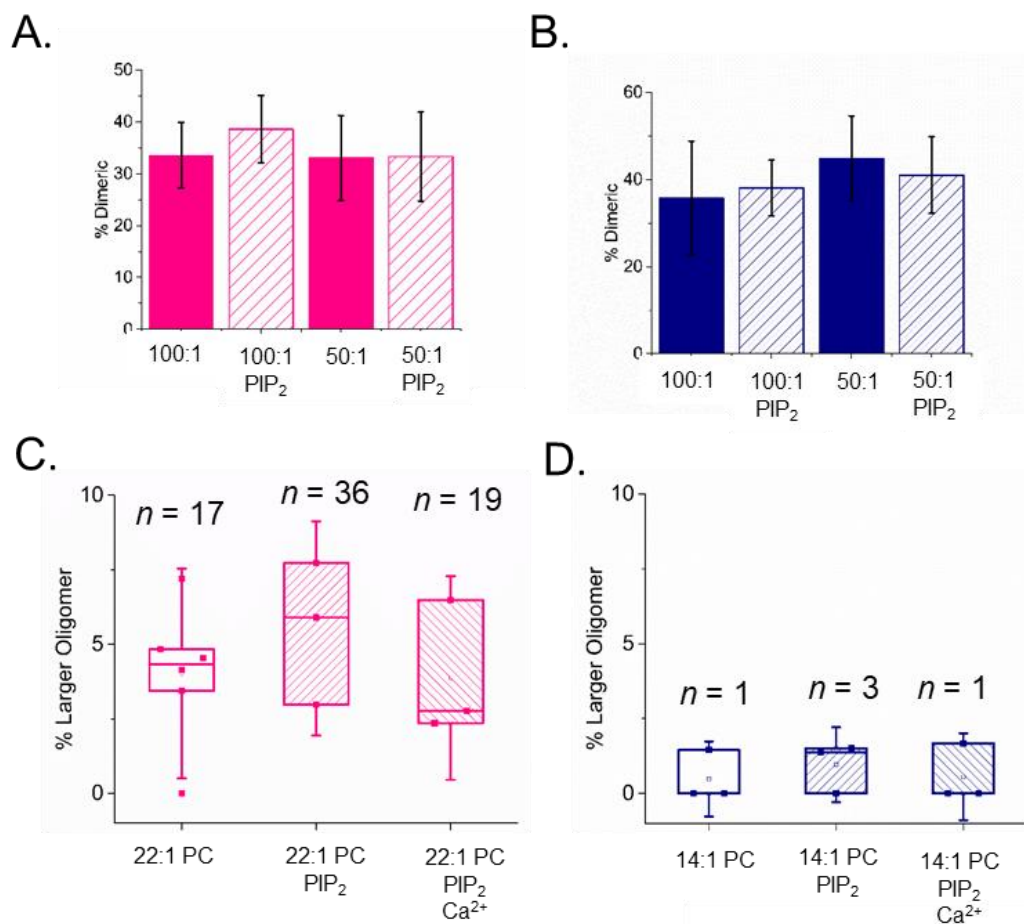
Figure 16. Percentages of dimeric TMJM at different concentrations and percentages of larger oligomers.

A. Percentage of dimeric peptide determined by SM-photobleaching at lipid to peptide ratios of 100:1 and 50:1 in 22:1 PC SMALPs with and without PIP_2. Bars are averages of 3 independent experiments ± S.D **B.** Percentage of dimeric peptide determined by SM-photobleaching at lipid to peptide ratios of 100:1 and 50:1 in 14:1 PC SMALPs with and without PIP_2. Bars are averages of 3 independent experiments ± S.D **C and D.** Percentage of peptide in larger oligomers in 22:1 PC and 14:1 PC SMALPs with and without 3% PIP_2 and 5 mM Ca^{2+} via SM-photobleaching experiments. Data are from 3-6 independent experiments. n = number of traces counted with 3 or more steps.

tryptophan was higher in 14:1 PC than 22:1 PC (Figure 17A) but the spectral maximum was similar (Figure 18). These data suggest a small change in the environment of the tryptophan that is not related to differences in membrane burial of the JM (189).

We next examined the association of the JM with the bilayer interface using the tryptophan as a FRET donor and a headgroup-labeled dansyl phosphatidylethanolamine (DNS-PE) as an acceptor. In both 14:1 PC and 22:1 PC in liposomes a decrease in donor fluorescence was observed upon the addition of 0.25 - 3% acceptor, indicating that FRET occurred in all conditions (Figure 19). By calculating the FRET efficiency (E) at 0.5% acceptor we were able to quantify that the FRET occurring in 22:1 PC and 14:1 PC was similar (Figure 17B). These data combined with the tryptophan fluorescence results (Figure 17A) led us to conclude that interhelical crossing angle does not greatly affect the association of the JM residues of TMJM with PC lipid bilayers.

PIP_2 drives changes in JM-headgroup distance only in thick membranes

To begin examining the effects that anionic lipids have on the coupling of TMD orientation and JM-lipid association, we repeated the OCD experiments in the presence of 3% PIP_2. We observed no large changes in helical tilt caused by the addition of PIP_2 in either thin or thick bilayers (Figure 20). Therefore, we conclude that the addition of anionic lipids does not perturb the hydrophobic matching driven changes in helical tilt observed in the original OCD experiments (Figure 11B).
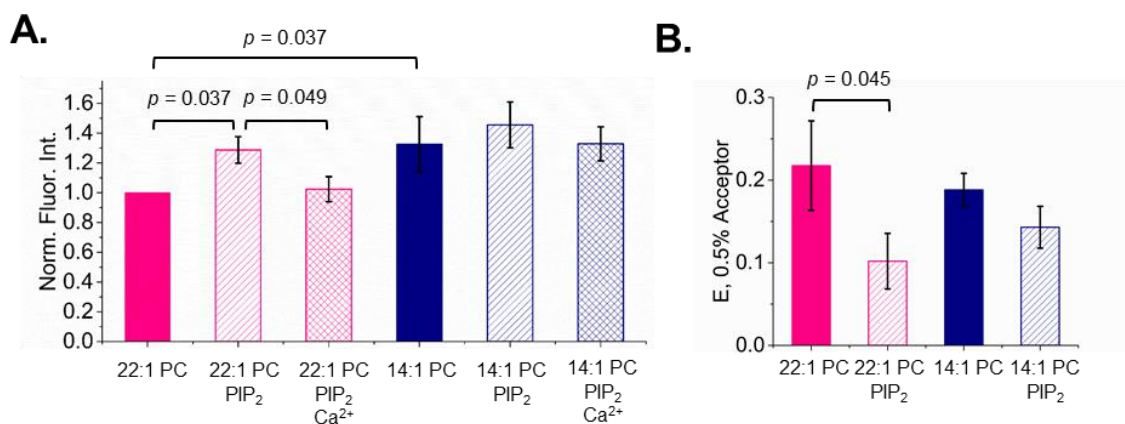
Figure 17. Bilayer thickness and PIP$_2$ alter Trp environment while headgroup distance is changed by PIP$_2$.

A. Normalized intensities of TMJM Trp in 22:1 PC and 14:1 PC liposomes in the presence and absence of PIP$_2$ and 5 mM Ca^{2+}. *p*-values were determined by Mann-Whitney U tests, bars are means ± S.D., *n* = 3 **B.** FRET efficiencies calculated from FRET experiments with TMJM (Trp, donor) in 14:1 PC and 22:1 PC liposomes in the presence and absence of 3% PIP$_2$ (3% DNS-PE, acceptor) in liposomes (bars are means ± S.D., *n* = 3). (*p*-value is from one-way ANOVA followed by Tukey post-hoc test).
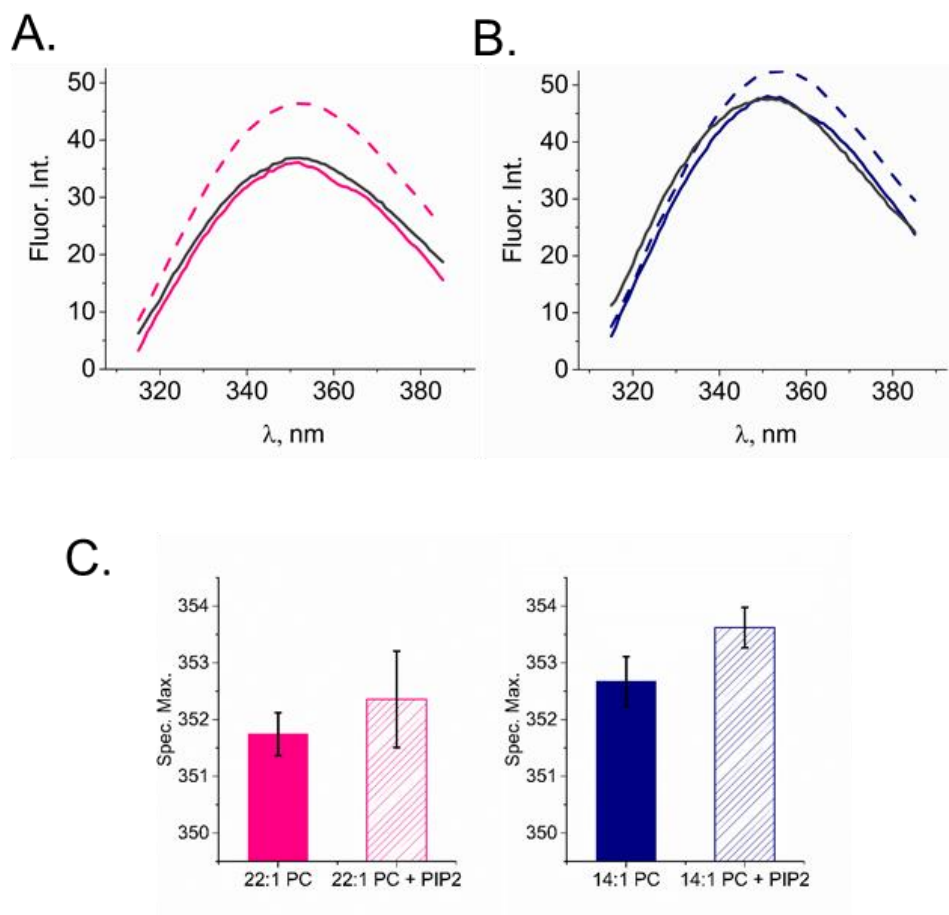
Figure 18. Tryptophan emission spectra and spectral maxima.

A. Trp emission spectra in 22:1 PC liposomes (solid fuchsia line), with 3% PIP$_2$ (dashed line) and 3% PIP$_2$ with Ca^{2+} (gray line) (curves are averages of 3 independent experiments). **B.** Trp emission spectra in 14:1 PC liposomes (solid navy line), with 3% PIP$_2$ (dashed line) and 3% PIP$_2$ with Ca^{2+} (gray line). Curves are averages of 3 independent experiments. **C.** Tryptophan fluorescence spectral max in 14:1 PC and 22:1 PC liposomes with and without 3% PIP$_2$. Bars are means ± S.D. from 3 independent experiments.
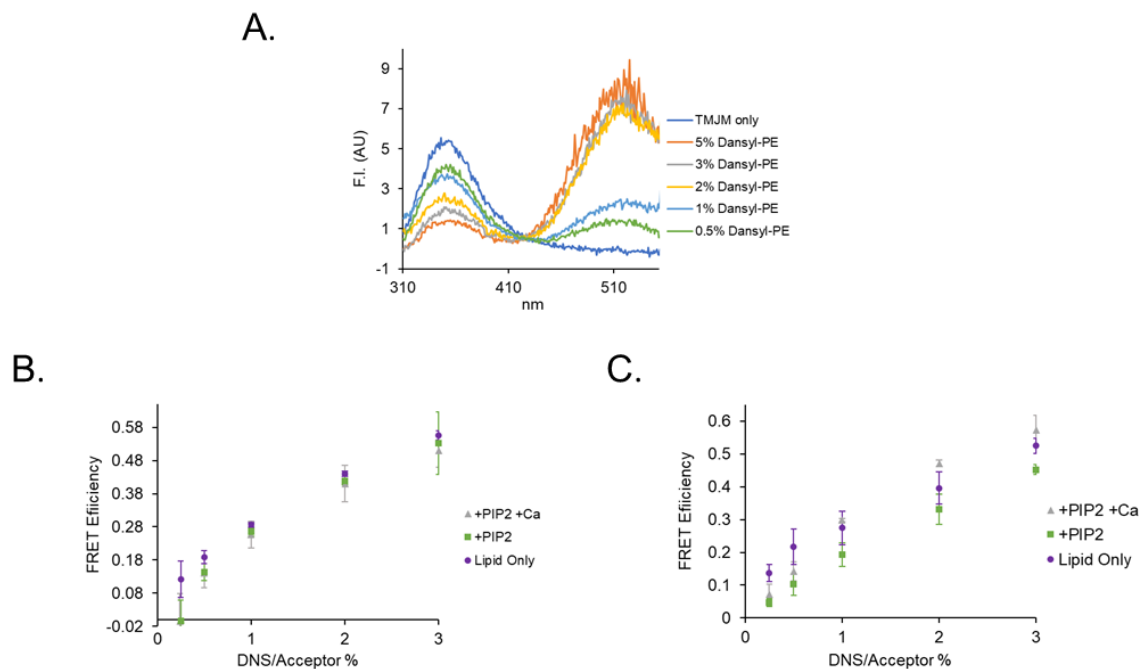
Figure 19. Trp DNS-PE FRET emission spectra and efficiencies.

A. Representative emission spectra of Trp and Dansyl showing saturating amounts of FRET at ~2% DNS-PE. **B.** FRET efficiencies of 1 µM TMJM in LUVs with 0-3% DNS-PE without PIP_2 or Ca^{2+} (purple), with 3% PIP_2 (green), and with 3% PIP_2 and 5 mM Ca^{2+} (grey) in 14:1 PC liposomes. **C.** FRET efficiencies of 1 µM TMJM in LUVs with 0-3% DNS-PE without PIP_2 or Ca^{2+} (purple), with 3% PIP_2 (green), and with 3% PIP_2 and 5 mM Ca^{2+} (grey) in 22:1 PC liposomes. Points are averages of 3 independent experiments ± S.D.
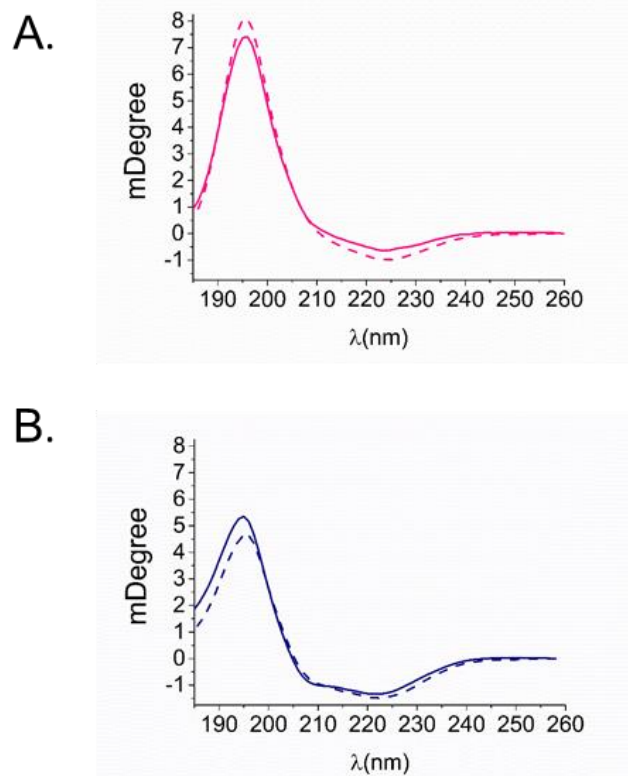
Figure 20. Helical tilt in thin and thick bilayers is preserved upon addition of PIP$_2$.

A. OCD spectra of TMJM in 22:1 PC with PIP$_2$ (dashed line) and without PIP$_2$ (solid line). Curves are averages of 3 independent experiments. **B.** OCD spectra of TMJM in 14:1 PC with PIP$_2$ (dashed line) and without PIP$_2$ (solid line). Curves are averages of 3 independent experiments.

We next determined if PIP$_2$ could cause changes in JM-membrane interactions. We performed both tryptophan fluorescence and FRET measurements. When examining tryptophan fluorescence, we added the divalent cation Ca^{2+} as a control to shield the negative charges on PIP$_2$. Saturating levels of Ca^{2+} were used in these experiments as determined by calcium influx assays (Figure 21). In 22:1 PC, we observed a statistically significant increase in tryptophan fluorescence in the presence of PIP$_2$ (Figure 17A). The observed intensity increase was reversed upon the addition of Ca^{2+} (Figure 17A). This reversal suggests that cationic JM residues are participating in an electrostatic interaction with the anionic PIP$_2$ headgroups, and that this interaction is placing the JM tryptophan into a different position. However, there were no significant fluorescence intensity changes in 14:1 PC in the presence of PIP$_2$, suggesting that in a more tilted TM configuration, the JM residues are less sensitive to the electrostatic interactions with PIP$_2$ (Figure 17A). There were no significant spectral maxima changes for either 14:1 PC or 22:1 PC upon addition of PIP$_2$ (Figure 18).

When we performed FRET experiments to determine the effect of PIP$_2$ on the JM region, we observed differences in FRET efficiency across a range of acceptor concentrations, as expected (Figure 19). Figure 17B shows that in thick bilayers the presence of PIP$_2$ decreased FRET by roughly half. This indicates that the distance between the JM tryptophan and the DNS-labeled lipid
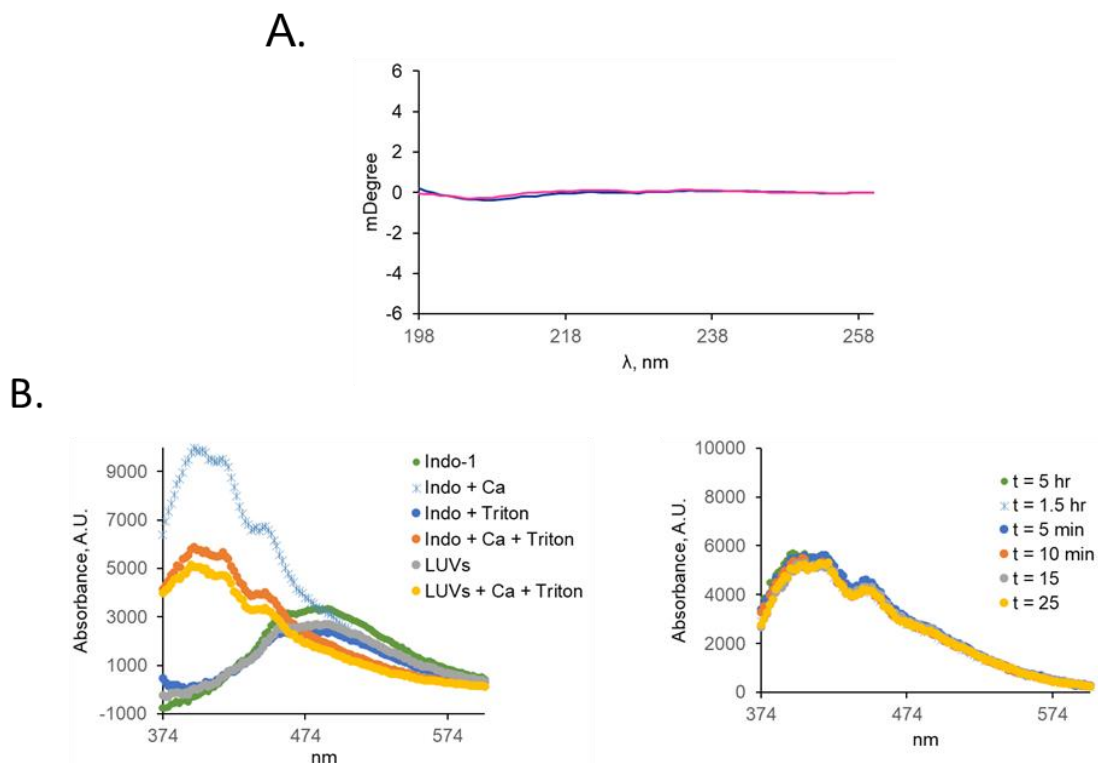
Figure 21. Peptide concentration and calcium influx controls.

A. Representative CD spectra of SDS washed tubes indicating comparable levels of peptide were recovered for 22:1 PC (fuchsia) and 14:1 PC (navy) liposomes in fluorescence experiments. **B. (right)** Blue shift of encapsulated Indo-1 dye spectral maximum is observed after addition of 5 mM Ca^{2+}. **(left)** Calcium influx assays showing 5 mM Ca^{2+} crosses the membrane in saturating amounts within 30 minutes.

headgroups is increased by PIP_2. This result agrees with the Trp fluorescence intensity changes caused by PIP_2 observed in thick bilayers (Figure 17A). By contrast, in thin bilayers, PIP_2 induced no significant changes in FRET efficiency Figure 17B).

PIP$_2$ drives increased oligomerization of TMJM only in thick membranes

Since changes in oligomerization accompany EphA2 signaling changes in cells (176, 190), we next determined if the interactions observed between the JM residues and PIP_2 influenced oligomerization of the peptide. Specifically, we used the single-molecule TIRF approach to examine the effect of PIP_2 on the self-assembly of TMJM, in thin and thick SMALPs. Transmission electron microscopy was conducted, which showed that PIP_2 did not alter SMALP size (Figure 14). Figure 22A shows that PIP_2 increased the amount of dimeric TMJM peptide in 22:1 PC. The increased dimerization was reversed in the presence of Ca^{2+}, indicating that this effect is due to an electrostatic interaction between the polybasic JM and the anionic PIP_2 headgroup. While Ca^{2+} can destabilize SMALPs, this effect is observed only at higher concentrations (>2 mM) than we employed (191). In contrast, PIP_2 did not affect dimerization in 14:1 PC (Figure 22B), nor do the counts for larger oligomers demonstrate a sensitivity to PIP_2 (Figure 16). Though they report on different aspects of the configuration of the peptide, these data agree with the tryptophan fluorescence and FRET data, which indicate that TMJM is sensitive to PIP_2 only in thick bilayers. Our data suggest that PIP_2 has a specific effect, which is limited to the conformation of
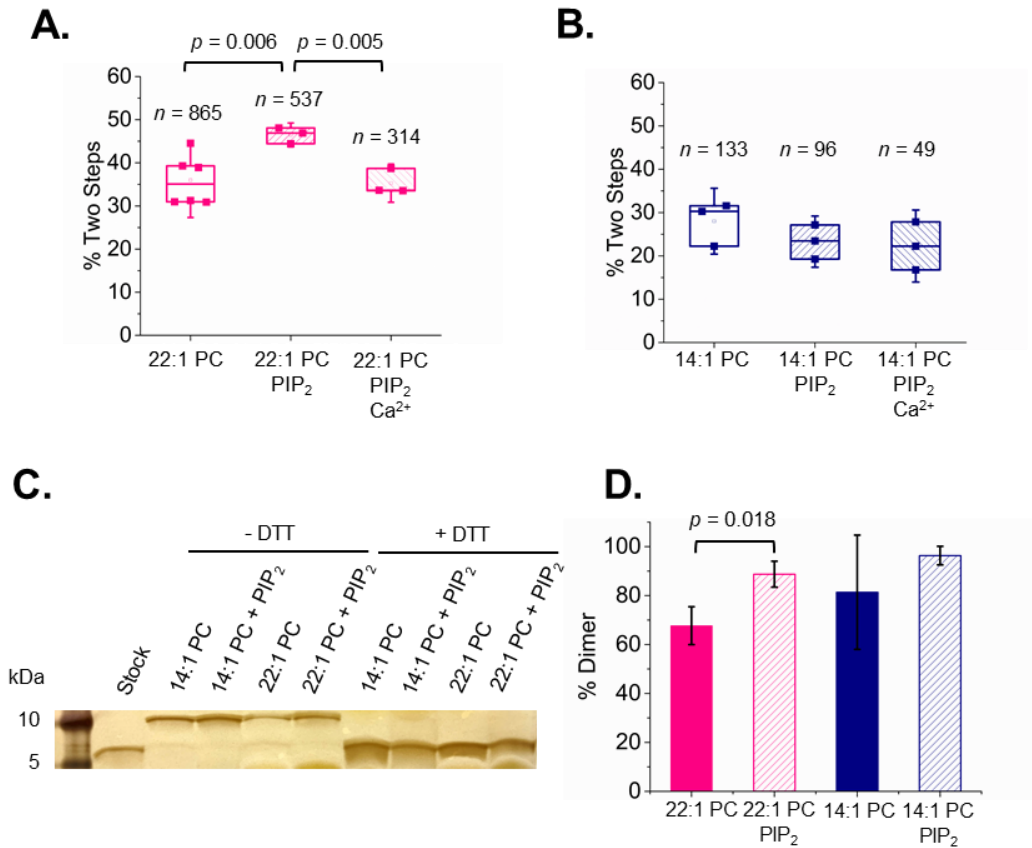
Figure 22. PIP₂ promotes self-assembly of TMJM in thick bilayers

A and B. Percentage of TMJM-Alexa488 peptide in two-step photobleaching traces in 22:1 PC and 14:1 SMALPs, respectively, determined by single-molecule studies. The effect of the presence of 3% PIP₂ and 1 mM Ca²⁺ are investigated. Data are from 3-6 independent experiments. *n* is number traces counted for each. *p*-values are from student's t-tests with significance determined after Benjamini-Hochberg procedure. **C.** Representative SDS-PAGE (full gel can be seen in Figure 23) of unlabeled TMJM in 14:1 PC and 22:1 PC liposomes in the presence and absence of 3% PIP₂. Monomer and disulfide-mediated dimers can be seen in non-reducing conditions. Addition of 5 mM DTT eliminates the disulfide-mediated dimer band. **D.** Quantification of 3 independent SDS-PAGE experiments as shown in C. Bands in each lane were quantified in ImageJ and percent of dimer was calculated. Bars are means ± S.D., *p*-value is from a student's t-test. All data are from experiments at a lipid to peptide ratio of 300:1, *n* = 3.
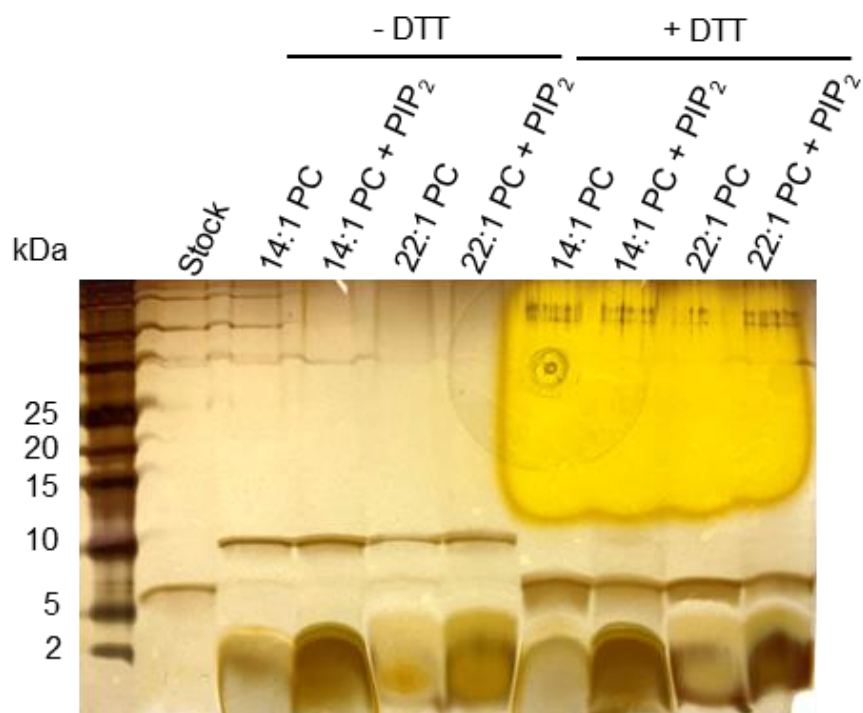
Figure 23. Representative SDS-PAGE of TMJM crosslinking.

Representative SDS PAGE gel of TMJM crosslinking as shown in Fig. 4C. Smears below 5 kDa are from lipids. Note: no smear is seen in first lane where no lipid was added. Yellow discoloration in upper-right portion of gel is from DTT.

TMJM present in thick bilayers. Further, this effect is likely due to JM-PIP$_2$ electrostatic interactions.

To further investigate the effects of JM interactions on the self-assembly of TMJM we performed SDS-PAGE experiments where dimerization was investigated by disulfide crosslinking. We reasoned that if PIP$_2$-dependent changes in self-assembly are promoted by lipid-JM interactions, this effect would be observable as differences in band sizes on a protein gel. Instead of measuring TMD-TMD interactions, as in the single-molecule experiments, we instead examined JM-JM interactions. To do this, TMJM containing a free Cys residue at the JM end was reconstituted in liposomes of 14:1 PC and 22:1 PC in the presence and absence of 3% PIP$_2$. The peptide stock remained monomeric in our basal conditions (Figure 22C, first lane). In the absence of a reducing agent, we observed two bands corresponding to monomer and disulfide-mediated dimer in all lipid conditions (Figure 22C). The relative percentage of monomer and dimer was measured for each lipid condition. We observed that in 22:1 PC + PIP$_2$ vesicles, the percentage of disulfide-mediated dimer was higher than in 22:1 PC alone (Figure 22D), in agreement with the single-molecule data in SMALPs. In 14:1 PC no effect of PIP$_2$ was observed.

PS alters JM environment but not dimerization in thick membranes

Given the effects of PIP$_2$ on TMJM, we wondered if phosphatidylserine (PS), an anionic lipid abundant at the plasma membrane, would also exert similar effects on the JM residues and dimerization of TMJM. The net charge of PS is -1,

while PIP$_2$ has on average a charge of -3 (192). To achieve a similar net charge in our model membranes, we used 22:1 PC with 10% PS (compared with 3% PIP$_2$). This value is similar to PS levels found in the plasma membrane of eukaryotic cells (193). We tested for changes in tryptophan fluorescence and oligomerization in 22:1 PC, where PIP$_2$-dependent changes were observed previously. As with the tryptophan fluorescence experiments, a significant increase in fluorescence intensity was observed in the presence of PS (Figure 24A). However, unlike the PIP$_2$ experiments, this increase was not fully reversed in the presence of saturating amounts of Ca^{2+}, suggesting differences in the effect of the two anionic lipids. Furthermore, single-molecule experiments showed that the presence of PS did not promote dimerization (Figure 24B). These data suggest that PS alters the environment of the JM residues like PIP$_2$, but without simultaneously driving significant changes in dimerization.

3.5 Discussion

We developed a reconstituted system that could stabilize the membrane region of the EphA2 receptor in two different configurations. OCD experiments performed in bilayers comprised of 14:1 PC indicated that the TMJM peptide adopted a highly tilted TM arrangement, as revealed by the presence of two well-resolved spectral minima at 208 and 224 nm (184–186). On the other hand, OCD results in the thicker 22:1 PC bilayers showed different features: the signal in the 200-230 nm range was less negative, and the 208 nm minimum was less
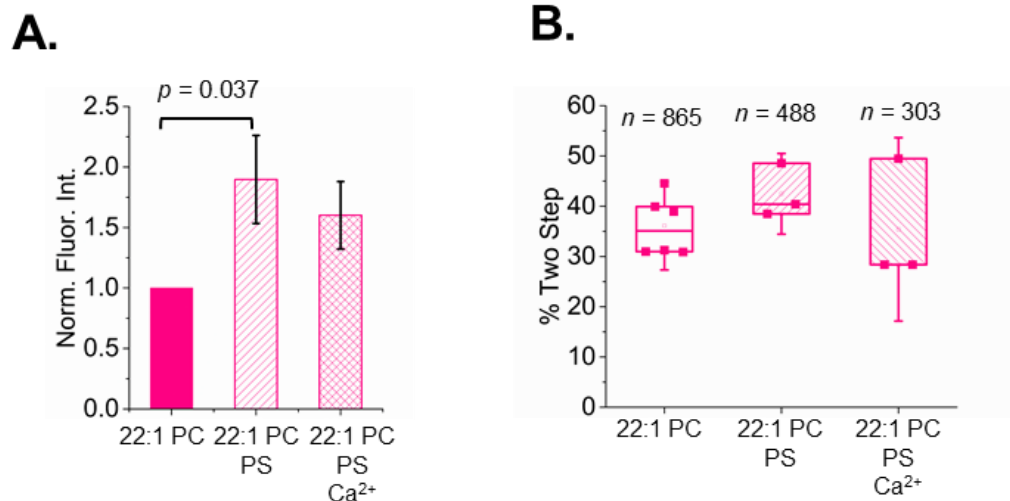
Figure 24. PS interactions with TMJM in thick bilayers

A. Normalized fluorescence intensities from emission spectra of TMJM in 22:1 PC liposomes with 10% POPS and 5 mM Ca^{2+}. Bars are means ± SD, n = 3. p-values were determined by Mann-Whitney U tests. **B.** Percentages of dimeric TMJM from SM-photobleaching experiments in 22:1 PC examining effects of 10% POPS and 1 mM Ca^{2+}. Data are from 3-6 independent experiments. n is number traces counted for each. No statistically significant differences were found.

pronounced, becoming a shoulder (Figure 11B). These differences clearly indicate that in thick bilayers the TMJM α-helix aligns close to perpendicular to the bilayer plane. It is theoretically possible to use OCD to calculate specific helical tilt angles (49), but we could not accurately carry out this approximation due to uncertainties in the homogeneities of the supported bilayers employed in OCD. However, there is an intriguing qualitative agreement between our data and the two TM conformations reported for EphA2 (22, 137). The ligand-dependent dimer crossed the membrane in a highly tilted state (45°), while the ligand-independent dimer has a small crossing angle (15°) (Figure 11B). Based on this similarity, we propose that the two conformations found in our data might correspond to the membrane structure EphA2 adopts in the two different activation states: in 22:1 PC dimerization would occur with almost parallel helices, as expected for the ligand-independent dimer. In 14:1 PC a high-crossing angle dimer would correspond to the conformation induced after ligand (e.g., ephrinA1) binding. Our data indicate that this can be accomplished using thin and thick bilayers by taking advantage of the strong propensity of the TMD to avoid hydrophobic mismatch (183).

To ensure that the TMJM engages in biologically relevant dimerization we employed two complementary methods. After finding artifacts in FRET experiments performed in liposomes, we resorted to develop a new single molecule approach that uses SMALPs, which have been shown to maintain native membrane structures (Figure 13) (187, 188). We also performed a

crosslinking assay in liposomes of the same lipid composition as the SMALPs. While this method does not measure dimerization *per se*, it is expected to report on a related event, the proximity of the JM cysteines. With these limitations in mind, it is likely that this method does not give an exact measurement of the amount of dimer in equilibrium, but an adequate estimation to make comparisons between different lipid environments. Not surprisingly the two methods yield different levels of dimerization of TMJM. However, they agree in reporting comparable levels of the dimer found in 14:1 PC and 22:1 PC environments (compare Figure 13C to Figure 22C-D). We conclude from the dimerization and OCD data that our thin and thick bilayer systems promote two different helical orientations of TMJM and that in both cases the peptide can from a dimer.

The JM segment of EphA2 is functionally important, as it contains the residues Y588 and Y594, which are phosphorylated by the kinase domain of EphA2. This event triggers the release of the receptor from the inactive, autoinhibited state (119). Hedger *et al.* examined the interaction of basic JM residues of 58 RTKs with anionic lipid headgroups via MD studies (159). They concluded that JM residues closest to the TM have significant contacts with PIP_2. Specifically, for EphA2, their simulations predicted that the HRRRK region of the JM contributed the most to contacts with PIP_2. Similar observations have been made in simulations of the JM and kinase domain of EphA2 in PIP_2 containing bilayers (194). However, these JM-PIP_2 interactions have never been

experimentally demonstrated. Based on this observation we included the HRRRK residues in the TMJM peptide.

Using the tryptophan near the C-terminus as a sensor we were able assess the JM environment in different lipid environments. Typically, burial of a tryptophan in a membrane results in a blue shift of the spectral maximin and a concurrent increase in fluorescence intensity (189). The change in bilayer thickness had a significant effect on the tryptophan fluorescence intensity but no accompanying shift in spectral maximum was observed. This uncoupling of intensity and spectral maximum could be due to adjacent residues that can quench tryptophan fluorescence. Specifically, the neighboring cysteine residue is known to engage in excited-state electron transfer with tryptophans (195). Further, it has been shown that tryptophan fluorescence spectra are sensitive to nearby charged residues (196). This led us to conclude that the local environment of the tryptophan is different in thin and thick bilayers, not because of changes in environmental polarity but more likely due to changes in relative orientation or proximity to the neighboring residues. When PIP_2 was added in thick bilayers, the tryptophan fluorescence increased significantly and was reversed upon the addition of Ca^{2+}. This observation indicates that an electrostatic interaction occurs between the polybasic JM residues and the anionic PIP_2 headgroups. We did not observe fluorescence changes with PIP_2 in thin bilayers, indicating that the peptide is not sensitive to the charged lipids in this alternate conformation.

Complementary FRET experiments revealed that PIP$_2$ altered the distance of JM residues to the DNS-PE headgroups. A significant decrease in FRET in the presence of PIP$_2$ was only observed in thick bilayers. To explain the increase in Trp fluorescence intensity and the decrease in observed FRET in 22:1 PC vesicles containing PIP$_2$ we have developed two possible explanations (Figure 25). First, it is possible that in the presence of PIP$_2$ the JM gets more buried into the core of the membrane vertically with respect to the plane of the bilayer moving the Trp away from the headgroups. Alternatively, PIP$_2$ may be clustering around the JM residues as their charges interact, and this crowding pushes the DNS-PE headgroups out away from the tryptophan laterally in the plane of the bilayer.

In single molecule experiments, PIP$_2$ bilayers promoted TMJM dimerization in thick bilayers, presumably *via* changes in TMD-TMD interactions. To assess self-assembly *via* JM-JM interactions we conducted disulfide crosslinking experiments (Figure 22C). SDS PAGE again showed that in thick bilayers PIP$_2$ promoted self-assembly. These results agree with the single-molecule SMALP data and suggest that the increased TMD-TMD dimerization is facilitated by PIP$_2$ through JM interactions. In thin bilayers, no PIP$_2$ dependent changes in disulfide-mediated dimerization was observed, also in agreement with the single-molecule data.
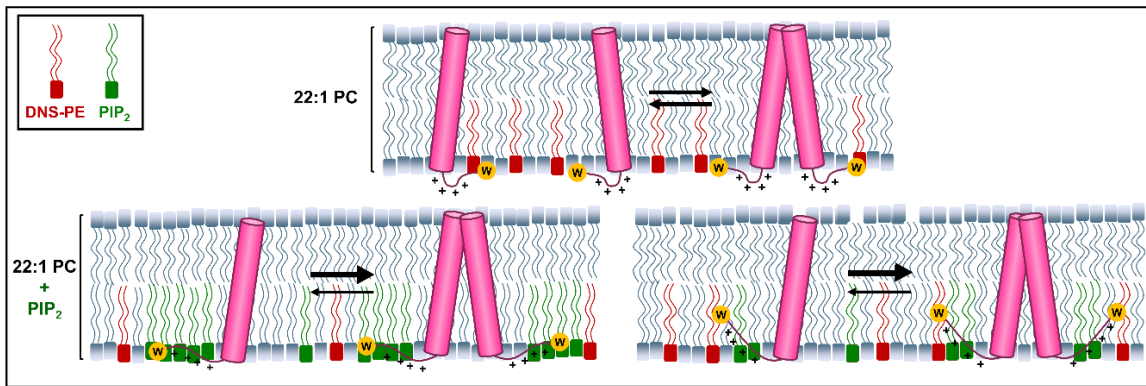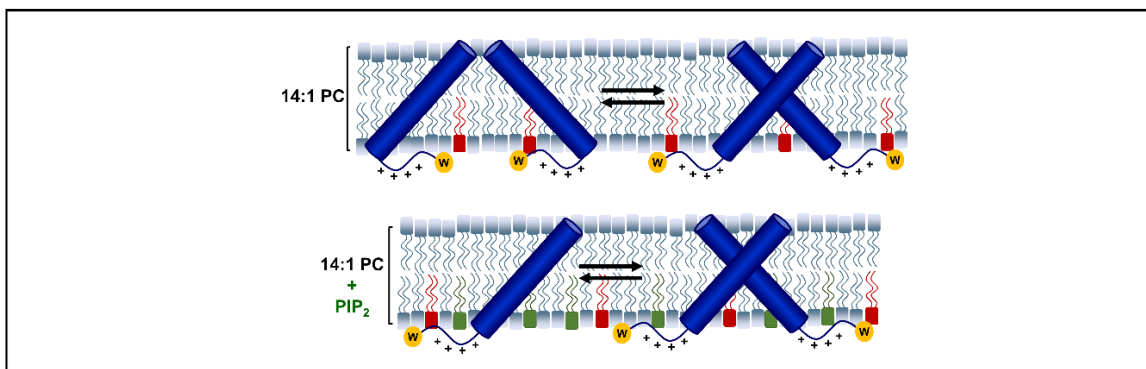
Figure 25. Model of TMJM in thin and thick bilayers.

(top) In the ligand-independent signaling configuration TMJM exists in a monomer-dimer equilibrium in the absence of PIP_2. Charge-charge repulsion of the JMs must be overcome for dimerization. In the presence of PIP_2 the JM-lipid association changes by either clustering of PIP_2 around the JM or burial of the JM. This shields the positive charges promoting dimerization. **(bottom)** In the ligand-independent signaling configuration TMJM exists as a monomer and dimer. Due to the tilt of the TM, charge repulsion of the JMs is not as large as in the ligand-independent state. Neither JM environment nor dimerization is altered by PIP_2.

93

Our data indicates that there is coupling between the TMD orientation and JM association with the bilayer, resulting from JM repulsion. In thick bilayers the TMD is less tilted, placing the JM close to each other in the dimer. The resulting electrostatic repulsion prevents further dimerization. The presence of PIP_2 attenuates these repulsive interactions to promote self-assembly via the TMDs. In thin bilayers the TMD adopts a more tilted orientation and in this configuration the JM is not sensitive to the presence of PIP_2, as the JM are too far away to repel each other in the dimer.

Based on previous work (22, 137) and our data we propose a model where the TMD and JM can be coupled. In the ligand-independent state EphA2 dimerization is facilitated by the heptad repeat motif resulting in a more upright orientation. In this configuration, the JM residues are tightly associated with the inner leaflet of the cell membrane via electrostatic interactions with PIP_2 (Figure 25, top). Without PIP_2, EphA2 dimerization would be less favorable due to charge-charge repulsion of the JMs. We propose that this is overcome by either clustering of PIP_2 around the JMs or burial of the JM due to PIP_2 interactions that shield the charged JMs from each other. In the ligand dependent states, the TMD dimers would rotate to the glycine zipper dimerization interface and open to create a larger interhelical crossing angle. With the larger interhelical crossing angle of the glycine zipper dimer, charge-charge repulsion due to the JMs is decreased and thus PIP_2 does not promote dimerization. In this conformation,

PIP$_2$ is no longer able to exert the same effects on the JM residues or oligomerization of EphA2 (Figure 25).

Tryptophan fluorescence data with PS suggest that, as with PIP$_2$, electrostatic interactions are enough to alter the environment of the JM region. However, unlike PIP$_2$, the PS interaction is not fully reversed upon addition of saturating amounts of Ca^{2+}. This could be due to differences in binding sites and stoichiometry of the two lipids with Ca^{2+} ions (197, 198). Interestingly, PS did not promote dimerization as PIP$_2$ did, and the tryptophan fluorescence changes were larger. This leads us to conclude that JM interactions with PS do alter the environment of the JM but without promoting dimerization. In this case, the charge density of PS may not be large enough to overcome the charge-charge repulsion caused by the JM polybasic stretch whereas the larger charge density of PIP$_2$ is. It has been reported that PS engages in contacts with RTK JM residues to a lesser degree than PIP$_2$, which may explain why in our experiments we see an effect of PS on JM environments but not on oligomerization (159).

Our data suggest that PIP$_2$ might play a direct role in modulating ligand-independent EphA2 signaling by stabilizing ligand-independent dimers and holding the phosphorylatable JM tyrosine residues at the plasma membrane. PIP$_2$-JM interactions have been demonstrated experimentally for several receptors including the epidermal growth factor receptor (EGFR), fibroblast growth factor receptor (FGFG), and tropomyosin receptor kinase A (TrkA) (21, 160, 199, 200). It is believed that these electrostatic interactions serve to

sequester phosphorylatable JM residues, rendering them inaccessible to the kinase domain, prior to activation of the receptor (21, 201). It is likely that this effect is paired with the kinase domains also binding with the membrane, which has been shown via MD for EphA2, and experimentally for EGFR (201, 202).

PIP_2 may thus play a role in modulating ligand-independent signaling levels. One study proposed that the tumorigenic signaling that occurs in the absence of ligand is caused primarily by monomeric EphA2 (176). By promoting dimerization of the unliganded state, PIP_2 could be reducing this signaling as well. Dimerization via PIP_2 in the unliganded state would be modulated by the SAM domains which are known to inhibit oligomerization (203). We speculate that when the ligand-independent dimer binds to an ephrin ligand, EphA2 undergoes rearrangements including rotation and opening of the TMD crossing angle that accompanies the release of the JM residues from PIP_2. Dimerization via the glycine zipper would then no longer be promoted by PIP_2 but by interactions between other parts of the full-length protein which are known to oligomerize such as the cysteine rich domains and the ligand binding domains which are known to interact through two different interfaces upon ligand binding (56, 190, 204). The glycine zipper TMD dimer may also be further stabilized by interactions with other proteins which may contribute to formation of large signaling clusters. For example, it is believed that interactions between SAM domains and dimers of SHIP2 may form large linear arrays (205, 206).

These findings provide new insights that suggest that PIP_2 and maybe other phosphorylated inositols could directly act on EphA2, causing Akt-independent modulation of the receptor. We are currently working to test the hypothesis that the lipid environment specifically regulates full-length EphA2 in cells.

Chapter IV. The effect of pHLIP on lipid diffusion in supported lipid bilayers

4.1 Abstract

In order to design effective membrane targeting peptides, it is useful to understand how these peptides interact with membrane lipids. Using pHLIP as a model for pH-responsive membrane-targeting peptides, we sought to understand the effects pHLIP may have on lipid dynamics. Prior data suggested that pHLIP may have an effect on lipid viscosity and therefore lipid diffusion. Here we developed a method of measure lipid diffusion via fluorescence recovery after photobleaching. A method of making unilamellar supported lipid bilayers was created and a partially automated data analysis pipeline was written using Python and Mathematica coding languages to extract diffusion coefficients. We applied this to investigating the effect of pHLIP on lipid diffusion at different pH values. We found that pH had no effect on lipid diffusion alone while our data suggest that pHLIP may have some effects on lipid diffusion.

4.2 Introduction

Lipids were once thought to be a passive support component of cell membranes. More recently, through various studies, it has become clear that lipids play an active role in regulating membrane and membrane protein functions (207). Specifically, membrane proteins are directly affected by membrane curvature and thickness (208, 209). Bilayer thickness is not static and fluctuates around an average. Interestingly, this dynamic thickening and thinning occurs at timescales to protein conformational dynamics (210, 211). It is

99

interesting therefore to probe the interplay between and protein and membrane dynamics.

The pH low insertion peptide (pHLIP) is a well characterized pH responsive transmembrane peptide. It is being studied for clinical applications since pHLIP is soluble in aqueous solution as a random coil (state I), readily sticks to membranes at neutral pH (state II) and inserts at low pH as an α helix (state III) (Figure 2) (29, 33). As described in detail in Chapter 1, these characteristics make pHLIP appealing for use as a drug delivery vehicle or for targeting cells in environments with lower than normal physiological pH, one hallmark of the tumor environment (31).

To better enable the application of pHLIP, and other pH responsive peptides, as a therapeutic, it is important to fully understand the interplay between the dynamics of the peptide and its lipid environment. To better understand the affects pHLIP has on lipid dynamics a variety of biophysical approaches have been applied. Neutron spin echo experiments conducted by our lab indicate changes in membrane thickness fluctuation dynamics upon the addition of pHLIP at pH 8 and again at pH 4. At pH 8 (state II) thickness fluctuations appear to happen at a higher rate than controls while the rate slows compared to controls at pH 4 (state III) (data not shown). Recent studies have explored thickness dynamics and membrane viscoelastic properties (212, 213). To investigate potential changes in viscosity associated with the presence of pHLIP in state II and state III, we wanted to use fluorescence recovery after

photobleaching (FRAP) in supported lipid bilayers (SLBs) to measure lipid diffusion.

FRAP is used to monitor the two-dimensional diffusion of a population of fluorescently labeled molecules by bleaching a defined region (**Figure 26**B) then monitoring as bleached molecules diffuse out of the region and unbleached molecules diffuse into the bleached region (**Figure 26**C). Passive diffusion replenishes the fluorescence intensity to the region which was bleached. Fluorescence data from the bleached region can be used to measure the mean squared displacement per unit time (μm^2/sec, for example) of the labeled molecule. The fraction of fluorescent molecules in the bleached region that are mobile (mobile fraction) can also be determined. FRAP can be conducted with fluorescently labeled proteins, lipid, and other molecules and most confocal microscopes are equipped to perform this technique.

A simple way to extract quantified data from FRAP is to determine the time it takes for half of the initial fluorescence to recover or recovery half-time usually represented as $\tau_{1/2}$. This metric provides a simple means of comparing rates of diffusion and is easily acquired from FRAP data. However, making comparisons of $\tau_{1/2}$ is only appropriate for data collected using identical bleaching parameters. $\tau_{1/2}$ is dependent on the bleaching radius, bleaching protocol and the size and environment of the diffusing molecule. A more robust and measure is the diffusion coefficient, D (214, 215). Early work by Axlerod *et al.*, 1976 and
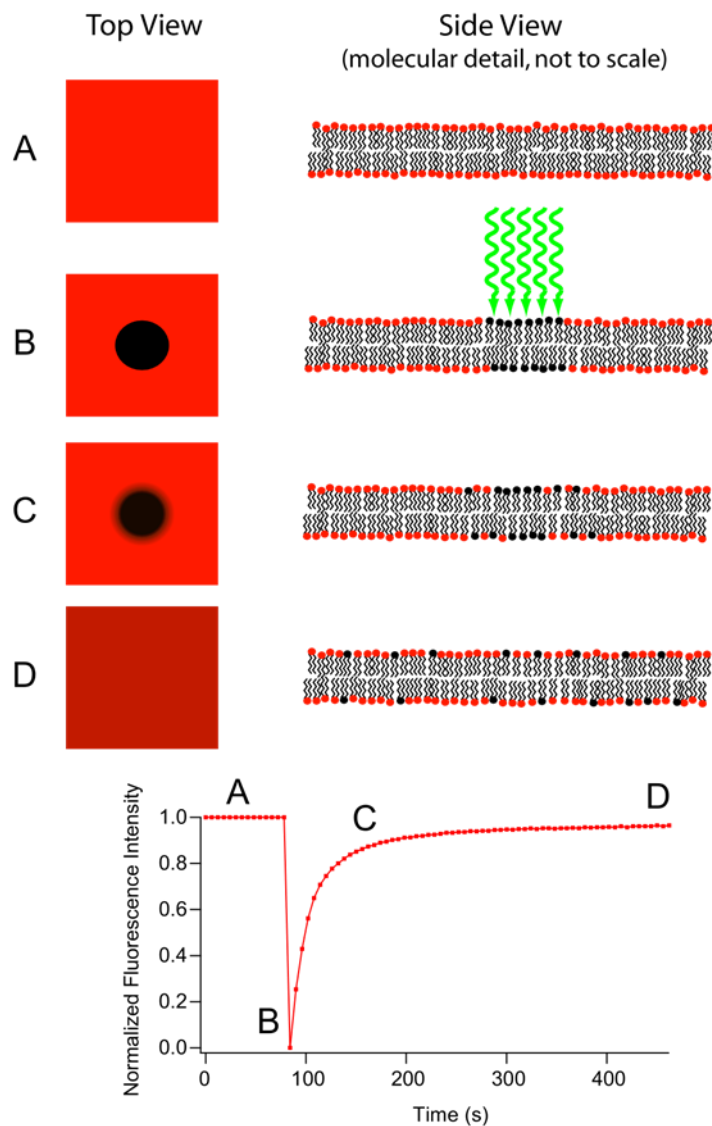
Figure 26. Theoretical FRAP images and recovery curve.

A. A lipid bilayer containing fluorescently labeled lipids. (MDougM, *Principle of FRAP*, 2008, commons.wikimedia.org/wiki/File:Frap_diagram.svg) **B**. A high intensity laser is used to beach a selected ROI. **C.** Passive lipid diffusion results in bleached lipids moving out of the ROI area unbleached lipids moving into the ROI. **D.** Diffusion eventually restores uniform fluorescence to the imaged area.

Soumpasis, 1983 produced the first mathematical models for fitting FRAP data to extract diffusion coefficients (214, 215). For example, the Soumpasis equation:

(1)
$$D = 0.224 \, \frac{r_n^2}{\tau_{1/2}}$$

Where D is the rate of diffusion, r_n is the nominal radius of the bleached spot, and $\tau_{1/2}$ is the half time of recovery. However, these early models assume that bleaching is instantaneous, and no diffusion occurs during this process. Due to the scanning times of confocal microscope diffusion does occur during bleaching and must be accounted for to accurately calculate D. To account for this, Kang *et al.* recently published their simplified FRAP equation for circularly bleached regions from confocal microscopes:

(2)
$$D_{CONFOCAL} = \frac{r_e^2 + r_n^2}{8\tau_{1/2}}$$

Where r_e is the effective bleaching radius of the postbleach spot profile.

Here we establish a protocol for producing uniform SLBs with which to conduct FRAP experiments via confocal microscopy. We apply a version on equation 2 to calculate diffusion coefficients. We then use this method to investigate if pHLIP in state II and state III effects the rate of lipid diffusion.

4.3 Methods

Glass Microscope Slide Cleaning:

A slide cleaning protocol adapted from Lin *et al.* was followed (216). Quartz microscope slides were boiled in 1% Contrad detergent for 20 minutes. Slides were then sonicated for 30 minutes in a hot water bath sonicator. Slides

were then briefly rinsed with MilliQ water to remove detergent. Slides were then soaked in piranha solution (75% sulfuric acid, 25% hydrogen peroxide) for 3 minutes. Slides were then thoroughly rinsed with MilliQ water. Slides were dried under a stream of argon gas.

Lipid Preparation and Vesicle Fusion

Lipid preparation and vesicle fusion protocols were adapted from published protocols (216, 217). The correct volumes of lipid stocks for a final concentration of 1.2 mg/mL in 400 ul (99% 1,2-dioleoyl-sn-glycero-3-phosphocholine (DOPC) (Avanti Polar Lipids, Alabaster Al) + 1% (1,2-dioleoyl-sn-glycero-3-phosphoethanolamine-N-(7-nitro-2-1,3-benzoxadiazol-4-yl)) (Avanti Polar Lipids, Alabaster Al) (NBD-PE)), were dried under inert gas followed by desiccation for 2-16 hours. Lipids were then resuspended in 200 μl MilliQ water then extruded 15 times through a 100 nm pore size filter. Vesicles were then diluted 2-fold in 20 mM sodium phosphate pH 7.4 + 300 mM NaCl for a final concentration of 10 mM sodium phosphate pH 7.4 + 150 mM NaCl. Final lipid concentration was 1.2 mg/mL

On a clean, dried slide, a 0.5 mm deep silicone isolator (Grace Bio-labs #664504) was placed. To the well the extruded lipid was added then covered and protected from light for 1 hour. Slide wells were then rinsed with 10 mM sodium phosphate pH 7.4 + 150 mM NaCl buffer 6-10 times.

FRAP

FRAP was performed on the SLB at neutral pH with a Leica SP8 laser scanning confocal using a 40x/1.30 HC PL APO CS2 oil immersion objective using an argon laser at 488 nm. The FRAP protocol was as follows with a scan speed of 1800 lines per second and averaging two lines: 10 pre-bleach images were taken using 0.5% laser power then a 4 μm^2 ROI was bleached for two frames (approximately 1.15 sec) at 100% laser power using the zoom-in function. Recovery was observed for 130 frames (about 75 sec). A total of 8 FRAP series were performed. pHLIP was then added to the SLB (150:1 lipid to peptide) in fusion buffer and incubated for 1 hour at room temperature. The FRAP procedure was repeated 8 times on the bilayer with pHLIP in neutral pH (state II). Finally, the buffer containing pHLIP was removed and replaces with 10 mM sodium acetate + 150 mM NaCl pH 4 to drive membrane insertion of pHLIP (state III). FRAP was repeated as described above.

Analysis

Pre-bleach and post-bleach intensities for the bleaching ROI and a background ROI were exported from LASX software. A python script (Appendix A) was written to copy these intensities from two separate files for each movie (a total of 48 files per experiment) into one excel file, set the time of bleaching to t = 0, and normalize the bleached ROI data to the background ROI data. This normalization of recovery data was performed to correct for total photobleaching observed while imaging.

The effective radii of photobleaching were determined by measuring fluorescence intensity across the bleached field using ImageJ. The intensities across this region were normalized to pre-bleached intensities across the same region. This was done for averaged data for each of the three treatment groups and fit to the following equation (Appendix C) to determine effective radius (r_e) (218):

$$(3) \qquad F_{postbleach}(x) = 1 - K \exp\left(-\frac{x^2}{r_e^2}\right)$$

Where F is the postbleach intensity, K is the bleaching depth (max intensity – min intensity across the bleached field) and x is the length of the line used to measure intensity across the bleached field.

The recovery data were then read into a Wolfram Mathematica notebook (Appendix B) and fit to the following equation modified from Kang *et al.*, 2012:

$$(4) \qquad F(t) = F_i\left\{1 - \frac{K}{1+\gamma^2+2t/D}\right\}M_f + (1 - M_f)F_0$$

Where $\gamma = \frac{r_n}{r_e}$, F_i is the prebleach intensity, F_0 is the postbleach intensity, K is the bleaching depth, M_f is the fraction of fluorescent molecules that are mobile, and t is the postbleach time. From the fittings, diffusion coefficients, (D in μm^2/sec), and mobile fractions (M_f) were determined for each FRAP movie and averaged across each treatment condition.

4.4 Results

Establishing a FRAP protocol for determination of diffusion coefficients

We were motivated to use FRAP on SLBs to investigate the possible effects of pHLIP on lipid diffusion. At the time, there was no working protocol in our lab for conducting these experiments. I sought out to hone a method for making supported lipid bilayers. We first attempted to make POPC SLBs on piranha slides using a simple vesicle fusion method. These early attempts resulted in patchy bilayers with many defects. This was determined by attempting FRAP experiments in which the bilayers containing a fluorescently labeled lipid would be photobleached but no recovery would occur and therefore no lipid diffusion in or out of the bleached area.

After several iterations of slide cleaning protocols and changing lipid composition, the method described above resulted in uniform SLBs which when photobleached recovered as expected (Figure 27A). FRAP experiments were carried out on a laser scanning confocal. Images of an area of bilayer were accumulated and then a region of interest (ROI) was bleached followed by further imaging until the fluorescence intensity of the bleached area recovered completely. This process resulted in two separate video files (pre-bleach and post-bleach) for each bleaching event. To plot and fit these data, the pre-bleach and post-bleach intensity of the ROI needed to be exported from the proprietary software format into .csv files then combined into a single plot. Further, to
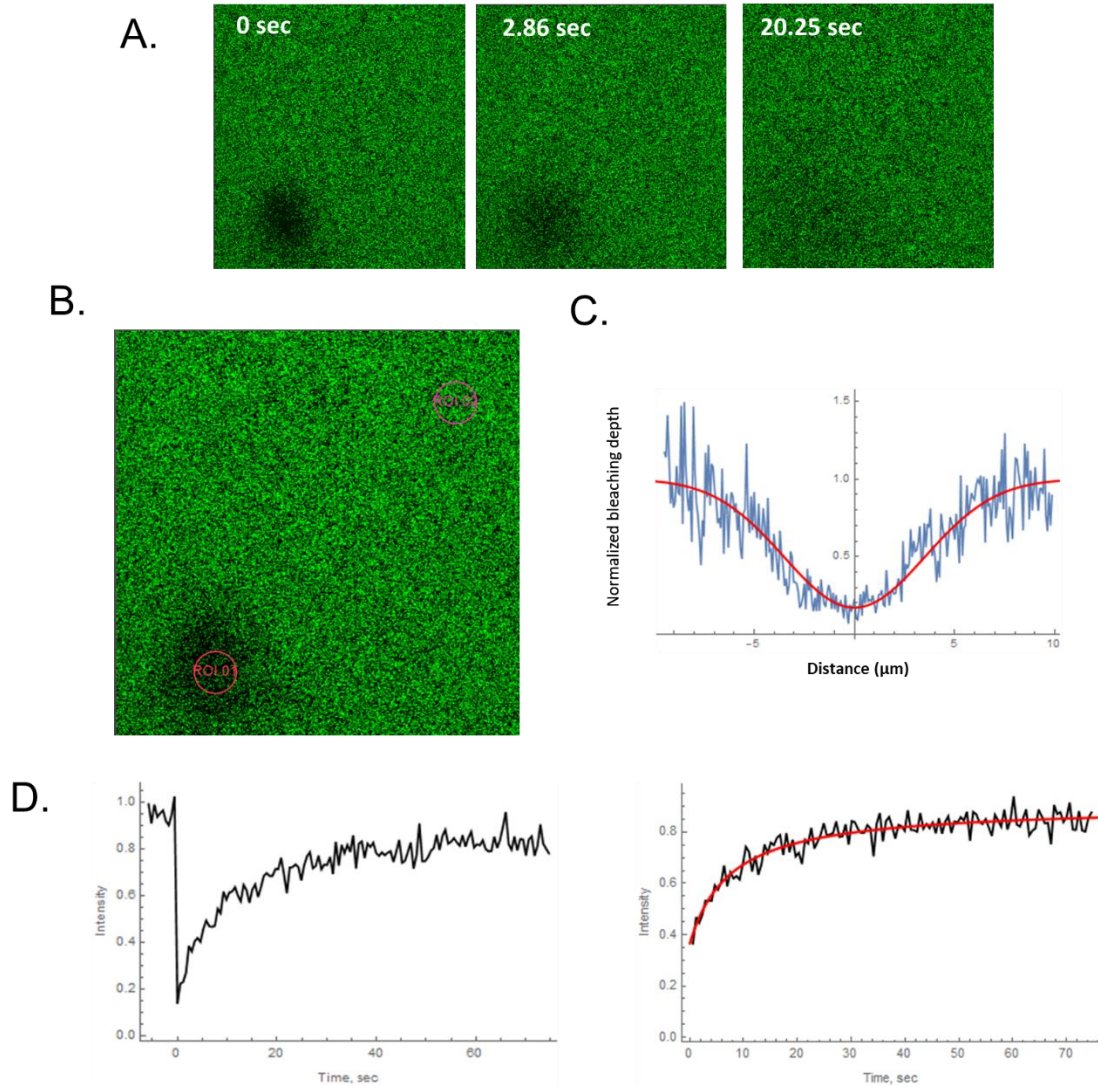
Figure 27. Representative FRAP images, r$_e$ measurement, and recovery curve fitting.

A. Representative stills from a FRAP movie showing the post-bleach ROI recovering fluorescence over time **B.** Representative image showing difference between r_n and r_e (bottom left). Example of ROI used to track background photobleaching also shown (top right). **C.** Representative fitting (red line) obtained for determination of r_e from fluorescence measurements across the bleached area (blue line). **D.** Representative recovery curve plotted in Mathematica (Appendix IC) (left) and representative fitting (red line) (right) for determining D.

compensate for global photobleaching due to imaging, a background ROI (Figure 27B, top right) needed to be measured and exported. The FRAP data must then be normalized to the background at every time interval in the movie. This meant for an experiment with several conditions and technical replicates, a large number of files would need to be exported, compiled, and normalized. To accomplish this in a reasonable time frame an automated program became necessary. For this the python script found in Appendix A was written.

Finally, it was noticed that due to the rapid diffusion of lipids during photobleaching, the effective radius of the bleached area is in fact larger than what is input (Figure 27B, bottom left). This phenomenon, as well as a method to calculate the effective bleaching radius, was described by Kang *et al*. To do this, the intensity across the bleached region is measured and fit to equation 1. A script (Appendix C) was written for importing the intensities across the bleached region and fitting the data to equation 1 (Figure 27C).

Our goal was to determine diffusion coefficients using equation 2 from Kang *et al*., 2012 (218) for SLBs with and without pHLIP at high and low pH. To plot and fit data from multiple experiments simultaneously, the Mathematica notebook found in Appendix B was written which imports data from the files generated by the python script in Appendix A. A representative normalized FRAP curve and a fit to equation 2 can be seen in Figure 27D.

Lipid diffusion in the presence of pHLIP

With a valid FRAP protocol and practical data analysis pipeline in hand, we could begin testing the effects of pHLIP on lipid diffusion. Control experiments show that alteration in pH alone have no effect on diffusion (Figure 28). Together with the day to day homogeneity of SLB mobility, any alterations seen in the presence of pHLIP can be reasonably attributed to lipid-peptide interactions. Lipids were observed to diffuse at 0.42 ± 0.16 μm^2/sec at pH 7.4 while addition of pHLIP at a lipid to peptide ratio of 150:1 raised the diffusion coefficient to 0.86 ± 0.7 μm^2/sec at pH 7.4 and finally, dropping the pH to 4 resulted in a diffusion coefficient of 1.4 ± 1.9 μm^2/sec (Figure 28). While an upward trend is observed in these data, the wide variance of the data leaves no reliable conclusion to be drawn. The mobile fraction data of lipid only at pH 7.4 preliminarily indicates that the SLBs were of uniform mobility for any given experiment. The mobile fraction of the supported lipid bilayers shows a decrease upon addition of peptide and a further decrease to pH 4. Between sample variation in lipid mobility is relatively low and prior experiments indicate no significant change in mobile fraction or diffusion coefficient (Figure 29) upon decrease of pH from 7.4 to 4 on lipid only samples. This would indicate that the changes seen in the data presented here are likely due to the incorporation of pHLIP. However, the variability in the diffusion coefficients are too large to draw reliable conclusions.
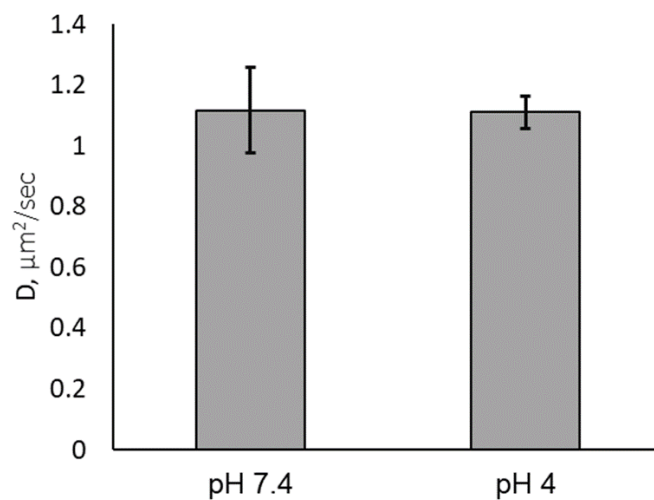
Figure 28. pH does not effect the rate of lipid diffusion.

Diffusion coefficients in 75% DOPC, 4% DOPS, 20% cholesterol, 1% NBD-PE bilayers at neutral and acidic pH. Bars are means ± S.D, $n = 2$. Difference is not significant via a student's t-test.
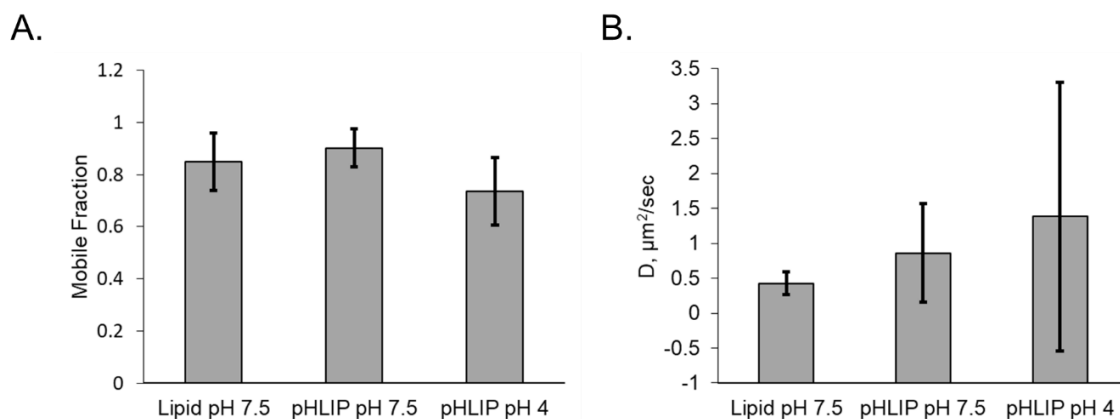
Figure 29. Effects of pHLIP on lipid diffusion.

A. Mobile fraction and **B.** diffusion coefficients of 99% DOPC, 1% NBD-PE lipid bilayers without pHLIP, +0.05 µM pHLIP at neutral pH (state II) and +0.05 µM pHLIP at acidic pH (state III). Bars are means ± S.D, $n = 2$. Differences are not significant.

4.5 Discussion

Here we have established a protocol for reliably producing supported lipid bilayers for FRAP experiments. We also provide here a protocol of exporting FRAP data from Leica image files (Appendix IA). We then wrote a data analysis pipeline starting with a Python program (Appendix IB) for formatting the exported data. These data can then be read into a Mathematica program (Appendix IC) and fit to equation 4 to determine a diffusion coefficient and mobile fraction for each FRAP recovery curve. We further provide a method for measuring the effective radius of bleaching by fitting data to equation 3 using a Mathematica program (Appendix ID). These programs are freely available for use and can be applied to FRAP data from any lipid composition collected via confocal microscopy.

We applied our FRAP method and data analysis pipeline to characterizing lipid diffusion of DOPC bilayers with and without pHLIP. We found that pH alone did not alter lipid diffusion. When pHLIP was added, shifts in D were observed but the magnitude of these shifts was highly variable making any interpretation impossible. It is possible that this is due to pHLIP-induced heterogeneities in the SLBs. D for SLBs prior to the addition of pHLIP was consistent (Figure 29B, lipid at pH 7.5). Only after adding pHLIP did the variability in the data increase. It is possible that upon insertion, some of the pHLIP molecules are interacting with the glass slide acting as anchors which could have a different effect on lipid diffusion than pHLIP which is freely diffusing with the lipids. This hypothesis

could be tested by performing FRAP experiments on tethered lipid bilayers on glass slides. Tethered lipid bilayers employ PEGylated lipids to establish a separation between the bilayer headgroups and the glass slide.

Experiments with pHLIP in tethered bilayers or any pH responsive peptide in either SLBs or tethered bilayers can provide interesting information about how these peptides impact the lipid environment which they target. Understanding the interplay between pH responsive peptides and cell membranes will allow researchers better understand the mechanisms by which these peptides function and allow for the design more effective peptides.

Appendix I Python and Mathematica Scripts

A. FRAP analysis step-by-step protocol

1. Create a file to contain the image exports, Python code and Mathematica notebooks

2. Open Lif project in LASX

3. Select a video and open the second of the two series (the one that begins with the first bleached image)

4. Click on the "Quantify" tab

5. Draw an ROI over the bleached area, resize to correct diameter. Copy that ROI and move the copy to another region of the image for background measurements

     *make sure "Annotations" is not highlighted when you draw ROI

     ** when you open different images series these ROIs will remain in the same X,Y positions

6. In "Tools" tab select "Stack Profile" under Tool and "All in One" under Sort Charts by Channels and ROIs

7. With ROIs in place right click on intensity plot, select "Export" then "Excel"

     a. For each pre bleached images series name the files PreData1, PreData2…

     b. For each post bleach image series name the files FrapData1, FrapData2…

*This naming convention is used by the Python code and must

correctly adhere to spelling and case

8. Using the command line, navigate to the directory containing the "FRAP

Data Excel" (Appendix B) python file

9. Open the file in your text editor (Suggested: Vim)

10. Under the import functions where the code generates the file path and file

name change the .xlsx files names to your choice (they must be the same),

save and exit to the command line

11. To run the python script type python scriptname.py in the command line

    a. The code will process all of the exported files and save the new data

    to a new file which you named in step 10

    b. The program quits and exits when it finds no more files to process

    and will print to the command line "File __not found! Exiting"

12. The new file should be in the correct directory and is now ready for

analysis in Mathematica notebook (Appendix C)

B. Python script which compiles and correctly formats .csv files exported from Leica FRAP images for import into Mathematica script (B)

```python
import openpyxl
import csv
import numpy
import os


# Writing new excel file with times, intensities, and normalized
intensities
filepath = os.getcwd()+"\FranFrapData.xlsx"
wb = openpyxl.Workbook()
dest_filename = 'FranFrapData.xlsx'

j = 0
while True:
    j += 1
    preFile = 'PreData' + str(j) + '.csv' #loop though
sequentially named PreData_ files
    frapFile = 'FrapData' + str(j) + '.csv' #loop through
sequntially named FrapData_ files
    if not os.path.isfile(preFile):
        print('File ' + preFile + ' not found! Exiting') # break
loop when PreData_ file not found
        break
    if not os.path.isfile(frapFile):
        print('File ' + frapFile + ' not found! Exiting') #break
loop when FrapDat_ not found
        break

    #Opening Exported CSVs and copying times and intensities
    #initializing list variables to recieve values
    preTimes = []
    preIntensities = []
    preBackground = []
    frapTimes = []
    frapIntensities = []
    frapBackground = []

    with open(preFile, newline='') as csvfile:  #while each
PreData file is open
        reader = csv.reader(csvfile, delimiter=',')
        next(reader) #ignore first line
        next(reader) #ignore sceond line
        for row in reader:
            time = float(row[0]) #floating point number needs to
be specified, otherwise string
            intensity = float(row[1])
            background = float(row[2])
            preTimes.append(time)
            preIntensities.append(intensity)
            preBackground.append(background)
```

117

```
    with open(frapFile, newline ='') as csvfile: #while each
FrapData file is open
        reader = csv.reader(csvfile, delimiter=',')
        next(reader)
        next(reader)
        for row in reader:
            time = float(row[0])
            intensity = float(row[1])
            background = float(row[2])
            frapTimes.append(time)
            frapIntensities.append(intensity)
            frapBackground.append(background)


    # Dividing bleached ROI by background ROI = Normalized
intensities
    # converting each list to requisite array for numpy
    frapInt = numpy.array(frapIntensities)
    frapBack = numpy.array(frapBackground)
    preInt = numpy.array(preIntensities)
    preBack = numpy.array(preBackground)
    preNorm = numpy.array(preBackground)
    frapNorm = numpy.array(frapBackground)
    NormList = []
    PreNormList = []

    #numpy.divide(dividend array, divisor array, output)
    numpy.divide(frapInt,frapBack,frapNorm)
    numpy.divide(preInt, preBack, preNorm)

    NormList = numpy.array(frapNorm).tolist()
    PreNormList = numpy.array(preNorm).tolist()

    #wrting into consecutive sheets of new excel workbook
    ws1 = wb.create_sheet("Frap" + str(j), j-1)
    header = ['Time','Bleached ROI','Background
ROI','Normalized']

    for i in range(1, len(header)+1):
        ws1.cell(row=1,column=i).value=header[i-1] #Column
headings

    #Column 1
    for i in range(1,len(preTimes)+1):
        ws1.cell(row=i+1,column=1).value=-preTimes[len(preTimes)-
i]-0.578 # pre-bleach times counting up to -0.578 starting from
last pretime value
    for i in range(1,len(frapTimes)+1):

ws1.cell(row=i+len(preTimes)+1,column=1).value=frapTimes[i-1]
#copying over post bleach times after prebleach times
```

```
    #Column 2
    for i in range(1,len(preIntensities)+1):
        ws1.cell(row=i+1,column=2).value=preIntensities[i-1]
#pre-bleach intensities first
    for i in range(1,len(frapIntensities)+1):

ws1.cell(row=i+len(preIntensities)+1,column=2).value=frapIntensit
ies[i-1] #post-bleach intesities after pre-bleach

    #Column 3
    for i in range(1,len(preBackground)+1):
        ws1.cell(row=i+1,column=3).value=preBackground[i-1]
#background pre-bleach intensities
    for i in range(1,len(frapBackground)+1):

ws1.cell(row=i+len(preBackground)+1,column=3).value=frapBackgroun
d[i-1] #background post-bleach vaules

    #Column 4
    for i in range(1,len(preNorm)+1):
        ws1.cell(row=i+1,column=4).value=preNorm[i-1] #Normalized
pre-bleach intensities
    for i in range(1,len(frapNorm)+1):
        ws1.cell(row=i+len(preNorm)+1,column=4).value=frapNorm[i-
1] #Normalized post-bleach intensities

wb.save(filepath)
```

C. Mathematica script that plots and fits FRAP data for diffusion coefficients

```
Model
frap = Fi*(1.0 - kappa/(1.0 + gamma^2 + 8.0*t*d/re^2))*
    Mf + (1.0 - Mf)*F0;

Import L only Data
SetDirectory[NotebookDirectory[]];
fnames = FileNames["*.xlsx"];
fnames // TableForm
FrapData =
  Table[Map[{#[[1]], #[[2]]} &,
    Import["L+PNoRinses030818.xlsx", {"Data", i, All, {1, 4}}]],
{i,
    Range[1, 8, 1]}];
Table[ListLinePlot[FrapData[[i]], PlotStyle -> Black,
  PlotRange -> All, FrameLabel -> {"Time, sec", "Intensity"},
  Frame -> {{Automatic, None}, {Automatic, None}}], {i,
  Length[FrapData]}]
x = Table[
  ListLinePlot[FrapData[[i]][[13 ;;]], PlotStyle -> Black,
   PlotRange -> All, FrameLabel -> {"Time, sec", "Intensity"},
   Frame -> {{Automatic, None}, {Automatic, None}}], {i,
   Length[FrapData]}]

Analyze Lipid only
kappaRule = {kappa -> (Fi - F0)/Fi*(1.0 + gamma^2)};
F = Take[FrapData[[1, 13 ;;, 2]]];
F0 = F[[1]];
Fi = 1.0;
gamma = rn/re;
rn = 2.0;
re = 5.8;
Mf0 = 0.0;
d0 = 2.0;
nlm = Table[
   NonlinearModelFit[
    FrapData[[i]][[13 ;;]], {frap /. kappaRule}, {{Mf, Mf0}, {d,
d0}},
      t, MaxIterations -> 1000], {i, Length[FrapData]}];
fitdata =
 Table[Show[x[[i]],
   Plot[nlm[[i]][t], {t, -5, 140}, PlotStyle -> {Red, Thick}]],
{i,
   Length[nlm]}]
fittable =
 Table[nlm[[i]][{"ParameterConfidenceIntervalTable"}], {i,
    Length[FrapData]}] // TableForm
dc = Table[
  nlm[[i]]["ParameterTableEntries"][[2, 1]], {i, Length[nlm]}]
A1 = Table[
```

```
    nlm[[i]]["ParameterTableEntries"][[1, 1]], {i, Length[nlm]}]
residuals =
 Table[ListPlot[
   Transpose[{FrapData[[i]][[13 ;;, 1]],
nlm[[i]]["FitResiduals"]}],
   PlotStyle -> {Black, Large}, PlotRange -> All,
   FrameLabel -> {"Time, sec", "Residuals"},
   Frame -> {{Automatic, None}, {Automatic, None}}], {i,
   Length[FrapData]}]

Import Lipid + Peptide pH 7.4 Data
SetDirectory[NotebookDirectory[]];
fnames = FileNames["*.xlsx"];
fnames // TableForm
FrapData =
  Table[Map[{#[[1]], #[[2]]} &,
    Import["L+PNoRinses030818.xlsx", {"Data", i, All, {1, 4}}]],
{i,
    Range[8, 16, 1]}];
Table[ListLinePlot[FrapData[[i]], PlotStyle -> Black,
  PlotRange -> All, FrameLabel -> {"Time, sec", "Intensity"},
  Frame -> {{Automatic, None}, {Automatic, None}}], {i,
  Length[FrapData]}]
x = Table[
  ListLinePlot[FrapData[[i]][[13 ;;]], PlotStyle -> Black,
   PlotRange -> All, FrameLabel -> {"Time, sec", "Intensity"},
   Frame -> {{Automatic, None}, {Automatic, None}}], {i,
   Length[FrapData]}]

Analyze Lipid + Peptide pH 7.4
kappaRule = {kappa -> (Fi - F0)/Fi*(1.0 + gamma^2)};
F = Take[FrapData[[1, 13 ;;, 2]]];
F0 = F[[1]];
Fi = 1.0;
gamma = rn/re;
rn = 2.0;
re = 6.8;
Mf0 = 0.0;
d0 = 2.0;
nlm = Table[
   NonlinearModelFit[
    FrapData[[i]][[13 ;;]], {frap /. kappaRule}, {{Mf, Mf0}, {d,
d0}},
     t, MaxIterations -> 1000], {i, Length[FrapData]}];
fitdata =
 Table[Show[x[[i]],
   Plot[nlm[[i]][t], {t, -5, 140}, PlotStyle -> {Red, Thick}]],
{i,
   Length[nlm]}]
fittable =
 Table[nlm[[i]][{"ParameterConfidenceIntervalTable"}], {i,
    Length[FrapData]}] // TableForm
dc = Table[
  nlm[[i]]["ParameterTableEntries"][[2, 1]], {i, Length[nlm]}]
```

```
A1 = Table[
  nlm[[i]]["ParameterTableEntries"][[1, 1]], {i, Length[nlm]}]
residuals =
 Table[ListPlot[
   Transpose[{FrapData[[i]][[13 ;;, 1]],
nlm[[i]]["FitResiduals"]}],
   PlotStyle -> {Black, Large}, PlotRange -> All,
   FrameLabel -> {"Time, sec", "Residuals"},
   Frame -> {{Automatic, None}, {Automatic, None}}], {i,
   Length[FrapData]}]

Import L+P 4 Data
SetDirectory[NotebookDirectory[]];
fnames = FileNames["*.xlsx"];
fnames // TableForm
FrapData =
  Table[Map[{#[[1]], #[[2]]} &,
    Import["L+PNoRinses030818.xlsx", {"Data", i, All, {1, 4}}]],
{i,
    Range[17, 24, 1]}];
Table[ListLinePlot[FrapData[[i]], PlotStyle -> Black,
  PlotRange -> All, FrameLabel -> {"Time, sec", "Intensity"},
  Frame -> {{Automatic, None}, {Automatic, None}}], {i,
  Length[FrapData]}]
x = Table[
  ListLinePlot[FrapData[[i]][[13 ;;]], PlotStyle -> Black,
   PlotRange -> All, FrameLabel -> {"Time, sec", "Intensity"},
   Frame -> {{Automatic, None}, {Automatic, None}}], {i,
   Length[FrapData]}]

Analyze L+P 4
kappaRule = {kappa -> (Fi - F0)/Fi*(1.0 + gamma^2)};
F = Take[FrapData[[1, 13 ;;, 2]]];
F0 = F[[1]];
Fi = 1.0;
gamma = rn/re;
rn = 2.0;
re = 10.752715075200687;
Mf0 = 0.0;
d0 = 2.0;
nlm = Table[
   NonlinearModelFit[
    FrapData[[i]][[13 ;;]], {frap /. kappaRule}, {{Mf, Mf0}, {d,
d0}},
     t, MaxIterations -> 1000], {i, Length[FrapData]}];
fitdata =
 Table[Show[x[[i]],
   Plot[nlm[[i]][t], {t, -5, 140}, PlotStyle -> {Red, Thick}]],
{i,
   Length[nlm]}]
fittable =
 Table[nlm[[i]][{"ParameterConfidenceIntervalTable"}], {i,
    Length[FrapData]}] // TableForm
dc = Table[
```

```
   nlm[[i]]["ParameterTableEntries"][[2, 1]], {i, Length[nlm]}]
A1 = Table[
   nlm[[i]]["ParameterTableEntries"][[1, 1]], {i, Length[nlm]}]
residuals =
 Table[ListPlot[
   Transpose[{FrapData[[i]][[13 ;;, 1]],
nlm[[i]]["FitResiduals"]}],
   PlotStyle -> {Black, Large}, PlotRange -> All,
   FrameLabel -> {"Time, sec", "Residuals"},
   Frame -> {{Automatic, None}, {Automatic, None}}], {i,
   Length[FrapData]}]
```

D. Mathematica script to calculate effective bleaching radius from data exported from FRAP images

```
Model
f = 1 - K * Exp[-x^2 / re^2];

Import and Fit Data
SetDirectory[NotebookDirectory[]];
fnames = FileNames["*.xlsx"];
fnames // TableForm
Data = Table[
   Map[{#[[1]], #[[2]]} &,
    Import["ReInputL+P7.4.xlsx", {"Data", i, All, {1, 2}}]], {i,
    Range[1, 1, 1]}];
Table[ListLinePlot[Data[[i]], PlotStyle -> Black, PlotRange ->
All,
  FrameLabel -> {"Microns", "Intensity"},
  Frame -> {{Automatic, None}, {Automatic, None}}], {i,
Length[Data]}]
F = Take[Data[[1, 2 ;;, 2]]];
K0 = Max[F] - Min[F];
re0 = 6;
nlm = Table[
   NonlinearModelFit[Data[[i]][[2 ;;]], {f}, {{re, re0}, {K,
K0}}, x,
    MaxIterations -> 1000], {i, Length[Data]}];
fitdata =
 Show[ListLinePlot[Data[[1]]],
  Plot[nlm[[1]][x], {x, -10, 12}, PlotStyle -> {Red, Thick}]]
fittable =
 Table[nlm[[i]][{"ParameterConfidenceIntervalTable"}], {i,
    Length[Data]}] // TableForm
```

Chapter IV. Conclusion

5.1 Conclusions

In Chapter II we explored the association of a novel EphA2-targeting peptide with EphA2 and its effects of cell morphology. We demonstrated via co-localization analysis and co-immunoprecipitation that TYPE7 interacts directly with EphA2 in A375 cancer cells. Ligand-dependent activation of EphA2 results in cell contraction and decreased cell migration and proliferation. While it was found that TYPE7 treatment reduces cancer cell migration, we did not find that it significantly resulted in cell contraction. This could indicate that the tyrosine, Y772, which TYPE7 phosphorylates is not sufficient to induce downstream signaling that results in cell contraction.

While we were able to show that TYPE7 has a specific effect on EphA2 signaling we do not understand the mechanism by which it acts. In order to better understand TYPE7 and to design more effective TMD targeting peptides, we need a better understanding of this region of EphA2. Thus, we sought, in Chapter III, to investigate how the TM and JM of EphA2 contribute to changes in signaling.

We used bilayer thickness and hydrophobic matching to recapitulate the two TMD configurations of our TMJM peptide which correspond to ligand-independent and ligand-dependent signaling. We proposed that thick bilayers promote the ligand-independent state while thin bilayers promote the ligand-dependent state. With this system we investigated changes in the JM and oligomerization. Using tryptophan fluorescence, we found that bilayer thickness

126

did result in changes in the local environment of the JM but not due to its distance from the bilayer interface changing. We then also showed that TMJM engages in biologically relevant dimerization using a novel single-molecule TIRF technique.

Next, we investigated if the polybasic residues of the JM participate in electrostatic interactions with the anionic lipid PIP_2. Tryptophan fluorescence experiments showed that, in thick bilayers, the environment of the tryptophan changes with PIP_2 and that this change is reversible upon addition of calcium. No changes occurred in thin bilayers. FRET experiments showed that the distance between the tryptophan and a fluorescently labeled lipid headgroup changed only in thick bilayers with PIP_2. Again, no PIP_2-dependent changes were observed in thin bilayers. Fluorescence and FRET data indicate that the JM is sensitive to interactions with PIP_2 only in the ligand-independent conformation. Finally, we found that PIP_2 promotes dimerization of TMJM in thick bilayers, again corresponding to the ligand-independent state. These data informed our proposed model in which PIP_2 regulates EphA2 by stabilizing ligand-independent dimers via electrostatic interactions with the JM. We found that this interaction is specific to PIP_2 as PS was unable to effect the same changes in the JM or dimerization. This work demonstrated, for the first time, that there is, in EphA2, a coupling of TMD orientation and JM-lipid associations which is at least specific to phosphatidylinositol lipids.

The results from Chapter III highlight how important protein-lipid interactions are to the function of membrane proteins. To better understand how lipids and TMDs interact with each other, in Chapter IV, we developed a FRAP protocol and automated data analysis pipeline for experiments conducted on supported lipid bilayers using confocal microscopy. The resulting protocol was robust and valid as it reproduced known diffusion coefficients for SLBs. Further, the Mathematica and Python programs presented in Chapter IV allow for accurate and fast determination of diffusion coefficients from Leica image files. We used pHLIP as a model TMD for to determine if it has an effect on lipid diffusion. We were able to measure lipid diffusion before and after the addition of pHLIP in the same bilayer. While this did not result in a statistically significant difference in D, it did cause changes in the variability of D (i.e the standard deviation of D after addition of pHLIP was much larger). Because experiments were conducted on the same bilayer these changes must be due to the presence of pHLIP. Changes to the experimental setup, such as using tethered bilayers instead of supported bilayers, may lead to improvements which allow for difference in the mean value of D to be detectable with pHLIP.

In summary, I have investigated transmembrane-lipid interactions of EphA2 and pH responsive peptides using cell biology together with classical and novel biophysical approaches. These projects have contributed to the understanding of how pH responsive peptides interact with lipids and their protein targets. We also characterized activation state-dependent TM-JM lipid

interactions in EphA2 which both advances the understanding of this developmentally important RTK and can aid designing targeted therapies.

5.2 Future Directions

We have shown that TYPE7 directly interacts with EphA2 in cancer cells. This interaction has been shown to change levels of tyrosine phosphorylation and inhibit cell migration. However, the mechanism by which TYPE7 exerts these effects is not known. We have speculated that by forming a dimer with the EphA2 TMD, TYPE7 may occlude the ligand-independent specific interface and thereby promote the ligand-dependent configuration. We have also speculated that interactions of the poly-glutamic acid stretch of TYPE7 may interact with the polybasic JM of EphA2 and alter its activation state. Based on the findings described in Chapter III, experiments with TYPE7 and TMJM in thin and thick bilayers may provide insights into the mechanism of TYPE7.

We have demonstrated that in thick bilayers (which corresponds to the ligand-independent configuration) TMD and JM are sensitive to interactions with PIP_2. This interaction drives changes in JM and environment and promotes TMD dimerization. If TYPE7 does in fact interact preferentially with the EphA2 ligand-independent interface this could be detected by repeating experiments detailed in Chapter III with TYPE7. I would expect to find that TYPE7 decreases dimerization of TMJM in single-molecule TIRF experiments in SMALPs comprised of 22:1 PC.

We further hypothesized that the poly-glutamic acid stretch at the C-terminus of TYPE7 interacts with the polybasic JM residues of TMJM. If this interaction occurs it could be detectable via tryptophan experiments. We know that interactions with PIP_2 alter the environment of the TMJM tryptophan (Chapter III) so if the addition of TYPE7 also alters the tryptophan environment it would be detectable these experiments. First, I propose that fluorescence studies be conducted in 22:1 PC liposomes containing TMJM as described with and without TYPE7 to see if TYPE7 alters the JM alone. Then, the experiments could be repeated in liposomes with 22:1 PC and PIP_2. If electrostatic interactions between TMJM and TYPE7 outcompete the interactions with PIP_2, I would expect to see a different outcome from this experiment. It may be that TYPE7 reverses the PIP_2 induced fluorescent changes or changes the fluorescence in a different way. These experiments would be complimented with tryptophan-dansyl PE FRET experiments to obtain quantitative information about changes in distance of the TMJM tryptophan and bilayer headgroups.

In Chapter III, we propose that the juxtamembrane region of EphA2 interacts with PIP_2 in a manner that involves PIP_2 clustering around the polybasic JM residues and/or causes the insertion of the JM into the core of the bilayer. These two hypotheses could be supported or rejected by employing different experiments. To investigate clustering of PIP_2 around the TMJM peptide, we have begun a collaboration with the lab of Adam Smith at the University of Akron. They employ fluorescence correlation spectroscopy (FCS) to measure the rate of

diffusion of lipids. If lipids cluster, they diffuse more slowly. They will conduct FCS on SLBs containing fluorescently labeled PIP$_2$ to measure a rate of diffusion. Then they will add TMJM to detect if it slows down the rate of diffusion thereby confirming or rejecting the cluster hypothesis.

In addition, the burial of the tryptophan of TMJM can be assessed via various quenching experiments. Quenchers, like acrylamide, can be added to liposomes containing TMJM to determine how solvated the JM is. If the tryptophan is not buried in the membrane a higher amount of quenching would be expected. To compliment this approach, spin-labeled phospholipids which quench fluorescence can be employed. The spin label can be added at different positions of the lipid acyl chain at various depths in the membrane. If the tryptophan of TMJM is buried in the presence of PIP$_2$, this experiment would show higher levels of quenching.

We saw in Chapter III that in thick membranes, PIP$_2$ promotes self-assembly of TMJM. To study the effects of PIP$_2$ on the oligomerization of full-length EphA2 in cells, we have proposed FCS experiments. Again, our collaborators in the Smith lab will perform these experiments. They will use cells which express a full-length EphA2 labeled with GFP. There are several drugs which can alter the levels of PIP$_2$ at the plasma membrane which can be added to cells. Using FCS they will assess a baseline diffusion of EphA2. When cells are treated with drugs which deplete PIP$_2$, we would expect based on our data, to see a decrease in dimerized EphA2 and therefore increase the rate of

diffusion. Conversely, we expect drugs which increase the levels of PIP2 to promote more dimerization of EphA2 and decrease the rate of diffusion.

Our oligomerization data in Chapter III suggests another possibility about EphA2 in cells. With PIP_2, the ligand-independent conformation is more dimeric than the ligand-dependent configuration. It is possible, that in cells, the HR dimer is more energetically favorable than the GZ dimer keeping receptor in ligand-independent state until ligand activation and other parts of the protein from TMDs to glycine zipper. To test this hypothesis in thin and thick bilayers we would need to determine which dimer interface is utilized in each. This could be achieved by changing different TM residues to cysteines and conducting cross-linking studies to identify the dimer interface in each lipid. We could then use the single-molecule TIRF experiments in SMALPs to determine dissociation constants in thin and thick bilayers with PIP_2. These additional studies on the TMD of EphA2 are the next steps toward characterizing the role of PIP_2 plays in modulating activity of the receptor in cells.

References

1. Dobson, L., Reményi, I., and Tusnády, G. E. (2015) The human transmembrane proteome. *Biol. Direct.* **10**, 1–18

2. Jp, O., and Al, H. (2006) How many drug targets are there ? PubMed Commons. *Nat. Rev. Drug Discov.* **5**, 10

3. Cuatrecasas, P. (1974) Membrane Receptors. *Annu. Rev. Biochem.* **43**, 169–214

4. Fredriksson, R., Lagerström, M. C., Lundin, L. G., and Schiöth, H. B. (2003) The G-protein-coupled receptors in the human genome form five main families. Phylogenetic analysis, paralogon groups, and fingerprints. *Mol. Pharmacol.* **63**, 1256–1272

5. Robinson, D. R., Wu, Y. M., and Lin, S. F. (2000) The protein tyrosine kinase family of the human genome. *Oncogene.* **19**, 5548–5557

6. Venkatakrishnan, A. J., Deupi, X., Lebon, G., Tate, C. G., Schertler, G. F., and Madan Babu, M. (2013) Molecular signatures of G-protein-coupled receptors. *Nature.* **494**, 185–194

7. Lemmon, M. A., and Schlessinger, J. (2010) Cell signaling by receptor tyrosine kinases. *Cell.* **141**, 1117–1134

8. Matthews, E. E., Zoonens, M., and Engelman, D. M. (2006) Dynamic Helix Interactions in Transmembrane Signaling. *Cell.* **127**, 447–450

9. Lemmon, M. A., Flanagan, J. M., Treutlein, H. R., Zhang, J., and Engelman, D. M. (1992) Sequence Specificity in the Dimerization of Transmembrane β-Helixes. *Biochemistry.* **31**, 12719–12725

10. Treutlein, H. R., Lemmon, M. A., Engelman, D. M., and Brunger, A. T. (1992) The Glycophorin A Transmembrane Domain Dimer : Sequence-Specific Propensity for a Right-Handed Supercoil of Helixes. *Biochemistry.* **31**, 12726–12732

11. Walters, R. F. S., and DeGrado, W. F. (2006) Helix-packing motifs in membrane proteins. *Proc. Natl. Acad. Sci. U. S. A.* **103**, 13658–13663

12. Gimpelev, M., Forrest, L. R., Murray, D., and Honig, B. (2004) Helical packing patterns in membrane and soluble proteins. *Biophys. J.* **87**, 4075–4086

13. Kim, S., Jeon, T., Oberai, A., Yang, D., Schmidt, J. J., and Bowie, J. U. (2005) Transmembrane glycine zippers : Physiological and pathological roles in membrane proteins

14. Anderson, S. M., Mueller, B. K., Lange, E. J., and Senes, A. (2017) Combination of Cα-H Hydrogen Bonds and van der Waals Packing Modulates the Stability of GxxxG-Mediated Dimers in Membranes. *J. Am. Chem. Soc.* **139**, 15774–15783

15. Russ, W. P., and Engelman, D. M. (2000) The GxxxG motif: A framework for transmembrane helix-helix association. *J. Mol. Biol.* **296**, 911–919

16. Senes, A., Ubarretxena-Belandia, I., and Engelman, D. M. (2001) The Cα -H⋯O hydrogen bond: A determinant of stability and specificity in transmembrane helix interactions. *Proc. Natl. Acad. Sci. U. S. A.* **98**, 9056–

9061

17. Chambers, P., Pringle, C. R., and Easton, A. J. (1990) Heptad repeat sequences are located adjacent to hydrophobic regions in several types of virus fusion glycoproteins. *J. Gen. Virol.* **71**, 3075–3080

18. Langosch, D., and Heringa, J. (1998) Interaction of transmembrane helices by a knobs-into-holes packing characteristic of soluble coiled coils. *Proteins Struct. Funct. Genet.* **31**, 150–159

19. Fantl, W. J., Johnson, D. E., and Williams, L. T. (1993) Signalling by receptor tyrosine kinases. *Annu. Rev. Biochem.* **62**, 453–481

20. Paul, M. D., and Hristova, K. (2019) The transition model of RTK activation: A quantitative framework for understanding RTK signaling and RTK modulator activity. *Cytokine Growth Factor Rev.* **49**, 23–31

21. Tamagaki, H., Furukawa, Y., Yamaguchi, R., Hojo, H., Aimoto, S., Smith, S. O., and Sato, T. (2014) Coupling of transmembrane helix orientation to membrane release of the Juxtamembrane Region in FGFR3. *Biochemistry*. **53**, 5000–5007

22. Sharonov, G. V, Bocharov, E. V, Kolosov, P. M., Astapova, M. V, Arseniev, A. S., and Feofanov, A. V (2014) Point Mutations in Dimerization Motifs of the Transmembrane Domain Stabilize Active or Inactive State of the EphA2 Receptor Tyrosine Kinase *. **289**, 14955–14964

23. Singh, D. R., King, C., Salotto, M., and Hristova, K. (2020) Revisiting a controversy: The effect of EGF on EGFR dimer stability. *Biochim. Biophys. Acta - Biomembr.* **1862**, 183015

24. Cymer, F., and Schneider, D. (2010) Transmembrane helix-helix interactions involved in ErbB receptor signaling. *Cell Adhes. Migr.* **4**, 299–312

25. Lorent, J. H., Diaz-Rohrer, B., Lin, X., Spring, K., Gorfe, A. A., Leventhal, K. R., and Leventhal, I. (2017) Structural determinants and functional consequences of protein affinity for membrane rafts. *Nat. Commun.* **8**, 1–9

26. Cunningham, O., Andolfo, A., Santovito, M. L., Iuzzolino, L., Blasi, F., and Sidenius, N. (2003) Dimerization controls the lipid raft partitioning of uPAR / CD87 and regulates its biological functions

27. Hunt, J. F., Rath, P., Rothschild, K. J., and Engelman, D. M. (1997) Spontaneous, pH-dependent membrane insertion of a transbilayer α-helix. *Biochemistry*. **36**, 15177–15192

28. Hunt, J. F., Earnest, T. N., Bousché, O., Kalghatgi, K., Reilly, K., Horváth, C., Rothschild, K. J., and Engleman, D. M. (1997) A biophysical study of integral membrane protein folding. *Biochemistry*. **36**, 15156–15176

29. Reshetnyak, Y. K., Andreev, O. A., Segala, M., Markin, V. S., and Engelman, D. M. (2008) Energetics of peptide (pHLIP) binding to and folding across a lipid bilayer membrane. *Proc. Natl. Acad. Sci. U. S. A.* **105**, 15340–15345

30. Scott, H. L., Westerfield, J. M., and Barrera, F. N. (2017) Determination of the Membrane Translocation pK of the pH-Low Insertion Peptide. *Biophys.*

J. **113**, 869–879

31. Andreev, O. A., Dupuy, A. D., Segala, M., Sandugu, S., Serra, D. A., Chichester, C. O., Engelman, D. M., and Reshetnyak, Y. K. (2007) Mechanism and uses of a membrane peptide that targets tumors and other acidic tissues in vivo. *Proc. Natl. Acad. Sci.* **104**, 7893–7898

32. Tannock, I. F., and Rotin, D. (1989) Acid pH in Tumors and Its Potential for Therapeutic Exploitation. *Cancer Res.* **49**, 4373–4384

33. Reshetnyak, Y. K., Andreev, O. A., Lehnert, U., and Engelman, D. M. (2006) Translocation of molecules into cells by pH-dependent insertion of a transmembrane helix. *Proc. Natl. Acad. Sci. U. S. A.* **103**, 6460–6465

34. An, M., Wijesinghe, D., Andreev, O. A., Reshetnyak, Y. K., and Engelman, D. M. (2010) PH-(low)-insertion-peptide (pHLIP) translocation of membrane impermeable phalloidin toxin inhibits cancer cell proliferation. *Proc. Natl. Acad. Sci. U. S. A.* **107**, 20246–20250

35. Zoonens, M., Reshetnyak, Y. K., and Engelman, D. M. (2008) Bilayer interactions of pHLIP, a peptide that can deliver drugs and target tumors. *Biophys. J.* **95**, 225–235

36. Burns, K. E., McCleerey, T. P., and Thévenin, D. (2016) PH-Selective Cytotoxicity of pHLIP-Antimicrobial Peptide Conjugates. *Sci. Rep.* **6**, 1–10

37. Yao, L., Daniels, J., Moshnikova, A., Kuznetsoz, S., Ahmed, A., Engelman, D. M., Reshetnayak, Y. K., and Andreev, O. A. (2013) pHLIP peptide targets nanogold particles to tumors Lan. *Proc. Natl. Acad. Sci. U. S. A.* **110**, 465–470

38. Son, S. M., Yun, J., Lee, S. H., Han, H. S., Lim, Y. H., Woo, C. G., Lee, H. C., Song, H. G., Gu, Y. M., Lee, H. J., and Lee, O. J. (2019) Therapeutic Effect of pHLIP-mediated CEACAM6 Gene Silencing in Lung Adenocarcinoma. *Sci. Rep.* **9**, 1–11

39. Özeş, A. R., Wang, Y., Zong, X., Fang, F., Pilrose, J., and Nephew, K. P. (2017) Therapeutic targeting using tumor specific peptides inhibits long non-coding RNA HOTAIR activity in ovarian and breast cancer. *Sci. Rep.* **7**, 1–11

40. Wyatt, L. C., Lewis, J. S., Andreev, O. A., Reshetnyak, Y. K., and Engelman, D. M. (2017) Applications of pHLIP Technology for Cancer Imaging and Therapy. *Trends Biotechnol.* **35**, 653–664

41. Daumar, P., Wanger-Baumann, C. A., Pillarsetty, N., Fabrizio, L., Carlin, S. D., Andreev, O. A., Reshetnyak, Y. K., and Lewis, J. S. (2012) Efficient 18F-labeling of large 37-amino-acid pHLIP peptide analogues and their biological evaluation. *Bioconjug. Chem.* **23**, 1557–1566

42. Vavere, A. L., Biddlecombe, G. B., Spees, W. M., Garbow, J. R., Wijesinghe, D., Andreev, O. A., Engelman, D. M., Reshetnyak, Y. K., and Lewis, J. S. (2009) A novel technology for the imaging of acidic prostate tumors by positron emission tomography. *Cancer Res.* **69**, 4510–4516

43. MacHoll, S., Morrison, M. S., Iveson, P., Arbo, B. E., Andreev, O. A., Reshetnyak, Y. K., Engelman, D. M., and Johannesen, E. (2012) In Vivo

pH imaging with 99mTc-pHLIP. *Mol. Imaging Biol.* **14**, 725–734

44. Adochite, R. C., Moshnikova, A., Carlin, S. D., Guerrieri, R. A., Andreev, O. A., Lewis, J. S., and Reshetnyak, Y. K. (2014) Targeting breast tumors with pH (Low) insertion peptides. *Mol. Pharm.* **11**, 2896–2905
45. Reshetnyak, Y. K., Yao, L., Zheng, S., Kuznetsov, S., Engelman, D. M., and Andreev, O. A. (2011) Measuring tumor aggressiveness and targeting metastatic lesions with fluorescent pHLIP. *Mol. Imaging Biol.* **13**, 1146–1156
46. Cruz-Monserrate, Z., Roland, C. L., Deng, D., Arumugam, T., Moshnikova, A., Andreev, O. A., Reshetnyak, Y. K., and Logsdon, C. D. (2014) Targeting pancreatic ductal adenocarcinoma acidic microenvironment. *Sci. Rep.* **4**, 1–8
47. Musial-Siwek, M., Karabadzhak, A., Andreev, O. A., Reshetnyak, Y. K., and Engelman, D. M. (2010) Tuning the insertion properties of pHLIP. *Biochim. Biophys. Acta - Biomembr.* **1798**, 1041–1046
48. Nguyen, V. P., Alves, D. S., Scott, H. L., Davis, F. L., and Barrera, F. N. (2015) A Novel Soluble Peptide with pH-Responsive Membrane Insertion. *Biochemistry.* **54**, 6567–6575
49. Alves, D. S., Westerfield, J. M., Shi, X., Nguyen, V. P., Stefanski, K. M., Booth, K. R., Kim, S., Morrell-Falvey, J., Wang, B. C., Abel, S. M., Smith, A. W., and Barrera, F. N. (2018) A novel pH-dependent membrane peptide that binds to EphA2 and inhibits cell migration. *Elife.* **7**, 1–22
50. Ullrich, A., and Schlessinger, J. (1990) Signal transduction by receptors with tyrosine kinase activity. *Cell.* **61**, 203–212
51. Hunter, T., and Blume-Jensen, P. (2001) Oncogenic kinase signalling. *Nature.* **411**, 355
52. Leppänen, V. M., Prota, A. E., Jeltsch, M., Anisimov, A., Kalkkinen, N., Strandin, T., Lankinen, H., Goldman, A., Ballmer-Hofer, K., and Alitalo, K. (2010) Structural determinants of growth factor binding and specificity by VEGF receptor 2. *Proc. Natl. Acad. Sci. U. S. A.* **107**, 2425–2430
53. Wiesmann, C., Fuh, G., Christinger, H. W., Eigenbrot, C., Wells, J. a, and Vos, A. M. De (1997) Resolution of VEGF Crystal Structure at 1 . 7 A in Complex with Domain 2 of the Flt-1 Receptor. *Cell.* **91**, 695–704
54. Barton, W. A., Tzvetkova-Robev, D., Miranda, E. P., Kolev, M. V., Rajashankar, K. R., Himanen, J. P., and Nikolov, D. B. (2006) Crystal structures of the Tie2 receptor ectodomain and the angiopoietin-2-Tie2 complex. *Nat. Struct. Mol. Biol.* **13**, 524–532
55. Wiesmann, C., Ultsch, M. H., Bass, S. H., and De Vos, A. M. (1999) Crystal structure of nerve growth factor in complex with the ligand- binding domain of the TrkA receptor. *Nature.* **401**, 184–188
56. Himanen, J. P., Yermekbayeva, L., Janes, P. W., Walker, J. R., Xu, K., Atapattu, L., Rajashankar, K. R., Mensinga, A., Lackmann, M., Nikolov, D. B., and Dhe-Paganon, S. (2010) Architecture of Eph receptor clusters. *Proc. Natl. Acad. Sci.* **107**, 10860–10865

57. Himanen, J. P., and Nikolov, D. B. (2003) Eph signaling: A structural view. *Trends Neurosci.* **26**, 46–51

58. Wehrman, T., He, X., Raab, B., Dukipatti, A., Blau, H., and Garcia, K. C. (2007) Structural and Mechanistic Insights into Nerve Growth Factor Interactions with the TrkA and p75 Receptors. *Neuron.* **53**, 25–38

59. Yuzawa, S., Opatowsky, Y., Zhang, Z., Mandiyan, V., Lax, I., and Schlessinger, J. (2007) Structural Basis for Activation of the Receptor Tyrosine Kinase KIT by Stem Cell Factor. *Cell.* **130**, 323–334

60. Schlessinger, J., Plotnikov, A. N., Ibrahimi, O. A., Eliseenkova, A. V., Yeh, B. K., Yayon, A., Linhardt, R. J., and Mohammadi, M. (2000) Crystal Structure of a Ternary FGF-FGFR-Heparin Complex Reveals a Dual Role for Heparin in FGFR Binding and Dimerization Joseph. *Mol. Cell.* **6**, 743–750

61. Nolen, B., Taylor, S., and Ghosh, G. (2004) Regulation of protein kinases: Controlling activity through activation segment conformation. *Mol. Cell.* **15**, 661–675

62. Hubbard, S. R. (2004) Juxtamembrane autoinhibition in receptor tyrosine kinases. *Nat. Rev. Mol. Cell Biol.* **5**, 464–470

63. Mol, C. D., Dougan, D. R., Schneider, T. R., Skene, R. J., Kraus, M. L., Scheibe, D. N., Snell, G. P., Zou, H., Sang, B. C., and Wilson, K. P. (2004) Structural basis for the autoinhibition and STI-571 inhibition of c-Kit tyrosine kinase. *J. Biol. Chem.* **279**, 31655–31663

64. Griffith, J., Black, J., Faerman, C., Swenson, L., Wynn, M., Lu, F., Lippke, J., and Saxena, K. (2004) The Structural Basis for Autoinhibition of FLT3 by the Juxtamembrane Domain. *Mol. Cell.* **13**, 169–178

65. Wybenga-Groot, L. E., Baskin, B., Ong, S. H., Tong, J., Pawson, T., and Sicheri, F. (2001) Structural basis for autoinhibition of the EphB2 receptor tyrosine kinase by the unphosphorylated juxtamembrane region. *Cell.* **106**, 745–757

66. Niu, X. L., Peters, K. G., and Kontos, C. D. (2002) Deletion of the carboxyl terminus of Tie2 enhances kinase activity, signaling, and function: Evidence for an autoinhibitory mechanism. *J. Biol. Chem.* **277**, 31768–31773

67. Pawson, T. (2004) Specificity in Signal Transduction: From Phosphotyrosine-SH2 Domain Interactions to Complex Cellular Systems. *Cell.* **116**, 191–203

68. Schlessinger, J., and Lemmon, M. A. (2003) SH2 and PTB domains in tyrosine kinase signaling. *Sci. STKE.* **2003**, 1–13

69. Schlessinger, J. (2000) Cell Signaling by Receptor Tyrosine Kinases. *Cell.* **103**, 211–225

70. Oda, K., Matsuoka, Y., Funahashi, A., and Kitano, H. (2005) A comprehensive pathway map of epidermal growth factor receptor signaling. *Mol. Syst. Biol.* 10.1038/msb4100014

71. Mohammadi, M., and Zinkle, A. (2018) A threshold model for receptor

tyrosine kinase signaling specificity and cell fate determination [version 1; referees: 4 approved]. *F1000Research*. **7**, 1–15

72. Furdui, C. M., Lew, E. D., Schlessinger, J., and Anderson, K. S. (2006) Autophosphorylation of FGFR1 kinase is mediated by a sequential and precisely ordered reaction. *Mol. Cell*. **21**, 711–717

73. Lew, E. D., Furdui, C. M., Anderson, K. S., and Schlessinger, J. (2009) The precise sequence of FGF receptor autophosphorylation is kinetically driven and is disrupted by oncogenic mutations. *Sci. Signal.* **2**, 1–11

74. Di Guglielmo, G. M., Baass, P. C., Ou, W. J., Posner, B. I., and Bergeron, J. J. M. (1994) Compartmentalization of SHC, GRB2 and mSOS, and hyperphosphorylation of Raf-1 by EGF but not insulin in liver parenchyma. *EMBO J.* **13**, 4269–4277

75. von Zastrow, M., and Sorkin, A. (2007) Signaling on the endocytic pathway. *Curr. Opin. Cell Biol.* **19**, 436–445

76. Mosesson, Y., Shtiegman, K., Katz, M., Zwang, Y., Vereb, G., Szollosi, J., and Yarden, Y. (2003) Endocytosis of receptor tyrosine kinases is driven by monoubiquitylation, not polyubiquitylation. *J. Biol. Chem.* **278**, 21323–21326

77. Huang, F., Lai, K. G., and Sorkin, A. (2009) EGF receptor ubiquitination is not necessary for its internalization (Proceedings of the National Academy of Sciences of the United States of America (2007) 104, 43, (16904-16909) DOI: 10.1073/pnas.0707416104). *Proc. Natl. Acad. Sci. U. S. A.* **106**, 14180

78. Pennock, S., and Wang, Z. (2008) A Tale of Two Cbls: Interplay of c-Cbl and Cbl-b in Epidermal Growth Factor Receptor Downregulation. *Mol. Cell. Biol.* **28**, 3020–3037

79. Burgess, A. W., Cho, H. S., Eigenbrot, C., Ferguson, K. M., Garrett, T. P. J., Leahy, D. J., Lemmon, M. A., Sliwkowski, M. X., Ward, C. W., and Yokoyama, S. (2003) An open-and-shut case? Recent insights into the activation of EGF/ErbB receptors. *Mol. Cell*. **12**, 541–552

80. Corless, C. L., and Heinrich, M. C. (2008) Molecular pathobiology of gastrointestinal stromal sarcomas. *Annu. Rev. Pathol. Mech. Dis.* **3**, 557–586

81. Paschka, P., Marcucci, G., Ruppert, A. S., Mrózek, K., Chen, H., Kittles, R. A., Vukosavljevic, T., Perrotti, D., Vardiman, J. W., Carroll, A. J., Kolitz, J. E., Larson, R. A., and Bloomfield, C. D. (2006) Adverse prognostic significance of KIT mutations in adult acute myeloid leukemia with inv(16) and t(8;21): A Cancer and Leukemia Group B study. *J. Clin. Oncol.* **24**, 3904–3911

82. Furitsu, T., Tsujimura, T., Tono, T., Ikeda, H., Kitayama, H., Koshimizu, U., Sugahara, H., Butterfield, J. H., Ashman, L. K., Kanayama, Y., Matsuzawa, Y., Kitamura, Y., and Kanakura, Y. (1993) Identification of mutations in the coding sequence of the proto-oncogene c-kit in a human mast cell leukemia cell line causing ligand-independent activation of c-kit product. *J.*

Clin. Invest. **92**, 1736–1744

83. Beadling, C., Jacobson-Dunlop, E., Hodi, F. S., Le, C., Warrick, A., Patterson, J., Town, A., Harlow, A., Cruz, F., Azar, S., Rubin, B. P., Muller, S., West, R., Heinrich, M. C., and Corless, C. L. (2008) KIT gene mutations and copy number in melanoma subtypes. *Clin. Cancer Res.* **14**, 6821–6828

84. Eswarakumar, V. P., Lax, I., and Schlessinger, J. (2005) Cellular signaling by fibroblast growth factor receptors. *Cytokine Growth Factor Rev.* **16**, 139–149

85. Smith, A., Robinson, V., Patel, K., and Wilkinson, D. G. (1997) The EphA4 and EphB1 receptor tyrosine kinases and ephrin-B2 ligand regulate targeted of branchial neural crest cells. *Curr. Biol.* **7**, 561–570

86. Xu, O., Alldus, G., Holder, N., and Wilkinson, D. G. (1995) Expression of truncated Sek-1 receptor tyrosine kinase disrupts the segmental restriction of gene expression in the Xenopus and zebrafish hindbrain. *Development.* **121**, 4005–4016

87. Adams, R. H., Wilkinson, G. A., Weiss, C., Diella, F., Gale, N. W., Deutsch, U., Risau, W., and Klein, R. (1999) Roles of ephrinB ligands and EphB receptors in cardiovascular development: Demarcation of arterial/venous domains, vascular morphogenesis, and sprouting angiogenesis. *Genes Dev.* **13**, 295–306

88. Gerety, S. S., Wang, H. U., Chen, Z. F., and Anderson, D. J. (1999) Symmetrical mutant phenotypes of the receptor EphB4 and its specific transmembrane ligand ephrin-B2 in cardiovascular development. *Mol. Cell.* **4**, 403–414

89. Harbott, L. K., and Nobes, C. D. (2005) A key role for Abl family kinases in EphA receptor-mediated growth cone collapse. *Mol. Cell. Neurosci.* **30**, 1–11

90. Vargas, L. M., Leal, N., Estrada, L. D., González, A., Serrano, F., Araya, K., Gysling, K., Inestrosa, N. C., Pasquale, E. B., and Alvarez, A. R. (2014) EphA4 activation of c-Abl mediates synaptic loss and LTP blockade caused by amyloid-β oligomers. *PLoS One.* 10.1371/journal.pone.0092309

91. Moresco, E. M. Y., and Koleske, A. J. (2003) Regulation of neuronal morphogenesis and synaptic function by Abl family kinases. *Curr. Opin. Neurobiol.* **13**, 535–544

92. Chen, Y., Fu, A. K. Y., and Ip, N. Y. (2012) Eph receptors at synapses: Implications in neurodegenerative diseases. *Cell. Signal.* **24**, 606–611

93. Fu, A. K. Y., Hung, K. W., Fu, W. Y., Shen, C., Chen, Y., Xia, J., Lai, K. O., and Ip, N. Y. (2011) APCCdh1mediates EphA4-dependent downregulation of AMPA receptors in homeostatic plasticity. *Nat. Neurosci.* **14**, 181–191

94. Hong, J. Y., Shin, M. H., Chung, K. S., Kim, E. Y., Jung, J. Y., Kang, Y. A., Kim, Y. S., Kim, S. K., Chang, J., and Park, M. S. (2015) EphA2 receptor signaling mediates inflammatory responses in lipopolysaccharide-induced lung injury. *Tuberc. Respir. Dis. (Seoul).* **78**, 218–226

95. Carpenter, T. C., Schroeder, W., Stenmark, K. R., and Schmidt, E. P. (2012) Eph-A2 promotes permeability and inflammatory responses to bleomycin-induced lung injury. *Am. J. Respir. Cell Mol. Biol.* **46**, 40–47

96. Sohl, M., Lanner, F., and Farnebo, F. (2010) Sp1 mediate hypoxia induced ephrinB2 expression via a hypoxia-inducible factor independent mechanism. *Biochem. Biophys. Res. Commun.* **391**, 24–27

97. Wang, Y., Nakayama, M., Pitulescu, M. E., Schmidt, T. S., Bochenek, M. L., Sakakibara, A., Adams, S., Davy, A., Deutsch, U., Lüthi, U., Barberis, A., Benjamin, L. E., Mäkinen, T., Nobes, C. D., and Adams, R. H. (2010) Ephrin-B2 controls VEGF-induced angiogenesis and lymphangiogenesis. *Nature.* **465**, 483–486

98. Fu, A. K. Y., Hung, K.-W., Huang, H., Gu, S., Shen, Y., Cheng, E. Y. L., Ip, F. C. F., Huang, X., Fu, W.-Y., and Ip, N. Y. (2014) Blockade of EphA4 signaling ameliorates hippocampal synaptic dysfunctions in mouse models of Alzheimer's disease. *Proc. Natl. Acad. Sci.* **111**, 9959–9964

99. Vargas, L. M., Cerpa, W., Muñoz, F. J., Zanlungo, S., and Alvarez, A. R. (2018) Amyloid-β oligomers synaptotoxicity: The emerging role of EphA4/c-Abl signaling in Alzheimer's disease. *Biochim. Biophys. Acta - Mol. Basis Dis.* **1864**, 1148–1159

100. Cancino, G. I., Toledo, E. M., Leal, N. R., Hernandez, D. E., Yévenes, L. F., Inestrosa, N. C., and Alvarez, A. R. (2008) STI571 prevents apoptosis, tau phosphorylation and behavioural impairments induced by Alzheimer's β-amyloid deposits. *Brain.* **131**, 2425–2442

101. Van Hoecke, A., Schoonaert, L., Lemmens, R., Timmers, M., Staats, K. A., Laird, A. S., Peeters, E., Philips, T., Goris, A., Dubois, B., Andersen, P. M., Al-Chalabi, A., Thijs, V., Turnley, A. M., Van Vught, P. W., Veldink, J. H., Hardiman, O., Van Den Bosch, L., Gonzalez-Perez, P., Van Damme, P., Brown, R. H., Van Den Berg, L. H., and Robberecht, W. (2012) EPHA4 is a disease modifier of amyotrophic lateral sclerosis in animal models and in humans. *Nat. Med.* **18**, 1418–1422

102. Zhao, J., Cooper, L. T., Boyd, A. W., and Bartlett, P. F. (2018) Decreased signalling of EphA4 improves functional performance and motor neuron survival in the SOD1G93A ALS mouse model. *Sci. Rep.* **8**, 11393

103. Davy, A., Bush, J. O., and Soriano, P. (2006) Inhibition of gap junction communication at ectopic Eph/ephrin boundaries underlies craniofrontonasal syndrome. *PLoS Biol.* **4**, 1763–1776

104. Fox, B. P., and Kandpal, R. P. (2004) Invasiveness of breast carcinoma cells and transcript profile: Eph receptors and ephrin ligands as molecular markers of potential diagnostic and prognostic application. *Biochem. Biophys. Res. Commun.* **318**, 882–892

105. Lin, Y. G., Han, L. Y., Kamat, A. A., Merritt, W. M., Landen, C. N., Deavers, M. T., Fletcher, M. S., Urbauer, D. L., Kinch, M. S., and Sood, A. K. (2007) EphA2 overexpression is associated with angiogenesis in ovarian cancer. *Cancer.* **109**, 332–340

106. Duxbury, M. S., Ito, H., Zinner, M. J., Ashley, S. W., and Whang, E. E. (2004) EphA2: A determinant of malignant cellular behavior and a potential therapeutic target in pancreatic adenocarcinoma. *Oncogene.* **23**, 1448–1456

107. Zeng, G., Hu, Z., Kinch, M. S., Pan, C. X., Flockhart, D. A., Kao, C., Gardner, T. A., Zhang, S., Li, L., Baldridge, L. A., Koch, M. O., Ulbright, T. M., Eble, J. N., and Cheng, L. (2003) High-Level Expression of EphA2 Receptor Tyrosine Kinase in Prostatic Intraepithelial Neoplasia. *Am. J. Pathol.* **163**, 2271–2276

108. Miyazaki, T., Kato, H., Fukuchi, M., Nakajima, M., and Kuwano, H. (2003) EphA2 overexpression correlates with poor prognosis in esophageal squamous cell carcinoma. *Int. J. Cancer.* **103**, 657–663

109. Liu, F., Park, P. J., Lai, W., Maher, E., Chakravarti, A., Durso, L., Jiang, X., Yu, Y., Brosius, A., Thomas, M., Chin, L., Brennan, C., DePinho, R. A., Kohane, I., Carroll, R. S., Black, P. M., and Johnson, M. D. (2006) A genome-wide screen reveals functional gene clusters in the cancer genome and identifies EphA2 as a mitogen in glioblastoma. *Cancer Res.* **66**, 10815–10823

110. Thaker, P. H., Deavers, M., Celestino, J., Thornton, A., Fletcher, M. S., Landen, C. N., Kinch, M. S., Kiener, P. A., and Sood, A. K. (2004) EphA2 expression is associated with aggressive features in ovarian carcinoma. *Clin. Cancer Res.* **10**, 5145–5150

111. Wu, D., Suo, Z., Kristensen, G. B., Li, S., Troen, G., Holm, R., and Nesland, J. M. (2004) Prognostic value of EphA2 and EphrinA-1 in squamous cell cervical carcinoma. *Gynecol. Oncol.* **94**, 312–319

112. Herrem, C. J., Tatsumi, T., Olson, K. S., Shirai, K., Finke, J. H., Bukowski, R. M., Zhou, M., Richmond, A. L., Derweesh, I., Kinch, M. S., and Storkus, W. J. (2005) Expression of EphA2 is prognostic of disease-free interval and overall survival in surgically treated patients with renal cell carcinoma. *Clin. Cancer Res.* **11**, 226–231

113. Cesarman, E., Chang, Y., Moore, P. S., Said, J. W., and Knowles, D. M. (1995) Kaposi's sarcoma—associated herpesvirus-like DNA sequences in AIDS-related body-cavity—based lymphomas. *N. Engl. J. Med.* **332**, 1186–1191

114. Hahn, A. S., Kaufmann, J. K., Wies, E., Naschberger, E., Panteleev-Ivlev, J., Schmidt, K., Holzer, A., Schmidt, M., Chen, J., König, S., Ensser, A., Myoung, J., Brockmeyer, N. H., Stürzl, M., Fleckenstein, B., and Neipel, F. (2012) The ephrin receptor tyrosine kinase A2 is a cellular receptor for Kaposi's sarcoma-associated herpesvirus. *Nat. Med.* **18**, 961–966

115. Zhang, H., Li, Y., Wang, H. B., Zhang, A., Chen, M. L., Fang, Z. X., Dong, X. D., Li, S. B., Du, Y., Xiong, D., He, J. Y., Li, M. Z., Liu, Y. M., Zhou, A. J., Zhong, Q., Zeng, Y. X., Kieff, E., Zhang, Z., Gewurz, B. E., Zhao, B., and Zeng, M. S. (2018) Ephrin receptor A2 is an epithelial cell receptor for Epstein-Barr virus entry. *Nat. Microbiol.* **3**, 164–171

116. Chen, J., Sathiyamoorthy, K., Zhang, X., Schaller, S., Perez White, B. E., Jardetzky, T. S., and Longnecker, R. (2018) Ephrin receptor A2 is a functional entry receptor for Epstein-Barr virus. *Nat. Microbiol.* **3**, 172–180

117. Farrell, P. J. (2019) Epstein-Barr Virus and Cancer. *Annu. Rev. Pathol. Mech. Dis.* **14**, 29–53

118. Lupberger, J., Zeisel, M. B., Xiao, F., Thumann, C., Fofana, I., Zona, L., Davis, C., Mee, C. J., Turek, M., Gorke, S., Royer, C., Fischer, B., Zahid, M. N., Lavillette, D., Fresquet, J., Cosset, F. L., Rothenberg, S. M., Pietschmann, T., Patel, A. H., Pessaux, P., Dofföl, M., Raffelsberger, W., Poch, O., McKeating, J. A., Brino, L., and Baumert, T. F. (2011) EGFR and EphA2 are host factors for hepatitis C virus entry and possible targets for antiviral therapy. *Nat. Med.* **17**, 589–595

119. Pasquale, E. B. (2010) Eph receptors and ephrins in cancer: Bidirectional signalling and beyond. *Nat. Rev. Cancer.* **10**, 165–180

120. Hafner, C., Schmitz, G., Meyer, S., Bataille, F., Hau, P., Langmann, T., Dietmaier, W., Landthaler, M., and Vogt, T. (2004) Differential Gene Expression of Eph Receptors and Ephrins in Benign Human Tissues and Cancers. *Clin. Chem.* **50**, 490–499

121. Macrae, M., Neve, R. M., Rodriguez-Viciana, P., Haqq, C., Yeh, J., Chen, C., Gray, J. W., and McCormick, F. (2005) A conditional feedback loop regulates Ras activity through EphA2. *Cancer Cell.* **8**, 111–118

122. Nikolov, D. B., Xu, K., and Himanen, J. P. (2014) Homotypic receptor-receptor interactions regulating Eph signaling. *Cell Adhes. Migr.* **8**, 360–365

123. Janes, P. W., Nievergall, E., and Lackmann, M. (2012) Concepts and consequences of Eph receptor clustering. *Semin. Cell Dev. Biol.* **23**, 43–50

124. Miao, H., Li, D. Q., Mukherjee, A., Guo, H., Petty, A., Cutter, J., Basilion, J. P., Sedor, J., Wu, J., Danielpour, D., Sloan, A. E., Cohen, M. L., and Wang, B. (2009) EphA2 Mediates Ligand-Dependent Inhibition and Ligand-Independent Promotion of Cell Migration and Invasion via a Reciprocal Regulatory Loop with Akt. *Cancer Cell.* **16**, 9–20

125. Paraiso, K. H. T., Das Thakur, M., Fang, B., Koomen, J. M., Fedorenko, I. V., John, J. K., Tsao, H., Flaherty, K. T., Sondak, V. K., Messina, J. L., Pasquale, E. B., Villagra, A., Rao, U. N., Kirkwood, J. M., Meier, F., Sloot, S., Gibney, G. T., Stuart, D., Tawbi, H., and Smalley, K. S. M. (2015) Ligand-Independent EPHA2 signaling drives the adoption of a targeted Therapy-Mediated metastatic melanoma phenotype. *Cancer Discov.* **5**, 264–273

126. Zhou, Y., Yamada, N., Tanaka, T., Hori, T., Yokoyama, S., Hayakawa, Y., Yano, S., Fukuoka, J., Koizumi, K., Saiki, I., and Sakurai, H. (2015) Crucial roles of RSK in cell motility by catalysing serine phosphorylation of EphA2. *Nat. Commun.* **6**, 1–12

127. Barquilla, A., Lamberto, I., Noberini, R., Heynen-Genel, S., Brill, L. M., and Pasquale, E. B. (2016) Protein kinase A can block EphA2 receptor-

mediated cell repulsion by increasing EphA2 S897 phosphorylation. *Mol. Biol. Cell.* **27**, 2757–2770

128. Kawai, H., Kobayashi, M., Hiramoto-Yamaki, N., Harada, K., Negishi, M., and Katoh, H. (2013) Ephexin4-mediated promotion of cell migration and anoikis resistance is regulated by serine 897 phosphorylation of EphA2. *FEBS Open Bio.* **3**, 78–82

129. Miao, H., Burnett, E., Kinch, M., Simon, E., and Wang, B. (2000) Activation of EphA2 kinase suppresses integrin function and causes focal-adhesion-kinase dephosphorylation. *Nat. Cell Biol.* **2**, 62–69

130. Boyd, A. W., Bartlett, P. F., and Lackmann, M. (2014) Therapeutic targeting of EPH receptors and their ligands. *Nat. Rev. Drug Discov.* **13**, 39–62

131. Miao, H., Wei, B. R., Peehl, D. M., Li, Q., Alexandrou, T., Schelling, J. R., Rhim, J. S., Sedor, J. R., Burnett, E., and Wang, B. (2001) Activation of EphA receptor tyrosine kinase inhibits the Ras/MAPK pathway. *Nat. Cell Biol.* **3**, 527–530

132. Larsen, A. B., Stockhausen, M. T., and Poulsen, H. S. (2010) Cell adhesion and EGFR activation regulate EphA2 expression in cancer. *Cell. Signal.* **22**, 636–644

133. Carter, N., Nakamoto, T., Hirai, H., and Hunter, T. (2002) EphrinA1-induced cytoskeletal re-organization requires FAK and p130cas. *Nat. Cell Biol.* **4**, 565–573

134. Cowan, C. W., Shao, Y. R., Sahin, M., Shamah, S. M., Lin, M. Z., Greer, P. L., Gao, S., Griffith, E. C., Brugge, J. S., and Greenberg, M. E. (2005) Vav family GEFs link activated Ephs to endocytosis and axon guidance. *Neuron.* **46**, 205–217

135. Yoo, S., Shin, J., and Park, S. (2010) EphA8-ephrinA5 signaling and clathrin-mediated endocytosis is regulated by Tiam-1, a Rac-specific guanine nucleotide exchange factor. *Mol. Cells.* **29**, 603–609

136. Boissier, P., Chen, J., and Huynh-Do, U. (2013) Epha2 signaling following endocytosis: Role of tiam1. *Traffic.* **14**, 1255–1271

137. Bocharov, E. V, Mayzel, M. L., Volynsky, P. E., Mineev, K. S., Tkach, E. N., Ermolyuk, Y. S., Schulga, A. A., Efremov, R. G., and Arseniev, A. S. (2010) Left-Handed Dimer of EphA2 Transmembrane Domain : Helix Packing Diversity among Receptor Tyrosine Kinases. *Biophysj.* **98**, 881–889

138. Singer, S. J., and Nicolson, G. L. (1972) The Fluid Mosaic Model of the Structure of Cell Membranes. *Science (80-.).* **175**, 720–731

139. Bretscher, M. S., and Raff, M. C. (1975) Mammalian plasma membranes. *Nature.* **258**, 43–49

140. Ferrell, J. E., and Huests, W. H. (1984) Phosphoinositide metabolism and the morphology of human erythrocytes. *J. Cell Biol.* **98**, 1992–1998

141. Czech, M. P. (2000) PIP2 and PIP3: Complex roles at the cell surface. *Cell.* **100**, 603–606

142. Fruman, D. A., Meyers, R. E., and Cantley, L. C. (1998) Phosphoinositide

kinases. *Annu. Rev. Biochem.* **67**, 481–507

143. Berridge, M. J., and Irvine, R. F. (1984) Inositol triphosophate, a novel second messenger in cellular transduction. *Nature.* **312**, 315–321

144. Rasmussen, H. (1989) The cycling of calcium as an intracellular messenger. *Sci. Am.* **261**, 66–73

145. Newton, A. C. (2018) Protein kinase C: perfectly balanced. *Crit. Rev. Biochem. Mol. Biol.* **53**, 208–230

146. Nishizuka, Y. (1995) Protein kinase C and lipid signaling for sustained cellular responses. *FASEB J.* **9**, 484–496

147. Hamada, K., Shimizu, T., Matsui, T., Tsukita, S., Tsukita, S., and Hakoshima, T. (2000) Structural basis of the membrane-targeting and unmasking mechanisms of the radixin FERM domain. *EMBO J.* **19**, 4449–4462

148. Ford, M. G. J., Pearse, B. M. F., Higgins, M. K., Vallis, Y., Owen, D. J., Gibson, A., Hopkins, C. R., Evans, P. R., and McMahon, H. T. (2001) Simultaneous binding of PtdIns (4,5) P2 and clathrin by AP180 in the nucleation of clathrin lattices on membranes. *Science (80-.).* **291**, 1051–1055

149. Ferguson, K. M., Lemmon, M. A., Schlessinger, J., and Sigler, P. B. (1995) Structure of the high affinity complex of inositol trisphosphate with a phospholipase C pleckstrin homology domain. *Cell.* **83**, 1037–1046

150. Wendland, B., Steece, K. E., and Emr, S. D. (1999) Yeast epsins contain an essential N-terminal ENTH domain, bind clathrin and are required for endocytosis. *EMBO J.* **18**, 4383–4393

151. Stenmark, H. (2000) Membrane traffic: Cycling lipids. *Curr. Biol.* **10**, 57–59

152. Chishti, A., Kim, A., and Hoover, K. B. (1998) The FERM domain : a unique module involved in. *Tibs.* **0004**, 281–282

153. Kavran, J. M., Klein, D. E., Lee, A., Falasca, M., Isakoff, S. J., Skolnik, E. Y., and Lemmon, M. A. (1998) Specificity and promiscuity in phosphoinositide binding by pleckstrin homology domains. *J. Biol. Chem.* **273**, 30497–30508

154. Dietrich, U., Krüger, P., Gutberlet, T., and Käs, J. A. (2009) Interaction of the MARCKS peptide with PIP2 in phospholipid monolayers. *Biochim. Biophys. Acta - Biomembr.* **1788**, 1474–1481

155. Arbuzova, A., Murray, D., and McLaughlin, S. (1998) MARCKS, membranes, and calmodulin: Kinetics of their interaction. *Biochim. Biophys. Acta - Rev. Biomembr.* **1376**, 369–379

156. McLaughlin, S., Smith, S. O., Hayman, M. J., and Murray, D. (2005) An electrostatic engine model for autoinhibition and activation of the epidermal growth factor receptor (EGFR/ErbB) family. *J. Gen. Physiol.* **126**, 41–53

157. Sengupta, P., Bosis, E., Nachliel, E., Gutman, M., Smith, S. O., Mihályné, G., Zaitseva, I., and McLaughlin, S. (2009) EGFR juxtamembrane domain, membranes, and calmodulin: Kinetics of their interaction. *Biophys. J.* **96**, 4887–4895

158. Li, H., and Villalobo, A. (2002) Evidence for the direct interaction between calmodulin and the human epidermal growth factor receptor. *Biochem. J.* **362**, 499–505

159. Hedger, G., Sansom, M. S. P., and Koldsø, H. (2015) The juxtamembrane regions of human receptor tyrosine kinases exhibit conserved interaction sites with anionic lipids. *Sci. Rep.* **5**, 1–10

160. Wang, Z., Fan, H., Hu, X., Khamo, J., Diao, J., Zhang, K., and Pogorelov, T. V. (2019) Coaction of Electrostatic an Hyrophobic Interactions: Dynamic Constraints on Disorere TrkA Juxtamembrane Domain. *J. Phys. Chem. B.* **123**, 10709–10717

161. London, M., and Gallo, E. (2020) The EphA2 and cancer connection : potential for immune - based interventions. *Mol. Biol. Rep.* 10.1007/s11033-020-05767-y

162. Carles-Kinch, K., Kilpatrick, K. E., Stewart, J. C., and Kinch, M. S. (2002) Antibody targeting of the EphA2 tyrosine kinase inhibits malignant cell behavior. *Cancer Res.* **62**, 2840–2847

163. Singh, D. R., Pasquale, E. B., and Hristova, K. (2016) A small peptide promotes EphA2 kinase-dependent signaling by stabilizing EphA2 dimers. *Biochim. Biophys. Acta - Gen. Subj.* **1860**, 1922–1928

164. Sugiyama, N., Gucciardo, E., Tatti, O., Varjosalo, M., Hyytiäinen, M., Gstaiger, M., and Lehti, K. (2013) Epha2 cleavage by MT1-MMP triggers single cancer cell invasion via homotypic cell repulsion. *J. Cell Biol.* **201**, 467–484

165. Koshikawa, N., Hoshino, D., Taniguchi, H., Minegishi, T., Tomari, T., Nam, S. O., Aoki, M., Sueta, T., Nakagawa, T., Miyamoto, S., Nabeshima, K., Weaver, A. M., and Seiki, M. (2015) Proteolysis of EphA2 converts it from a tumor suppressor to an oncoprotein. *Cancer Res.* **75**, 3327–3339

166. Carpenter, A. E., Jones, T. R., Lamprecht, M. R., Clarke, C., Kang, I. H., Friman, O., Guertin, D. A., Chang, J. H., Lindquist, R. A., Moffat, J., Golland, P., and Sabatini, D. M. (2006) CellProfiler: Image analysis software for identifying and quantifying cell phenotypes. *Genome Biol.* 10.1186/gb-2006-7-10-r100

167. Barquilla, A., Lamberto, I., Noberini, R., Heynen-Genel, S., Brill, L. M., and Pasquale, E. B. (2016) Protein kinase A can block EphA2 receptor-mediated cell repulsion by increasing EphA2 S897 phosphorylation. *Mol. Biol. Cell.* **27**, 2757–2770

168. Cho, M. C., Cho, S. Y., Yoon, C. Y., Lee, S. B., and Kwak, C. (2015) EphA2 Is a Potential Player of Malignant Cellular Behavior in Non-Metastatic Renal Cell Carcinoma Cells but Not in Metastatic Renal Cell Carcinoma Cells. 10.1371/journal.pone.0130975

169. Nikolov, D. B., Xu, K., and Himanen, J. P. (2014) Homotypic receptor-receptor interactions regulating Eph signaling. *Cell Adhes. Migr.* **8**, 360–365

170. von Heijne, G. (1990) The signal peptide. *J. Membr. Biol.* **115**, 195–201

171. Pasquale, E. B. (2008) Eph-Ephrin Bidirectional Signaling in Physiology and Disease. *Cell.* **133**, 38–52

172. Risley, M., Garrod, D., Henkemeyer, M., and McLean, W. (2009) EphB2 and EphB3 forward signalling are required for palate development. *Mech. Dev.* **126**, 230–239

173. Kinch, M. S., Moore, M. B., and Harpole, D. H. (2003) Predictive value of the EphA2 receptor tyrosine kinase in lung cancer recurrence and survival. *Clin. Cancer Res.* **9**, 613–618

174. Chen, J., Schaller, S., Jardetzky, T. S., and Longnecker, R. (2020) EBV gH/gL and KSHV gH/gL bind to different sites on EphA2 to trigger fusion. *J. Virol.* 10.1128/JVI.01454-20

175. Wykosky, J., and Debinski, W. (2008) The EphA2 Receptor and EphrinA1 Ligand in Solid Tumors: Function and Therapeutic Targeting. *Mol. Cancer Res.* **6**, 1795–1806

176. Singh, D. R., Ahmed, F., King, C., Gupta, N., Salotto, M., Pasquale, E. B., and Hristova, K. (2015) EphA2 receptor unliganded dimers suppress EphA2 pro-tumorigenic signaling. *J. Biol. Chem.* **290**, 27271–27279

177. Fiske, C. H., and Subbarow, Y. (1925) The colorimetric determination of phosphorus. *J. Biol. Chem.* **66**, 375–400

178. Chandradoss, S. D., Haagsma, A. C., Lee, Y. K., Hwang, J. H., Nam, J. M., and Joo, C. (2014) Surface passivation for single-molecule protein studies. *J. Vis. Exp.* 10.3791/50549

179. Lamichhane, R., Solem, A., Black, W., and Rueda, D. (2010) Single-molecule FRET of protein-nucleic acid and protein-protein complexes: Surface passivation and immobilization. *Methods.* **52**, 192–200

180. Aitken, C. E., Marshall, R. A., and Puglisi, J. D. (2008) An oxygen scavenging system for improvement of dye stability in single-molecule fluorescence experiments. *Biophys. J.* **94**, 1826–1835

181. Tinnefeld, P. (2011) Pull-down for single molecules. *Nature.* **473**, 461–462

182. Kučerka, N., Gallová, J., Uhríková, D., Balgavý, P., Bulacu, M., Marrink, S. J., and Katsaras, J. (2009) Areas of monounsaturated diacylphosphatidylcholines. *Biophys. J.* **97**, 1926–1932

183. Nyholm, T. K. M., Özdirekcan, S., and Antoinette Killian, J. (2007) How protein transmembrane segments sense the lipid environment. *Biochemistry.* **46**, 1457–1465

184. Wu, Y., Huang, H. W., and Olah, G. A. (1990) Method of oriented circular dichroism. *Biophys. J.* **57**, 797–806

185. Burck, J., Wadhwani, P., Fangha, S., and Ulrich, A. S. (2016) Oriented Circular Dichroism : A Method to Characterize Membrane- Active Peptides in Oriented Lipid Bilayers. *Acc. Chem. Res.* **49**, 184–192

186. Ulmschneider, M. B., Ulmschneider, J. P., Schiller, N., Wallace, B. A., Von Heijne, G., and White, S. H. (2014) Spontaneous transmembrane helix insertion thermodynamically mimics translocon-guided insertion. *Nat. Commun.* 10.1038/ncomms5863

187. Postis, V., Rawson, S., Mitchell, J. K., Lee, S. C., Parslow, R. A., Dafforn, T. R., Baldwin, S. A., and Muench, S. P. (2015) The use of SMALPs as a novel membrane protein scaffold for structure study by negative stain electron microscopy. *Biochim. Biophys. Acta - Biomembr.* **1848**, 496–501

188. Knowles, T. J., Finka, R., Smith, C., Lin, Y. P., Dafforn, T., and Overduin, M. (2009) Membrane proteins solubilized intact in lipid containing nanoparticles bounded by styrene maleic acid copolymer. *J. Am. Chem. Soc.* **131**, 7484–7485

189. Ladokhin, A. S., Jayasinghe, S., and White, S. H. (2000) How to Measure and Analyze Tryptophan Fluorescence in Membranes Properly , and Why Bother ? *Anal. Biochem.* **245**, 235–245

190. Singh, D. R., Kanvinde, P., King, C., Pasquale, E. B., and Hristova, K. (2018) The EphA2 receptor is activated through induction of distinct, ligand-dependent oligomeric structures. *Commun. Biol.* **1**, 15

191. Gulamhussein, A. A., Meah, D., Soja, D. D., Fenner, S., Saidani, Z., Akram, A., Lallie, S., Mathews, A., Painter, C., Liddar, M. K., Mohammed, Z., Chiu, L. K., Sumar, S. S., Healy, H., Hussain, N., Patel, J. H., Hall, S. C. L., Dafforn, T. R., and Rothnie, A. J. (2019) Examining the stability of membrane proteins within SMALPs. *Eur. Polym. J.* **112**, 120–125

192. Toner, M., Vaio, G., McLaughlin, A., and McLaughlin, S. (1988) Adsorption of Cations to Phosphatidylinositol 4,5-Bisphosphate. *Biochemistry.* **27**, 7435–7443

193. Van Meer, G., Voelker, D. R., and Feigenson, G. W. (2008) Membrane lipids: Where they are and how they behave. *Nat. Rev. Mol. Cell Biol.* **9**, 112–124

194. Chavent, M., Karia, D., Kalli, A. C., Domański, J., Duncan, A. L., Hedger, G., Stansfeld, P. J., Seiradake, E., Jones, E. Y., and Sansom, M. S. P. (2018) Interactions of the EphA2 Kinase Domain with PIPs in Membranes: Implications for Receptor Function. *Structure.* **26**, 1025-1034.e2

195. Chen, Y., and Barkley, M. D. (1998) Toward understanding tryptophan fluorescence in proteins. *Biochemistry.* **37**, 9976–9982

196. Vivian, J. T., and Callis, P. R. (2001) Mechanisms of tryptophan fluorescence shifts in proteins. *Biophys. J.* **80**, 2093–2109

197. Slochower, D. R., Huwe, P. J., Radhakrishnan, R., and Janmey, P. A. (2013) Quantum and all-atom molecular dynamics simulations of protonation and divalent ion binding to phosphatidylinositol 4,5-bisphosphate (PIP2). *J. Phys. Chem. B.* **117**, 8322–8329

198. Boettcher, J. M., Davis-Harrison, R. L., Clay, M. C., Nieuwkoop, A. J., Ohkubo, Y. Z., Tajkhorshid, E., Morrissey, J. H., and Rienstra, C. M. (2011) Atomic view of calcium-induced clustering of phosphatidylserine in mixed lipid bilayers. *Biochemistry.* **50**, 2264–2273

199. Michailidis, I. E., Rusinova, R., Georgakopoulos, A., Chen, Y., Iyengar, R., Robakis, N. K., Logothetis, D. E., and Baki, L. (2011) Phosphatidylinositol-4,5-bisphosphate regulates epidermal growth factor receptor activation.

Pflugers Arch. Eur. J. Physiol. **461**, 387–397

200. Westerfield, J. M., and Barrera, F. N. (2020) Membrane receptor activation mechanisms and transmembrane peptide tools to elucidate them. *J. Biol. Chem.* **295**, 1792–1814

201. McLaughlin, S., Smith, S. O., Hayman, M. J., and Murray, D. (2005) An electrostatic engine model for autoinhibition and activation of the epidermal growth factor receptor (EGFR/ErbB) family. *J. Gen. Physiol.* **126**, 41–53

202. Chavent, M., Seiradake, E., Jones, E. Y., and Sansom, M. S. P. (2016) Structures of the EphA2 Receptor at the Membrane: Role of Lipid Interactions. *Structure*. **24**, 337–347

203. Shi, X., Hapiak, V., Zheng, J., Muller-Greven, J., Bowman, D., Lingerak, R., Buck, M., Wang, B. C., and Smith, A. W. (2017) A role of the SAM domain in EphA2 receptor activation. *Sci. Rep.* **7**, 1–12

204. Seiradake, E., Harlos, K., Sutton, G., Aricescu, A. R., and Jones, E. Y. (2010) An extracellular steric seeding mechanism for Eph-ephrin signaling platform assembly. *Nat. Struct. Mol. Biol.* **17**, 398–402

205. Borthakur, S., Lee, H. J., Kim, S. J., Wang, B. C., and Buck, M. (2014) Binding and function of phosphotyrosines of the Ephrin A2 (EphA2) receptor using synthetic sterile α motif (SAM) domains. *J. Biol. Chem.* **289**, 19694–19703

206. Lee, H. J., Hota, P. K., Chugha, P., Guo, H., Miao, H., Zhang, L., Kim, S. J., Stetzik, L., Wang, B. C., and Buck, M. (2012) NMR structure of a heterodimeric SAM:SAM complex: Characterization and Manipulation of EphA2 Binding Reveal New Cellular Functions of SHIP2. *Structure*. **20**, 41–55

207. Phillips, R., Ursell, T., Wiggins, P., and Sens, P. (2009) Emerging roles for lipids in shaping membrane-protein function. *Nature*. **459**, 379–385

208. Sachs, J. N., and Engelman, D. M. (2006) Introduction to the membrane protein reviews: The interplay of structure, dynamics, and environment in membrane protein function. *Annu. Rev. Biochem.* **75**, 707–712

209. Andersen, O. S., and Koeppe, R. E. (2007) Bilayer thickness and membrane protein function: An energetic perspective. *Annu. Rev. Biophys. Biomol. Struct.* **36**, 107–130

210. Woodka, A. C., Butler, P. D., Porcar, L., Farago, B., and Nagao, M. (2012) Lipid bilayers and membrane dynamics: Insight into thickness fluctuations. *Phys. Rev. Lett.* **109**, 1–5

211. Henzler-Wildman, K., and Kern, D. (2007) Dynamic personalities of proteins. *Nature*. **450**, 964–972

212. Ashkar, R., Nagao, M., Butler, P. D., Woodka, A. C., Sen, M. K., and Koga, T. (2015) Tuning Membrane Thickness Fluctuations in Model Lipid Bilayers. *Biophys. J.* **109**, 106–112

213. Bingham, R. J., Smye, S. W., and Olmsted, P. D. (2015) Dynamics of an asymmetric bilayer lipid membrane in a viscous solvent. *Epl*. 10.1209/0295-5075/111/18004

214. Axelrod, D., Koppel, D. E., Schlessinger, J., Elson, E., and Webb, W. W. (1976) Mobility measurement by analysis of fluorescence photobleaching recovery kinetics. *Biophys. J.* **16**, 1055–1069

215. Soumpasis, D. M. (1983) Theoretical analysis of fluorescence photobleaching recovery experiments. *Biophys. J.* **41**, 95–97

216. Lin, W.-C., Yu, C.-H., Triffo, S., and Groves, J. T. (2010) *Supported Membrane Formation, Characterization, Functionalization, and Patterning for Application in Biological Science and Technology*, 10.1002/9780470559277.ch100131

217. Kalb, E., Frey, S., and Tamm, L. K. (1992) Formation of supported planar bilayers by fusion of vesicles to supported phospholipid monolayers. *BBA - Biomembr.* **1103**, 307–316

218. Kang, M., Day, C. A., Kenworthy, A. K., and DiBenedetto, E. (2012) Simplified equation to extract diffusion coefficients from confocal FRAP data. *Traffic.* **13**, 1589–1600

Vita

Katherine M. Stefanski (née Smith) was born in Blytheville, Arkansas. She received a Bachelor of Science in Biology from the University of North Carolina at Chapel Hill in 2009. She later received a Master of Science in Biology from Middle Tennessee State University in 2015. She enrolled in the Graduate School of Genome Science and Technology at the University of Tennessee in 2016. Upon graduation she became a postdoctoral scholar in the lab of Charles Sanders at Vanderbilt University.